The Dissertation Committee for Bonil Koo Certifies that this is the approved version of the following dissertation:

CdTe/CdSe/CdTe Heterostructure Nanorods and I-III-VI$_2$ Nanocrystals: Synthesis and Characterization

Committee:

Brian A. Korgel, Supervisor

John G. Ekerdt

James R. Chelikowsky

Charles B. Mullins

Chih-Kang(Ken) Shih

CdTe/CdSe/CdTe Heterostructure Nanorods and I-III-VI$_2$ Nanocrystals: Synthesis and Characterization

by

Bonil Koo, B.S.

Dissertation

Presented to the Faculty of the Graduate School of

The University of Texas at Austin

in Partial Fulfillment

of the Requirements

for the Degree of

Doctor of Philosophy

The University of Texas at Austin

December 2009

Dedicated to Jiye, Daniel, and Timothy

Acknowledgements

First of all, I can't thank enough to my advisor, Dr. Brian Korgel, for his giving me a great opportunity working his group from 2005 and guiding my research with all his efforts so far. His enthusiastic research and brilliant insights constructively challenged me to go beyond my own steps. Also, he led me to learn from him how to effectively teach and guide other people. I remember that any discussion with him was very comfortable and positive. Particularly, the fundamental understanding of nanoscience and the approach strategy to dig out science that I acquired from him were the most beneficial parts in my PhD life for four and half years. Besides these above, I am also indebted to his hearted consideration even when I had to take care of my personal situations—having and raising two kids with my wife.

I am also very thankful to all of the Korgelite (past and present Korgel group members) since they were always happy to help me, answer my questions, discuss any research project, and play basketball. I was glad to start my PhD work with smart and friendly lab mates, Danielle Smith, Dayne Fanfair, Doh C. Lee , Hsing-Yu Tuan, Tripp Davidson, and Ali Ghezelbash. Particularly, Doh C. Lee deserves very special thanks due to his devoted care (academically, mentally, etc) to me when I began my career as an apprentice in the group. Many thanks are to Andrew Heitsch and Damon Smith, who entered this group with me, owing to the friendship and advice offered by them. I am also grateful to other current group members, Vahid Akhavan, Aaron Chockla, Kate Collier, Brian Goodfellow, Justin Harris, Vince Holmberg, Tyne Johns, Matt Panthani, Mike Rasch, Kate Shipman, Chet Steinhagen, Colin Hessel, and Jose Luis Hueso Martos, who shared their time, ideas, advice, and friendship so that I could keep myself motivated

and entertained in the lab. In particular, Colin Hessel deserves big thanks because of his fabulous teaching skill and many helps during my work.

Also, I appreciate my committee members, who devoted their time and knowledge on discussion of my research projects since the preliminary exams.

I would especially like to thank my parents and sister for their love and prayers, and their being my support at all times while pursuing my dreams. Also, I, beyond any description, give my loves and joys to my wife, Jiye Lee, and the most adorable sons, Daniel (Jinmo) and Timothy (Hyunmo). Finally, all of the glories to my everlasting God and his Son, Jesus Christ, my Savior.

CdTe/CdSe/CdTe Heterostructure Nanorods and I-III-VI$_2$ Nanocrystals: Synthesis and Characterization

Publication No._____

Bonil Koo, Ph.D.

The University of Texas at Austin, 2009

Supervisor: Brian A. Korgel

Semiconductor nanocrystals are interesting candidates as new light-absorbing materials for photovoltaic (PV) devices.   They can be dispersed in solvents and cheaply deposited at low-temperature on various substrates.   Also, the nanocrystals have unique optical properties depending on their size due to the quantum size effect and moreover it is easy to uniformly control their stoichiometry.   CdTe/CdSe/CdTe heterostructure nanorods and I-III-VI$_2$ nanocrystals were selected to synthesize and investigate in order to utilize the benefits of colloidal nanocrystals described above.

Colloidal nanorods with linear CdTe/CdSe/CdTe heterojunctions were synthesized by sequential reactant injection.   After CdTe deposition at the ends of initially formed CdSe nanorods, continued heating in solution leads to Se-Te interdiffusion across the heterojunctions and coalescence to decreased aspect ratio.   The Se-Te interdiffusion rates were measured by mapping the composition profile using nanobeam energy dispersive X-ray spectroscopy (EDS).   The rate of nanorod

coalescence was also measured and compared to model predictions using a continuum viscous flow model.

The synthetic method of monodisperse chalcopyrite (tetragonal) $CuInSe_2$ nanocrystals was also developed. The nanocrystals have trigonal pyramidal shape with one polar and three non-polar surface facets. When drop-cast onto carbon substrates, the nanocrystals self-assemble into close-packed monolayers with triangular (honeycomb) lattice structure. Moreover, the effect of excess Cu precursor (CuCl) was studied for the formation of monodisperse trigonal pyramidal $CuInSe_2$ nanocrystals. The formation mechanism of monodisperse trigonal pyramidal $CuInSe_2$ nanocrystals was suggested with regard to excess amount of CuCl precursor, based on the nucleation-growth model of colloidal nanocrystal formation.

A new wurtzite phase of $CuInS_2$, $CuInSe_2$, and $Cu(In_xGa_{1-x})Se_2$ (CIGS) was observed in nanocrystals synthesized by heating metal precursors and Se-(or S-)urea in alkylamine. X-ray diffraction (XRD) showed the predominant phase to be wurtzite (hexagonal) instead of chalcopyrite (tetragonal). High resolution transmission electron microscopy (TEM), however, revealed polytypism in the nanocrystals, with the wurtzite phase interfaced with significant chalcopyrite domains.

Table of Contents

List of Figures

xviii

Chapter 1: Introduction

1.1 HETEROJUNCTION NANOSTRUCTURES

Colloidal chemical routes can be used to synthesize relatively complicated heterojunction nanostructures, such as multiple quantum well quantum dots with onion-like shell structures,[1-4] linear heterojunctions in quantum-size rods[5-9] and branched structures like tetrapods,[5,10,11] and even superlattice quantum wells with oscillating composition along the lengths of nanowires.[12] Heterojunctions create built-in electric fields that deplete or accumulate electrons and holes within the nanostructure, which is potentially useful for optoelectronic technologies like light-emitting diodes,[13] photovoltaics,[14] and optical sensors.[15] The large surface area-to-volume ratio of colloidal nanocrystals and nanorods helps relieve strain at epitaxial interfaces between materials with large lattice mismatches to alleviate the formation of extended defects.[2,16-18] These interfaces, however, can restructure in relatively short times with atomic interdiffusion across the heterojunctions.[6-8,19-21] Furthermore, non-spherical nanocrystals can coalesce into spheres.[6-8,22,23] The dynamics of these processes requires further study and better understanding.

In Chapter 2, the rates of heterojunction interdiffusion and coalescence of CdTe/CdSe/CdTe nanorods are reported and compared to model predictions. Colloidal nanorods with linear CdTe/CdSe/CdTe heterojunctions were synthesized by sequential reactant injection. After CdTe deposition at the ends of initially formed CdSe nanorods, continued heating in solution leads to Se-Te interdiffusion across the heterojunctions and coalescence to decreased aspect ratio. The rate of nanorod coalescence was also measured and compared to model predictions using a continuum viscous flow model.

1

1.2 I-III-VI$_2$ NANOCRYSTALS

Semiconductor nanocrystals are being considered as new light-absorbing materials for photovoltaic devices (PVs).[24-33] For lower cost PV manufacture, nanocrystals could be synthesized in large quantities and then dispersed in solvents for low-temperature deposition on various substrates, including plastics.[30] The nanocrystals could also be deposited within the pores of nanoporous substrates, such as microporous TiO$_2$ films[32] or forests of ZnO nanowires,[33] or combined with polymers to make hybrid light-absorbing layers.[29] Quantum-size nanocrystals have the interesting possibility of multiexciton generation for harvesting short wavelength light in single junction solar cells for improved efficiencies.[26-28] Many nanocrystal materials suitable for PVs have been synthesized, including CdTe,[34] PbSe,[35,36] Ge[37,38] and Si,[39,40] which have optical gaps at the red edge of the solar spectrum.

The ternary I-III-VI$_2$ chalcopyrite materials like CuInSe$_2$ or CuInS$_2$ are particularly interesting candidates for PVs. These materials have band gap energies near the red edge of the visible spectrum, high optical absorption coefficients, durable photostability, and when deposited by vapor-phase routes have been used to achieve high efficiency (>10%) PVs.[41,42] However, there have been only a few examples of the nanocrystal synthesis of CuInSe$_2$ and other I-III-VI$_2$ chalcopyrite compounds in solution.[43-50] Very recently, solvent dispersions, or "inks", of nanocrystals of ternary I-III-VI$_2$ compounds have been developed and applied to printed and flexible PVs.[51-55] Since the power conversion efficiencies have been relatively low (<5%),[51-55] part of the challenge facing these efforts has been the need for better synthetic methods for nanocrystals the desired I-III-VI$_2$ compound.

1.2.1 CuInSe$_2$ nanocrystals

In general, reported syntheses of CuInSe$_2$ nanocrystals have suffered from relatively broad size distributions, composition and phase impurities, and poor dispersibility. Very recently, Allen and Bawendi[50] demonstrated Cu-In-Se nanocrystal synthesis with very good size control, but only reported the ordered vacancy chalcopyrite compounds, CuIn$_{1.5}$Se$_3$, CuIn$_{2.3}$Se$_4$ and CuIn$_5$Se$_8$ and not the synthesis of stoichiometric CuInSe$_2$. In Chapter 3, the synthesis of monodisperse, solution-stable chalcopyrite CuInSe$_2$ nanocrystals is reported. The nanocrystals are monodisperse, phase pure, and exhibit a trigonal pyramidal shape. When drop-cast on carbon substrates, they self-assemble into close-packed monolayers with long-range triangular order.

1.2.2 Monodisperse nanocrystals

Monodisperse nanocrystals are of tremendous importance for future generation applications since electrical, magnetic, and optical properties of nanocrystals vary depending on their size, shape, and composition.[56] The colloidal synthesis of monodisperse nanocrystals have been explored for metal, metal oxide, and semiconductor materials with various sizes and shapes.[57-60] Several research groups investigated the reaction mechanism for the synthesis of monodisperse nanoparticles, and they in large attributed it to burst nucleation and separated growth.[60-64] Although the nucleation and growth mechanism for the formation of monodisperse nanoparticles is still under study, it is known that it is influenced by diverse variables such as reaction condition (temperature, time, and sequence), kind of precursor and capping ligand, precursor and monomer concentration, and reactivity among the reactants. Recently, our group reported a synthesis of monodisperse trigonal pyramidal CuInSe$_2$ nanocrystals, and the precise synthetic ways, reaction temperature, and choice of oleylamine were considered as critical factors to make monodisperse CuInSe$_2$ nanocrystals.[65] However, more study

was needed on the factors to influence the monodispersity such as precursor concentration related to reaction kinetics. In Chapter 4, the effect of excess CuCl precursor is discussed on the monodispersity of trigonal pyramidal $CuInSe_2$ nanocrystals.

1.3 WURTZITE-TYPE NANOCRYSTALS

1.3.1 Wurtzite-chalcopyrite polytypism in $CuInS_2$

$CuInS_2$ nanocrystals have been synthesized by a number of research groups in the recent past.[47,49,53,66-75] The crytal structure of those $CuInS_2$ nanocrystals has been mostly revealed to be the expected tetragonal chalcopyrite phase or compositionally disordered cubic, sphalerite.[76] However, very recently, a few reports emerged informing an observance of unexpected wurtzite $CuInS_2$ phase in nanostructures.[66,77-81] For example, Schimmel, *et al.*[82] has reported the formation of wurtzite $CuInS_2$ by thin film electrodeposition and coincidentally, Pan, *et al.*[66] also recently observed wurtzite $CuInS_2$ in their colloidally-grown nanocrystals. Still, the chemistry continues to be refined to obtain nanocrystals with improved size control.

In Chapter 5, a new synthetic route to monodisperse $CuInS_2$ nanodisks is provided. Recent examples of shape control have appeared for $CuInSe_2$ nanocrystals, including doughnuts[52] and trigonal pyramids,[65] but no similar examples of non-spherical nanocrystals of $CuInS_2$. Moreover, X-ray diffraction (XRD) showed that the $CuInS_2$ nanodisks had wurtzite crystal structure instead of the expected tetragonal chalcopyrite phase. Interestingly, high resolution transmission electron microscopy (TEM) of the $CuInS_2$ nanodisks revealed the first example of wurtzite-chalcopyrite polytypism in a I-III-VI_2 compound.

1.3.2 Wurtzite-chalcopyrite polytypism in CuInSe$_2$ and Cu(In$_x$Ga$_{1-x}$)Se$_2$ (CIGS)

As shown above, some CIGS nanocrystals showed unexpected crystal structure.[66,77-81] This is very interesting, as the wurtzite phase is not stable at room temperature in the bulk relative to chalcopyrite and other cubic phases such as sphalerite or ordered vacancy compound.[76] Wurtzite CuInS$_2$ occurs only as a high temperature phase (1045-1090 $^{\circ}$C).[76] However, wurtzite phases of CuInSe$_2$ and CIGS have not been observed in nanocrystals.[83] It is probably due to high stacking fault energy of CuInSe2 relative to other chalcopyrite (or cubic) semiconductors.[84,85] There were only a few reports on slightly manipulated chalcopyrite crystal structure such as compositionally disordered cubic (sphalerite) or ordered vacancy chalcopyrites.[50,52]

In Chapter 6, we report CuInSe$_2$ and Cu(In$_x$Ga$_{1-x}$)Se$_2$ nanocrystals with wurtzite (hexagonal) crystal structure. X-ray diffraction (XRD) revealed wurtzite crystal structure and high resolution transmission electron microscopy (TEM) imaging showed that the nanocrystals in fact were polytypic, as shown in wurtzite-type CuInS$_2$.

1.4 DISSERTATION OVERVIEW

The rates of heterojunction interdiffusion and coalescence of CdTe/CdSe/CdTe nanorods are reported and compared to model predictions in Chapter 2. The Se and Te composition profiles were mapped in individual nanorods aged in hot solvents for different amounts of time to determine the Te in CdSe diffusion coefficient and evaluate the influence of strain on the interdiffusion rates across the heterojunctions. The measured rod-to-sphere coalescence rates were compared to rates predicted using a continuum viscous flow model for nanorod-to-sphere coalescence.

The synthesis and characterization of various types of I-III-VI$_2$ nanocrystals are shown in Chapters 3 through 6.

Chapters 3 and 4 show the synthesis of monodisperse, solution-stable chalcopyrite $CuInSe_2$ nanocrystals. The nanocrystals are monodisperse, phase pure, and exhibit a trigonal pyramidal shape. When drop-cast on carbon substrates, they self-assemble into close-packed monolayers with long-range triangular order. In Chapter 4, the effect of excess CuCl precursor is discussed on the monodispersity of trigonal pyramidal $CuInSe_2$ nanocrystals.

A new synthetic route to monodisperse $CuInS_2$ nanodisks is provided in Chapter 5. X-ray diffraction (XRD) showed that the $CuInS_2$ nanodisks had wurtzite crystal structure instead of the expected tetragonal chalcopyrite phase. High resolution transmission electron microscopy (TEM) of the $CuInS_2$ nanodisks, however, revealed a significant amount of polytypism with most of the nanodisks having domains of chalcopyrite $CuInS_2$ interfaced with wurtzite $CuInS_2$ across $(002)_w/(112)_{ch}$ stacking faults.

In Chapter 6, the $CuInSe_2$ and $Cu(In_xGa_{1-x})Se_2$ nanocrystals with wurtzite (hexagonal) crystal structure are reported. X-ray diffraction (XRD) revealed wurtzite crystal structure in $CuInSe_2$ and $Cu(In_xGa_{1-x})Se_2$ nanocrystals. Extensive high resolution transmission electron microscopy (TEM) imaging showed that the nanocrystals in fact were polytypic, consisting of both chalcopyrite and wurtzite crystal structure within the same nanocrystals. Elemental mapping in the nanocrystals by nanobeam energy dispersive spectroscopy (EDS) line scans revealed compositional variations between the chalcopyrite and wurtzite phases.

Chapter 7 shows the summarized conclusions of the dissertation and suggests future plans to extend my thesis work.

1.5 REFERENCES

(1)   Mews, A.; Eychmuller, A.; Giersig, M.; Schooss, D.; Weller, H. *J Phys Chem-Us* **1994**, *98*, 934-941.

(2)   Kamalov, V. F.; Little, R.; Logunov, S. L.; ElSayed, M. A. *J Phys Chem-Us* **1996**, *100*, 6381-6384.

(3)   Dorfs, D.; Eychmuller, A. *Z Phys Chem* **2006**, *220*, 1539-1552.

(4)   Manna, L.; Scher, E. C.; Li, L. S.; Alivisatos, A. P. *J Am Chem Soc* **2002**, *124*, 7136-7145.

(5)   Mokari, T.; Rothenberg, E.; Popov, I.; Costi, R.; Banin, U. *Science* **2004**, *304*, 1787-1790.

(6)   Shieh, F.; Saunders, A. E.; Korgel, B. A. *J Phys Chem B* **2005**, *109*, 8538-8542.

(7)   Halpert, J. E.; Porter, V. J.; Zimmer, J. P.; Bawendi, M. G. *J Am Chem Soc* **2006**, *128*, 12590-12591.

(8)   Kumar, S.; Jones, M.; Lo, S. S.; Scholes, G. D. *Small* **2007**, *3*, 1633-1639.

(9)   Jones, M.; Kumar, S.; Lo, S. S.; Scholes, G. D. *J Phys Chem C* **2008**, *112*, 5423-5431.

(10)   Milliron, D. J.; Hughes, S. M.; Cui, Y.; Manna, L.; Li, J. B.; Wang, L. W.; Alivisatos, A. P. *Nature* **2004**, *430*, 190-195.

(11)   Yong, K. T.; Sahoo, Y.; Swihart, M. T.; Prasad, P. N. *Adv Mater* **2006**, *18*, 1978.

(12)   Robinson, R. D.; Sadtler, B.; Demchenko, D. O.; Erdonmez, C. K.; Wang, L. W.; Alivisatos, A. P. *Science* **2007**, *317*, 355-358.

(13)   Coe, S.; Woo, W. K.; Bawendi, M.; Bulovic, V. *Nature* **2002**, *420*, 800-803.

(14)   Zhong, H. Z.; Zhou, Y.; Yang, Y.; Yang, C. H.; Li, Y. F. *J Phys Chem C* **2007**, *111*, 6538-6543.

(15)   Konstantatos, G.; Howard, I.; Fischer, A.; Hoogland, S.; Clifford, J.; Klem, E.; Levina, L.; Sargent, E. H. *Nature* **2006**, *442*, 180-183.

(16)   Chen, X. B.; Lou, Y. B.; Samia, A. C.; Burda, C. *Nano Lett* **2003**, *3*, 799-803.

(17)   Shenoy, V. B. *Phys Rev B* **2005**, *71*.

(18)   Dingreville, R.; Qu, J. M.; Cherkaoui, M. *J Mech Phys Solids* **2005**, *53*, 1827-1854.

(19)   Wang, Y. L.; Cai, L.; Xia, Y. N. *Adv Mater* **2005**, *17*, 473.

(20)   Peng, S.; Sun, S. H. *Angew Chem Int Edit* **2007**, *46*, 4155-4158.

(21)   Yin, Y. D.; Erdonmez, C. K.; Cabot, A.; Hughes, S.; Alivisatos, A. P. *Adv Funct Mater* **2006**, *16*, 1389-1399.

(22)   Puntes, V. F.; Krishnan, K. M.; Alivisatos, A. P. *Science* **2001**, *291*, 2115-2117.

(23)   Jun, Y. W.; Jung, Y. Y.; Cheon, J. *J Am Chem Soc* **2002**, *124*, 615-619.

(24)   Gur, I.; Fromer, N. A.; Geier, M. L.; Alivisatos, A. P. *Science* **2005**, *310*, 462-465.

(25)   Kumar, S.; Scholes, G. D. *Microchim Acta* **2008**, *160*, 315-325.

(26)   Nozik, A. J. *Chem Phys Lett* **2008**, *457*, 3-11.

(27)   Schaller, R. D.; Klimov, V. I. *Phys Rev Lett* **2004**, *92*.

(28)   Trinh, M. T.; Houtepen, A. J.; Schins, J. M.; Hanrath, T.; Piris, J.; Knulst, W.; Goossens, A. P. L. M.; Siebbeles, L. D. A. *Nano Lett* **2008**, *8*, 1713-1718.

(29)   Huynh, W. U.; Dittmer, J. J.; Alivisatos, A. P. *Science* **2002**, *295*, 2425-2427.

(30)   Wu, Y.; Wadia, C.; Ma, W. L.; Sadtler, B.; Alivisatos, A. P. *Nano Lett* **2008**, *8*, 2551-2555.

(31)   Koleilat, G. I.; Levina, L.; Shukla, H.; Myrskog, S. H.; Hinds, S.; Pattantyus-Abraham, A. G.; Sargent, E. H. *Acs Nano* **2008**, *2*, 833-840.

(32)   Gunes, S.; Neugebauer, H.; Sariciftci, N. S.; Roither, H.; Kovalenko, M.; Pillwein, G.; Heiss, W. *Adv Funct Mater* **2006**, *16*, 1095-1099.

(33)   Leschkies, K. S.; Divakar, R.; Basu, J.; Enache-Pommer, E.; Boercker, J. E.; Carter, C. B.; Kortshagen, U. R.; Norris, D. J.; Aydil, E. S. *Nano Lett* **2007**, *7*, 1793-1798.

(34)   Manna, L.; Milliron, D. J.; Meisel, A.; Scher, E. C.; Alivisatos, A. P. *Nat Mater* **2003**, *2*, 382-385.

(35)   Cho, K. S.; Talapin, D. V.; Gaschler, W.; Murray, C. B. *J Am Chem Soc* **2005**, *127*, 7140-7147.

(36)   Law, M.; Luther, J. M.; Song, O.; Hughes, B. K.; Perkins, C. L.; Nozik, A. J. *J Am Chem Soc* **2008**, *130*, 5974-5985.

(37) Lu, X. M.; Ziegler, K. J.; Ghezelbash, A.; Johnston, K. P.; Korgel, B. A. *Nano Lett* **2004**, *4*, 969-974.

(38) Gerion, D.; Zaitseva, N.; Saw, C.; Casula, M. F.; Fakra, S.; Van Buuren, T.; Galli, G. *Nano Lett* **2004**, *4*, 597-602.

(39) Heitsch, A. T.; Fanfair, D. D.; Tuan, H. Y.; Korgel, B. A. *J Am Chem Soc* **2008**, *130*, 5436.

(40) Zhang, X.; Brynda, M.; Britt, R. D.; Carroll, E. C.; Larsen, D. S.; Louie, A. Y.; Kauzlarich, S. M. *J Am Chem Soc* **2007**, *129*, 10668.

(41) Repins, I.; Contreras, M. A.; Egaas, B.; DeHart, C.; Scharf, J.; Perkins, C. L.; To, B.; Noufi, R. *Prog Photovoltaics* **2008**, *16*, 235-239.

(42) Cahen, D.; Dagan, G.; Mirovsky, Y.; Hodes, G.; Giriat, W.; Lubke, M. *J Electrochem Soc* **1985**, *132*, 1062-1070.

(43) Yang, Y. H.; Chen, Y. T. *J Phys Chem B* **2006**, *110*, 17370-17374.

(44) Li, B.; Xie, Y.; Huang, J. X.; Qian, Y. T. *Adv Mater* **1999**, *11*, 1456-1459.

(45) Jiang, Y.; Wu, Y.; Mo, X.; Yu, W. C.; Xie, Y.; Qian, Y. T. *Inorg Chem* **2000**, *39*, 2964.

(46) Gou, X. L.; Cheng, F. Y.; Shi, Y. H.; Zhang, L.; Peng, S. J.; Chen, J.; Shen, P. W. *J Am Chem Soc* **2006**, *128*, 7222-7229.

(47) Castro, S. L.; Bailey, S. G.; Raffaelle, R. P.; Banger, K. K.; Hepp, A. F. *Chem Mater* **2003**, *15*, 3142-3147.

(48) Malik, M. A.; O'Brien, P.; Revaprasadu, N. *Adv Mater* **1999**, *11*, 1441-1444.

(49) Zhong, H. Z.; Li, Y. C.; Ye, M. F.; Zhu, Z. Z.; Zhou, Y.; Yang, C. H.; Li, Y. F. *Nanotechnology* **2007**, *18*.

(50) Allen, P. M.; Bawendi, M. G. *J Am Chem Soc* **2008**, *130*, 9240.

(51) Panthani, M. G.; Akhavan, V.; Goodfellow, B.; Schmidtke, J. P.; Dunn, L.; Dodabalapur, A.; Barbara, P. F.; Korgel, B. A. *J Am Chem Soc* **2008**, *130*, 16770-16777.

(52) Guo, Q.; Kim, S. J.; Kar, M.; Shafarman, W. N.; Birkmire, R. W.; Stach, E. A.; Agrawal, R.; Hillhouse, H. W. *Nano Lett* **2008**, *8*, 2982-2987.

(53) Tang, J.; Hinds, S.; Kelley, S. O.; Sargent, E. H. *Chem Mater* **2008**, *20*, 6906-6910.

(54) Todorov, T.; Cordoncillo, E.; Sanchez-Royo, J. F.; Carda, J.; Escribano, P. *Chem Mater* **2006**, *18*, 3145-3150.

(55) Ahn, S.; Kim, K.; Yoon, K. *Curr Appl Phys* **2008**, *8*, 766-769.

(56) El-Sayed, M. A. *Accounts Chem Res* **2004**, *37*, 326-333.

(57) Murray, C. B.; Norris, D. J.; Bawendi, M. G. *J Am Chem Soc* **1993**, *115*, 8706-8715.

(58) Sun, S. H.; Murray, C. B.; Weller, D.; Folks, L.; Moser, A. *Science* **2000**, *287*, 1989-1992.

(59) Park, J.; An, K. J.; Hwang, Y. S.; Park, J. G.; Noh, H. J.; Kim, J. Y.; Park, J. H.; Hwang, N. M.; Hyeon, T. *Nat Mater* **2004**, *3*, 891-895.

(60) Kwon, S. G.; Hyeon, T. *Accounts Chem Res* **2008**, *41*, 1696-1709.

(61) Peng, X. G.; Wickham, J.; Alivisatos, A. P. *J Am Chem Soc* **1998**, *120*, 5343-5344.

(62) Talapin, D. V.; Rogach, A. L.; Haase, M.; Weller, H. *J Phys Chem B* **2001**, *105*, 12278-12285.

(63) Casula, M. F.; Jun, Y. W.; Zaziski, D. J.; Chan, E. M.; Corrias, A.; Alivisatos, A. P. *J Am Chem Soc* **2006**, *128*, 1675-1682.

(64) Kwon, S. G.; Piao, Y.; Park, J.; Angappane, S.; Jo, Y.; Hwang, N. M.; Park, J. G.; Hyeon, T. *J Am Chem Soc* **2007**, *129*, 12571-12584.

(65) Koo, B.; Patel, R. N.; Korgel, B. A. *J Am Chem Soc* **2009**, *131*, 3134.

(66) Pan, D. C.; An, L. J.; Sun, Z. M.; Hou, W.; Yang, Y.; Yang, Z. Z.; Lu, Y. F. *J Am Chem Soc* **2008**, *130*, 5620.

(67) Kuo, K. T.; Chen, S. Y.; Cheng, B. M.; Lin, C. C. *Thin Solid Films* **2008**, *517*, 1257-1261.

(68) Kino, T.; Kuzuya, T.; Itoh, K.; Sumiyama, K.; Wakamatsu, T.; Ichidate, M. *Mater Trans* **2008**, *49*, 435-438.

(69) Nairn, J. J.; Shapiro, P. J.; Twamley, B.; Pounds, T.; von Wandruszka, R.; Fletcher, T. R.; Williams, M.; Wang, C. M.; Norton, M. G. *Nano Lett* **2006**, *6*, 1218-1223.

(70) Zhong, H. Z.; Zhou, Y.; Ye, M. F.; He, Y. J.; Ye, J. P.; He, C.; Yang, C. H.; Li, Y. F. *Chem Mater* **2008**, *20*, 6434-6443.

(71) Nakamura, H.; Kato, W.; Uehara, M.; Nose, K.; Omata, T.; Otsuka-Yao-Matsuo, S.; Miyazaki, M.; Maeda, H. *Chem Mater* **2006**, *18*, 3330-3335.

(72) Uehara, M.; Watanabe, K.; Tajiri, Y.; Nakamura, H.; Maeda, H. *J Chem Phys* **2008**, *129*.

(73) Wang, D. S.; Zheng, W.; Hao, C. H.; Peng, Q.; Li, Y. D. *Chem Commun* **2008**, 2556-2558.

(74) Du, W. M.; Qian, X. F.; Yin, J.; Gong, Q. *Chem-Eur J* **2007**, *13*, 8840-8846.

(75) Dutta, D. P.; Sharma, G. *Mater Lett* **2006**, *60*, 2395-2398.

(76) Binsma, J. J. M.; Giling, L. J.; Bloem, J. *J Cryst Growth* **1980**, *50*, 429-436.

(77) Connor, S. T.; Hsu, C. M.; Weil, B. D.; Aloni, S.; Cui, Y. *J Am Chem Soc* **2009**, *131*, 4962-4966.

(78) Qi, Y. X.; Liu, Q. C.; Tang, K. B.; Liang, Z. H.; Ren, Z. B.; Liu, X. M. *J Phys Chem C* **2009**, *113*, 3939-3944.

(79) Koo, B.; Patel, R. N.; Korgel, B. A. *Chem Mater* **2009**, *21*, 1962-1966.

(80) Nose, K.; Soma, Y.; Omata, T.; Otsuka-Yao-Matsuo, S. *Chem Mater* **2009**, *21*, 2607-2613.

(81) Batabyal, S. K.; Tian, L.; Venkatram, N.; Ji, W.; Vittal, J. J. *J Phys Chem C* **2009**, *113*, 15037-15042.

(82) Schimmel, M. I.; de Tacconi, N. R.; Rajeshwar, K. *J Electroanal Chem* **1998**, *453*, 187-195.

(83) Park, J. S.; Dong, Z.; Kim, S.; Perepezko, J. H. *J Appl Phys* **2000**, *87*, 3683-3690.

(84) Medvedeva, N. I.; Shalaeva, E. V.; Kuznetsov, M. V.; Yakushev, M. V. *Phys Rev B* **2006**, *73*.

(85) Gottschalk, H.; Patzer, G.; Alexander, H. *Phys Status Solidi A* **1978**, *45*, 207-217.

Chapter 2: Coalescence and interface diffusion in linear CdTe/CdSe/CdTe heterojunction nanorods†

2.1 INTRODUCTION

Heterojunction nanostructures can be colloidally synthesized in diverse pathways, leading formation of various heterostructure types.[1-12] The formation of extended defects in heterojunction nanocrystals is alleviated since the large surface area-to-volume ratio of colloidal nanocrystals and nanorods helps relieve strain at epitaxial interfaces between materials with large lattice mismatches.[2,16-18] Nonetheless, the relatively fast reconstruction of these interfaces[6-8,19-21] or the coalescence of non-spherical nanocrystals[6-8,22,23] were previously reported, which requires further study and better understanding of the dynamics of these processes.

In this chapter, the rates of heterojunction interdiffusion and coalescence of CdTe/CdSe/CdTe nanorods are reported and compared to model predictions. The Se and Te composition profiles were mapped in individual nanorods aged in hot solvents for different amounts of time to determine the Te in CdSe diffusion coefficient and evaluate the influence of strain on the interdiffusion rates across the heterojunctions. The measured rod-to-sphere coalescence rates were compared to rates predicted using a continuum viscous flow model for nanorod-to-sphere coalescence. Se and Te interdiffusion rates appear to be independent of strain at the CdSe/CdTe interface and the continuum model gives a reasonable approximation to the measured coalescence rates.

2.2 EXPERIMENTAL SECTION

Cadmium oxide (CdO, 99.5%), tellurium (Te, 99.8%), tributylphosphine (TBP, 97%), and toluene (99.8%) were purchased and used as received from Aldrich. n-

---

† The contents of this chapter appear in *Nano Letters* 8, 2490-2496 (**2008**).

Tetradecylphosphonic acid (TDPA, 97%) was purchased from Alfa Aesar. Tri-n-octylphosphine (TOP, 97%), trioctylphosphine oxide (TOPO, 99%), and selenium (Se, 99.99%) were purchased from STREM

2.2.1 Synthesis of CdTe/CdSe/CdTe heterojunction nanorods

A Cd-TDPA complex[86] was prepared by adding 0.963 g of CdO (7.5 mmol) and 4.185 g of TDPA (15 mmol) to 3 g of TOPO and degassing for one hour through pulling vacuum in the Schlenk line. The mixture was heated to 300 ℃ under nitrogen. It kept aged for 10 minutes until it turned optically clear, indicating that the Cd-TDPA complex formed. Subsequently, the clear Cd-TDPA solution was cooled at room temperature to be solidified and aged for more than 24 hr. This Cd-TDPA complex is important for making the CdSe nanorods, as its stability leads to distinct particle nucleation followed by slow controlled growth, which is necessary for nanorod formation.[6]

A mixture of 3.48 g of Cd-TDPA complex (3.2 mmol of Cd) and 4.65 g of TOPO was degassed in the reaction flask for one hour and then heated to 320 ℃ under nitrogen. A selenium precursor reactant solution was prepared by dissolving 0.126 g of Se (1.6 mmol) in a mixture of 0.468 mL of TBP, 3.482 mL of TOP, and 0.694 mL of toluene at 120 ℃. The tellurium reactant solution was made under the same condition except with an increased amount (5 mL) of TOP to lower the solution viscosity for easy injection through a syringe pump. The selenium precursor was rapidly injected into the mixture of Cd-TDPA and TOPO at 320 ℃. The temperature was then immediately decreased to 250 ℃. This temperature decrease promotes the formation of relatively high aspect ratio CdSe nanorods.[86] After heating for 30 minutes, the reaction solution was returned to 300 ℃ and then the tellurium precursor was injected by syringe pump for 7.5 minutes at a rate of 48 mL/hr, which yields CdTe/CdSe/CdTe heterojunction nanorods.[6]

13

2.2.1.1 Nanorod aging

After Te injection from the syringe pump was complete, the CdTe/CdSe/CdTe heterojunction nanorods were stirred in solution for 30 hr at 300 ºC. Nanorods were removed from solution at different times in ~0.5 mL aliquots for characterization. Prior to characterization, the nanorods in each aliquot were purified by precipitation with excess ethanol, followed by centrifugation. The precipitated nanorods were redispersed chloroform or toluene for characterization

2.2.2 Nanocrystal Characterization

Low resolution transmission electron microscopy (LRTEM) images were acquired using a Phillips EM280 microscope operated at an accelerating voltage of 80 kV. High resolution electron transmission microscopy (HRTEM) images were obtained using a JEOL 2010F microscope equipped with a field emission gun operated at 200 kV. TEM samples were prepared by drop-casting dilute solutions of nanorods from toluene onto a carbon-coated copper TEM grid (200-mesh, Ladd Research).

Energy dispersive X-ray spectroscopy (EDS) mapping was performed on an FEI TECNAI G2 F20 X-TWIN microscope in scanning transmission electron microscopy (STEM) mode at an accelerating voltage of 200 kV. Drift corrected spectrum profiles were obtained by initially selecting a reference area in STEM image and regulating the scanning direction not to stray from the reference area. The electron beam was focused to a spot size of ~0.5 nm in diameter. During EDS mapping, the dwell time was 1000 ms at a given position and the profile size was 400 positions per nanorod. The spatial resolution of this technique is ~1 nm.

X-ray diffraction (XRD) was performed on a Bruker-Nonius D8 Advance powder diffractometer with Cu K_α radiation ($\lambda = 1.54$ Å). Nanorods were evaporated from toluene onto quartz substrates and dried to make thick films (~200 µm). Diffraction

patterns were obtained at a scan rate of 12 deg / min in 0.01 deg increments for 12 hr, rotating the sample at 15 deg / min.

UV-visible absorbance spectra were collected on a Varian Cary 5000 Scan spectrophotometer and photoluminescence (PL) spectra were recorded using a Fluorolog-3 fluorometer with a 450W Xe source. The absorbance and PL spectra were measured at room temperature with nanocrystals dispersed in toluene. PL measurements were taken with nanorod concentrations adjusted so that the at the first exciton peak wavelength—which was also the excitation wavelength—was 0.1.

2.3 RESULTS AND DISCUSSION

2.3.1 Coalescence of linear CdTe/CdSe/CdTe heterojunction nanorods

Linear CdTe/CdSe/CdTe heterojunction nanorods were synthesized by high temperature arrested precipitation using a sequential reactant injection method.[6,87] In this procedure, CdSe nanorods first precipitate in an initial reaction step, followed by a subsequent controlled heterogeneous deposition of CdTe at the tips of the CdSe nanorods.

2.3.1.1 Nanorods aging without purification

Figure 2.1 shows transmission electron microscopy (TEM) images of a nanorod sample imaged at different times during a preparation. The initial CdSe nanorods (Figure 2.1a) have an initial average diameter and length of 4.2 nm and 19.6 nm. Immediately after adding Te-TOP, the nanorods grew by 2.5 nm on each end to 24.6 nm (Figure 2.1b). The nanorod diameter also increased slightly to 4.7 nm (by 0.5 nm), which corresponds to the adsorption of approximately one CdTe monolayer. The length and diameter histograms constructed from TEM images of these samples are shown in Figure 2.2. The nanorods are wurtzite crystals elongated in the (hexagonal) [001]

crystallographic direction (revealed in XRD data in Figure 2.3) and the linear deposition of CdTe on the polar CdSe (and CdTe) (001) surfaces (i.e., the ends of the nanorods) is approximately 10 times faster than the deposition on the non-polar sidewall surfaces.
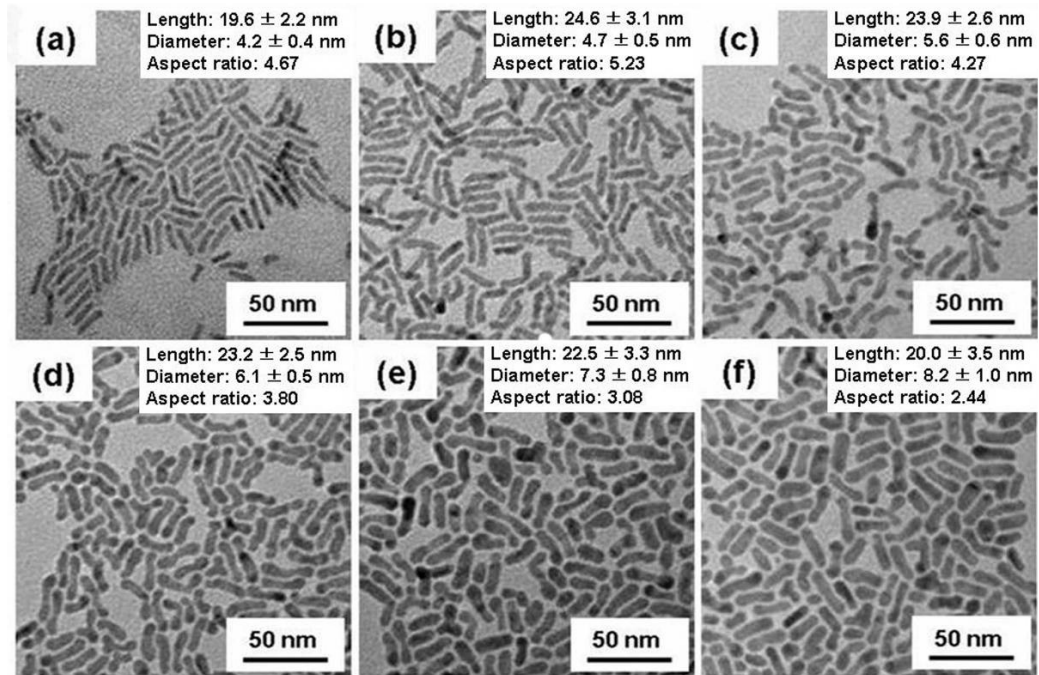
Figure 2.1. TEM images of (a) CdSe nanorods prior to CdTe deposition, and CdTe/CdSe/CdTe heterojunction nanorods (b) immediately after CdTe deposition and then after remaining in solution at 300 ^{o}C for (c) 10 min, (d) 1 hr, (e) 7 hr and (f) 30 hr.

(a)

$\overline{l} = 19.6$ nm
$\sigma = 2.2$ nm

$\overline{d} = 4.2$ nm
$\sigma = 0.4$ nm

(b)

$\overline{l} = 24.6$ nm
$\sigma = 3.1$ nm

$\overline{d} = 4.7$ nm
$\sigma = 0.5$ nm

(c)

$\overline{l} = 23.9$ nm
$\sigma = 2.6$ nm

$\overline{d} = 5.6$ nm
$\sigma = 0.6$ nm
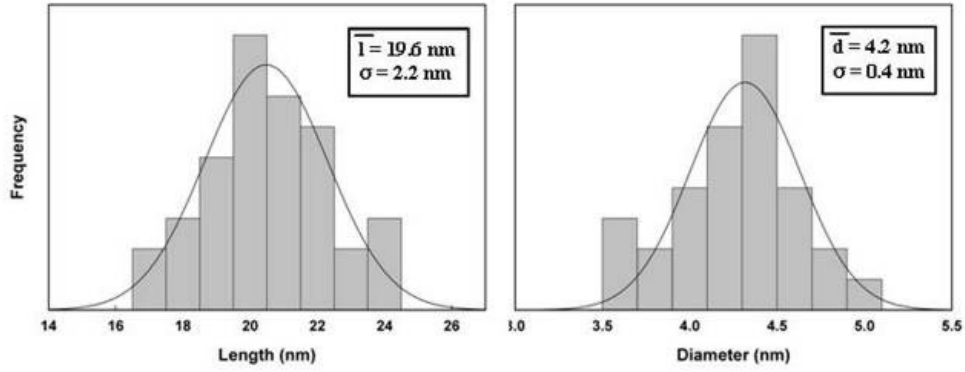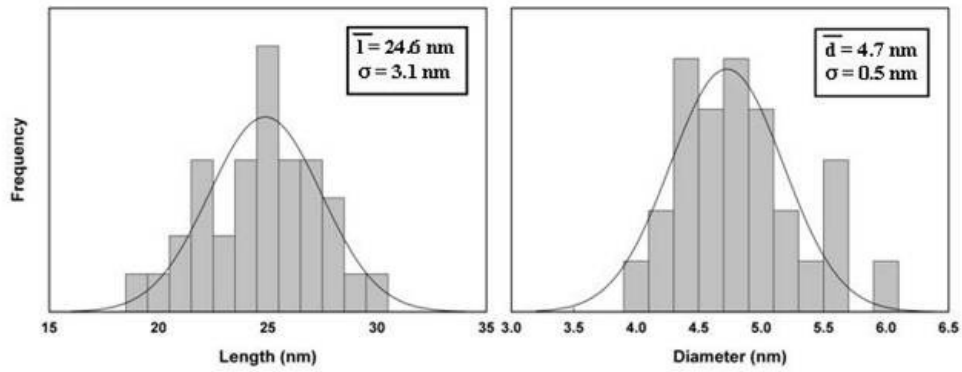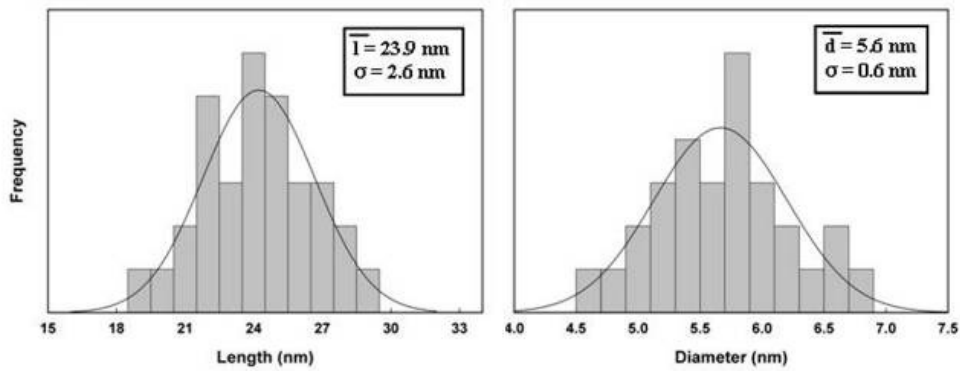
(d)
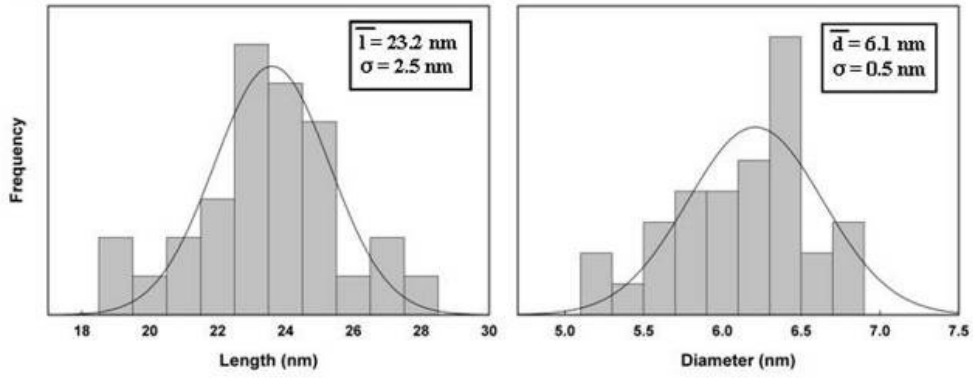
(e)
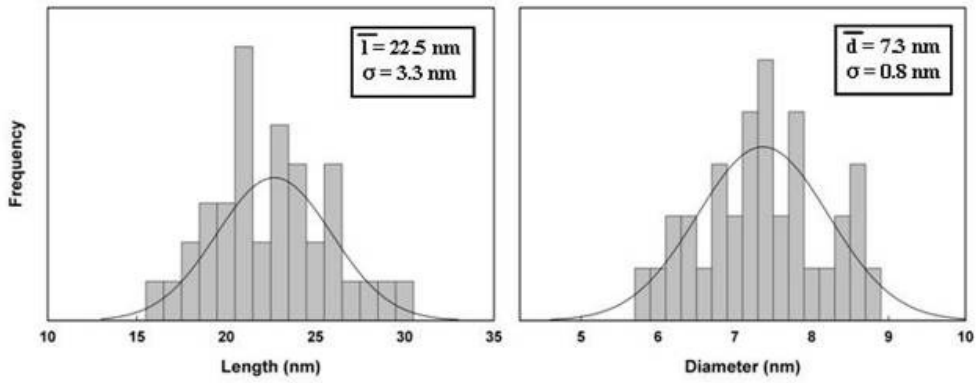
(f)
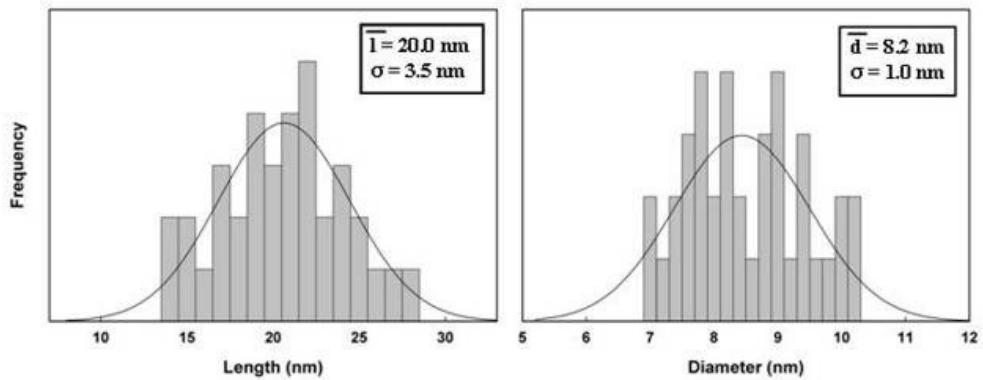
Figure 2.2. Histograms of length and diameter of (a) CdSe nanorods and the CdTe/CdSe/CdTe heterojunction nanorods after (b) initial CdTe deposition and then stirring in solution at 300 ºC for (c) 10 min, (d) 1 hr, (e) 7 hr, and (f) 30 hr. The nanorod dimensions were determined from TEM images. The histograms correspond to the nanorod samples imaged in Figure 2.1.

Figure 2.3 shows XRD data for CdTe/CdSe/CdTe nanorods as-synthesized and aged in solution. The broadened peaks in the range of $2\Theta = 40\sim50^o$ that appear after 10 minutes of aging in solution at 300^oC indicate that there is relatively significant Te/Se interdiffusion across the heterojunction. After 1 hour of aging in solution, the XRD peaks have broadened and shifted to lower angle, indicating that a significant amount of CdSe/CdTe alloying due to Se-Te interfdiffusion across the heterojunctions has occurred. After 30 hours of aging, the nanorods have formed a $CdSe_{0.4}Te_{0.6}$ alloy.
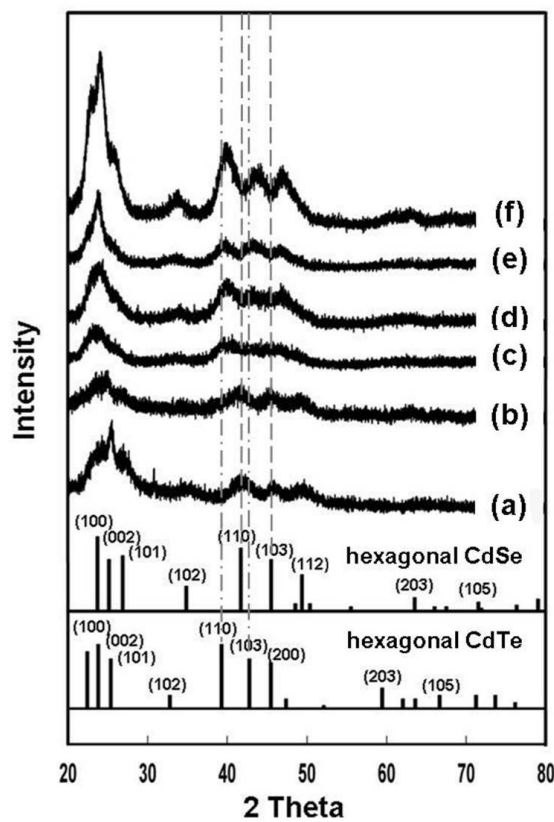
Figure 2.3. X-ray diffraction (XRD) of (a) CdSe nanorods prior to CdTe addition and CdTe/CdSe/CdTe heterojunction nanorods (b) immediately following CdTe deposition and after aging in solution at 300 ℃ for (c) 10min, (d) 1 hr, (e) 7 hr, and (f) 30 hr. The broadened peaks in the range of $2\Theta = 40\sim50$ ° in (c) result from the beginning of Te/Se interdiffusion. The XRD pattern (f) corresponds to CdSe$_{0.4}$Te$_{0.6}$ alloy with hexagonal crystal structure: d_{002} =3.66 Å, d_{110} =2.24 Å, giving $a_{CdSe_xTe_{1-x}}$ =4.48 Å, $c_{CdSe_xTe_{1-x}}$ =7.3 Å, which corresponds to the lattice parameters expected for CdSe$_{0.4}$Te$_{0.6}$.

The nanorods coalesce to shorter aspect ratios if they remain dispersed in the solvent at 300℃, as shown in Figure 2.1. At first, the CdTe ends coalesce before the central CdSe portion, giving the initial appearance of a dumbbell shape as has been observed previously for CdTe/CdSe/CdTe nanorods.[6-8] The nanorod diameter then becomes uniform as the nanorods continue to decrease in length. Figure 2.4 plots the length, radius, aspect ratio and volume of the nanorod sample shown in Figure 2.1. The length decreases continuously with the coalescence rate gradually slowing as the nanorods become more spherical. The nanorod volume, however, does not remain constant (Figure 2.4d). There is also a slow continued deposition of CdTe (and also CdSe) from unreacted precursors as the nanorods are coalescing.
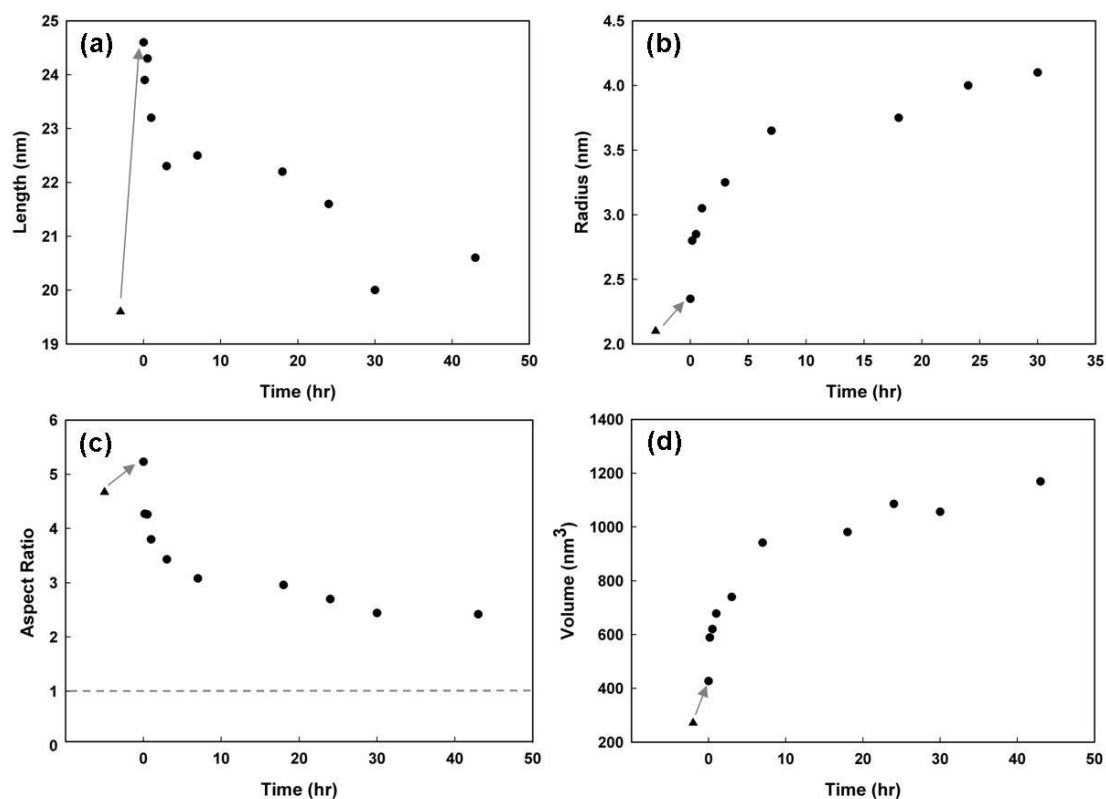
Figure 2.4.   (a) Length, (b) radius, (c) aspect ratio, and (d) volume of CdTe/CdSe/CdTe heterojunction nanorods (determined from TEM measurements) aged in solution at 300°C.   These samples correspond to the nanorods imaged in Figure 1.   The triangles correspond to the CdSe nanorods before CdTe deposition and the arrows indicate the change in dimensions immediately after Te-TOP addition to the reaction mixture.   The dotted line in (c) corresponds to the aspect ratio of sphere (= 1).   The (d) volume was estimated from the measured radius and length assuming a cylindrical geometry: $vol = \pi R^2 L$ (*R*: radius, *L*: length).

2.3.1.2 Nanorods aging after purification

To prevent this residual deposition during the aging process, nanorods were also studied that were purified after the initial CdTe deposition step and then redispersed in solution at 300 °C.   Figure 2.5 shows TEM images of CdTe/CdSe/CdTe nanorods

21

prepared in this way. Figure 2.6 shows plots of the length, radius, aspect ratio and volume of nanorods made using this procedure. The purification largely eliminates continued CdTe deposition; however, there is still a slight increase in nanocrystal volume during aging—from 800 to 1200 nm^3. It was not possible to cleanly separate the nanorods by antisolvent precipitation from unreacted precursor, but this procedure did help minimize further deposition. In both cases—with and without purification—the nanorods coalesce relatively rapidly in solution at 300°C, with decreases in aspect ratio from just over 5 to 2 (Figure 2.5) and nearly 1 (Figure 2.6) after 30 hours in solution. Figure 2.7 shows XRD data for the CdTe/CdSe/CdTe nanorods that were redispersed at 300°C after first purifying them to try to remove all residual reactants and then after 30 hours of aging. The XRD pattern corresponds to a $CdSe_{0.48}Te_{0.52}$ alloy.
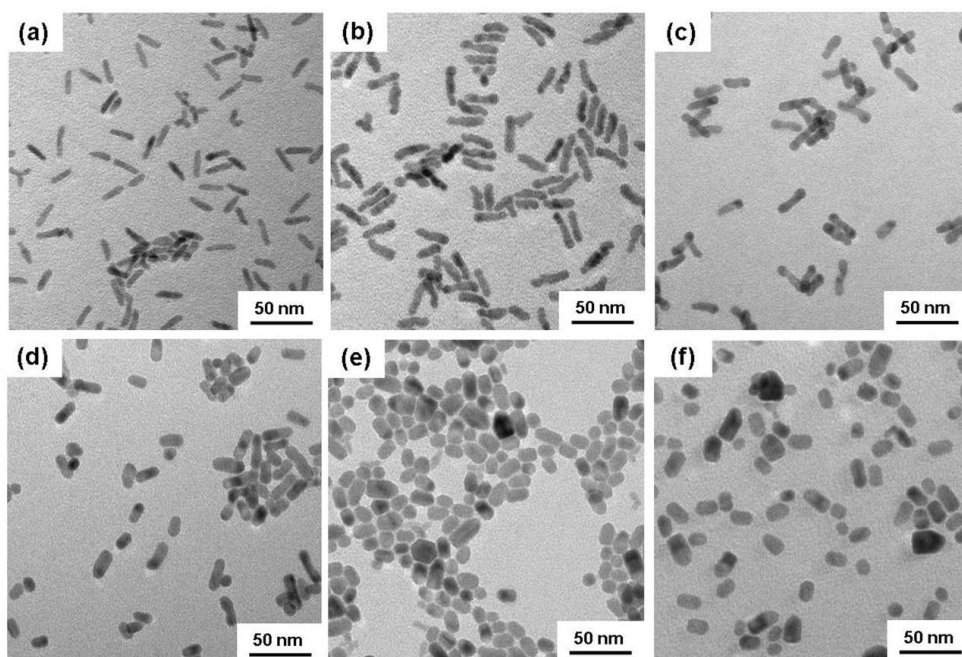
Figure 2.5. TEM images of CdTe/CdSe/CdTe heterojunction nanorods aged after purifying the as-formed CdTe/CdSe/CdTe nanorods prior to aging in solution at 300°C: (a) CdSe nanorods prior to CdTe deposition; (b) CdTe/CdSe/CdTe nanorods immediately after CdTe deposition; after redispersing the CdTe/CdSe/CdTe nanorods at 300°C for (c) 10 min, (d) 1 hr, (e) 7 hr, and (f) 30 hr.
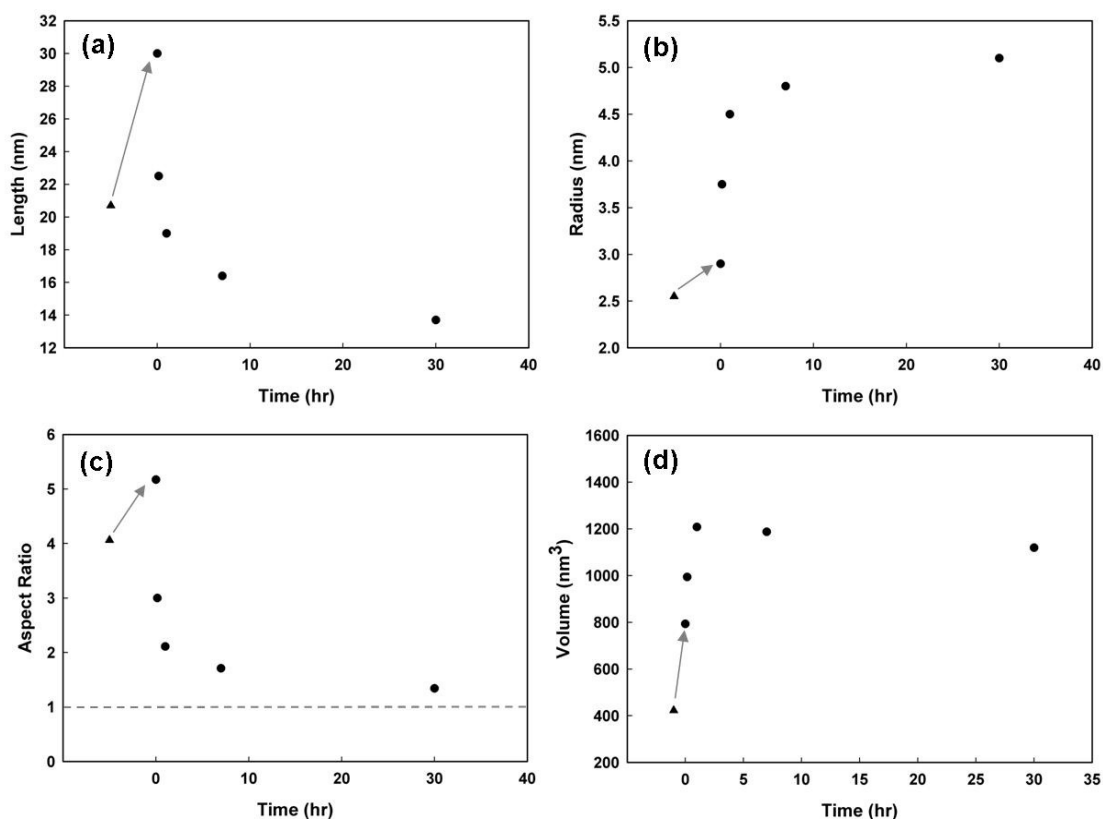
Figure 2.6. (a) Length, (b) radius, (c) aspect ratio, and (d) volume of CdTe/CdSe/CdTe heterojunction nanorods (determined from TEM measurements; representative images shown in Figure 2.5) aged in solution at 300°C. These nanorods were subjected to a purification step immediately after the addition of the Te-TOP reactant to try to remove unreacted precursor. The triangles correspond to the CdSe nanorods before CdTe deposition and the arrows indicate the change in dimensions immediately after Te-TOP addition to the reaction mixture. The dotted line in (c) corresponds to the aspect ratio of sphere (= 1). The (d) volume was estimated from the measured radius and length assuming a cylindrical geometry: $vol = \pi R^2 L$ (R: radius, L: length).

23
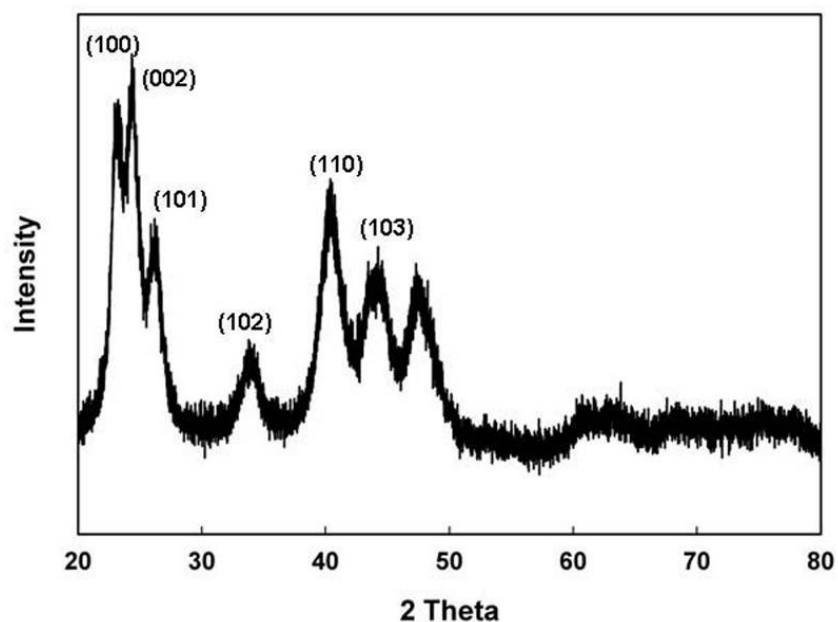
Figure 2.7. XRD of the coalesced nanorods imaged by TEM in Figure 2.5f, which have been aged in solution at $300^{\circ}C$ for 30 hr after an initial purification step. The lattice constants of $a = 4.4$ Å and $c = 7.26$ Å determined from the (002) and (110) peak positions, $d_{002} = 3.63$ Å and $d_{110} = 2.20$ Å correspond to a final alloy composition of $CdSe_{0.48}Te_{0.52}$, which is consistent with the volume change measured and plotted in Figure 2.6.

2.3.2 Continuum viscous model

The coalescence of rod-shaped nanoparticles has been examined in some detail for particles formed in aerosol (gas-phase) processes,[88,89] but such analyses have not yet been extended to nanorods in solution, even though the fundamental rate processes are identical, with coalescence to spheres being driven by the surface tension gradient on the particle surface arising from the non-spherical shape. One way to estimate the coalescence rate is to assume that continuum viscous flow applies to the nanorods and to then take mass and energy balances to obtain a relationship between the coalescence time t, and the nanorod length L, and radius r. As a similar approach to that of Hawa and

Zachariah the relationships between the nanorod length and radius and coalescence time from such a continuum viscous flow model are:[88]

$$t = -\frac{12\eta}{\sigma} \int_{L_0}^{L} \left(\sqrt{\frac{\pi}{V}} L^{3/2} - 2 \right)^{-1} dL \qquad (2.1)$$

$$t = \frac{24\eta}{\sigma} \int_{R_0}^{R} \left(1 - \frac{2\pi r^3}{V} \right)^{-1} dr. \qquad (2.2)$$

In Eqns (2.1) and (2.2), the nanorod volume V, does not change with time (i.e., mass is conserved). L_0 and R_0 are the initial length and radius. The coalescence rate in this viscous flow model depends on the two materials-dependent parameters of viscosity and the surface tension, η and σ. For a fluid, η and the diffusion coefficient D, can be related by the Eyring equation:

$$\eta = \frac{kT}{a_0 D} \qquad (2.3)$$

where k is Boltzmann's constant, T is the temperature and a_0 is the interatomic spacing. Since the nanorods are well below the melting temperatures of CdTe and CdSe, the use of Eqn (2.3) to determine η provides only an upper bound to the nanorod coalescence rate. A more accurate relationship between an effective viscosity of a crystal with a nanoscale domain size and its solid-state diffusion coefficient has been derived by Herring:[90]

$$\eta = \frac{kTR^2}{4\Omega_0 D} \qquad (2.4)$$

In Eqn (2.4), R is the nanorod radius and Ω_0 is the atomic volume in the solid. The value of η determined using Eqn (2.4) is close to two orders of magnitude higher than η calculated using Eqn (2.3). The expression for η in Eqn (2.4) yields the same functional form of the coalescence frequency as that predicted by Friedlander and Wu[89] for coalescing solid particles, indicating that the use of the viscous flow model equations

(2.1) and (2.2), combined with Eqn (2.4) should provide a reasonable approximation for the coalescence rate of the nanorods.

2.3.2.1 Model prediction

To quantitatively compare the coalescence rates predicted by Eqns (2.1) and (2.2), the extra CdTe deposition on the CdTe/CdSe/CdTe nanorods that occurs during the aging process must be subtracted from the total volume of the nanorods to determine the reduction in length by coalescence. This was done by subtracting the (measured) additional particle volume from the initial CdTe/CdSe/CdTe nanorod volume and considering that the deposition rate on the ends of the nanorods is 10 times as fast as the sidewall deposition. Figure 2.8 plots the (corrected) nanorod length and radius as a function of aging time. The best fits of Eqns (2.1) and (2.2) to the data in Figure 2.8 give estimates of σ/η equal to 12 and 24 nm/hr for the two different sets of experiments. These values are about an order of magnitude lower than those calculated using Eqn (2.3) and the bulk values of the CdSe surface tension and diffusion coefficient. Note that, for the calculations, values of $D = 2\times10^{-17}$ cm^2/sec (Te into CdSe),[91] $\sigma = 0.5$ J/m^2,[92,93] $\Omega_o = 0.0547\,\text{nm}^3$, $a_o = 2.8\times10^{-10}$ m, and averaged R values of 3.4 nm and 4.2 nm for Eqn (2.4), were used. And the best fit values of σ/η =12 nm/hr and σ/η =24 nm/hr are slightly higher than the values of σ/η =6.4 nm/hr and σ/η =4.2 nm/hr predicted using Eqn (2.4) to estimate η. Therefore, it appears that the continuum viscous flow model provides an upper bound for the coalescence rate when used in conjunction with the Eyring equation (Eqn (2.3)) to relate η and D, and perhaps a lower bound for the coalescence rate when Herring's equation relating η and D (Eqn (2.4)) is used.
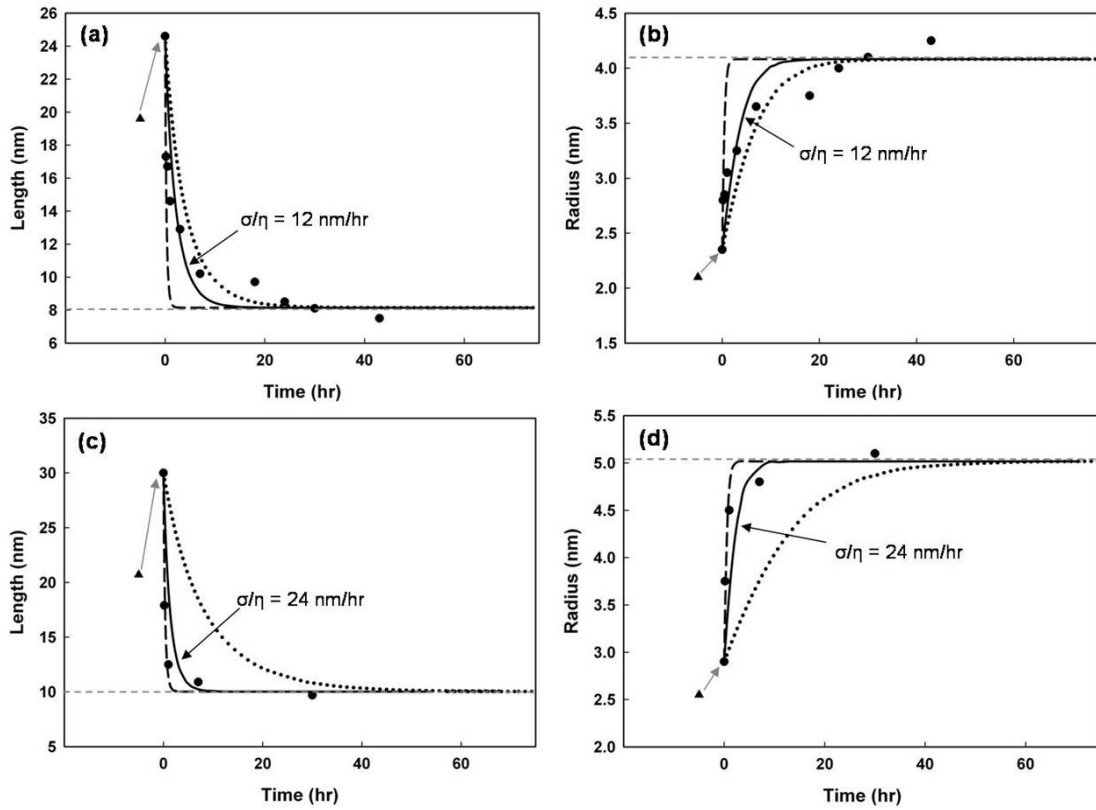
Figure 2.8. Corrected (a, c) length and (b, d) radius versus aging time (solid dots) in TOP/TOPO solution at 300°C and model predictions using Eqns (2.1) and (2.2) (solid, dashed and dotted lines). The data in (a) and (b) correspond to the nanorod samples imaged in Figure 2.1 and the data in (c) and (d) correspond to the "purified" nanorod samples imaged in Figure 2.5. The dashed and dotted curves in (a-d) are plots of Eqns (2.1) and (2.2) calculated using Eqns (2.3) and (2.4), respectively to determine η. Using bulk values of D, σ, Ω_0, a_0, and averaged values of R, gave σ/η = 96 nm/hr (dashed curves) using Eqn (2.3) and σ/η =6.4 nm/hr (dotted curves in (a) and (b)) and σ/η =4.2 nm/hr (dotted curves in (c) and (d)) using Eqn (2.4). The solid curves are the best fits of Eqns (2.1) and (2.2) to the data. The horizontal dotted lines indicate the nanorod lengths and radii for spherical particles with the same volume as the starting nanorods (i.e., the final limiting condition when the aspect ratio equals 1).

27

2.3.3 Interface diffusion in linear CdTe/CdSe/CdTe heterojunction nanorods

As the nanorods age in solution at 300°C, Se and Te interdiffusion occurs across the heterojunctions, as illustrated in Figure 2.9. The interdiffusion is observable by XRD (Figure 2.3) and nanobeam energy dispersive X-ray spectroscopy (EDS) mapping (Figure 2.10). By measuring the rate of Te-Se interdiffusion at the heterojunctions, D for Te diffusion into CdSe can be estimated and compared to bulk values. A solution to the time-dependent diffusion equation ($\partial C/\partial t = D\left(\partial^2 C/\partial t^2\right)$) provides a relationship between the Te concentration profile and D:

$$C(x,t) = \frac{Q}{\sqrt{\pi D t}} \exp\left(-\frac{x^2}{4Dt}\right). \tag{2.5}$$

In Eqn (2.5), x is the distance from the end of the rod, t is the aging time and Q is the amount of CdTe initially deposited at the end of the nanorod. Therefore, D can be estimated by determining the *diffusion length*, $\ell = \sqrt{Dt}$, which is the position at which the Te concentration decreased to $1/e$ the value of the peak concentration, as a function of aging time.[94,95] From EDS data like that shown in Figure 2.10, ℓ was determined for four different nanorods at four different aging times.
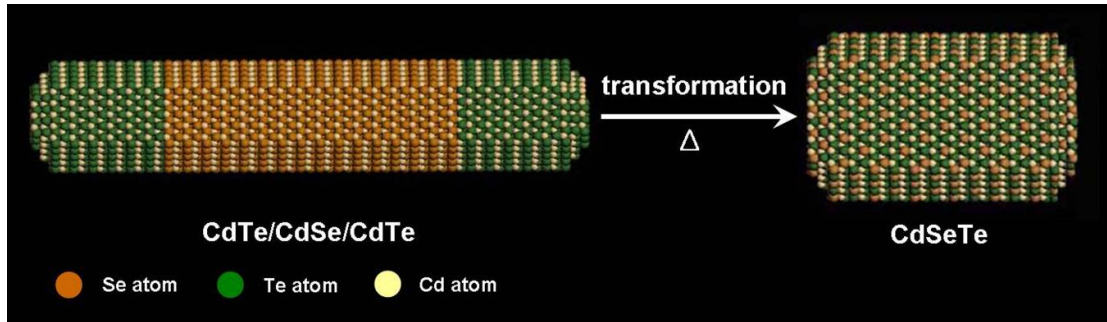
Figure 2.9. Se and Te interdiffusion at the CdSe/CdTe interfaces leads to transformation of CdTe/CdSe/CdTe heterojunction nanorods into alloyed CdSeTe nanoparticles.
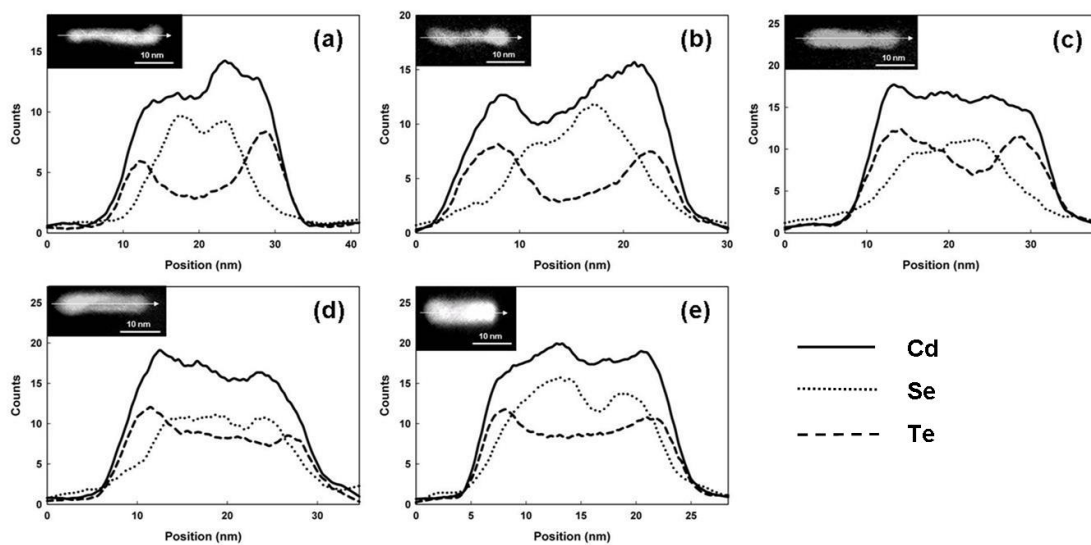
Figure 2.10. Cd, Se, and Te composition profiles measured by nanobeam EDS down the length of individual CdTe/CdSe/CdTe heterostructure nanorods: (a) immediately after CdTe deposition at the ends of the CdSe nanorods, and after aging in solution at 300 ºC for (b) 10min, (c) 1 hr, (d) 7 hr, and (e) 30 hr.   (Insets) Dark-field STEM images of the corresponding nanorods.   The arrow indicates the line scan direction.   The undulations in the concentration profiles result from slight fluctuations in nanorod diameter along the nanorod length.

2.3.3.1 Determination of diffusion length

To determine the Te diffusion length in the nanorods after different aging times, the edge of the Te profile in the center of each nanorod was estimated as illustrated in Figure 2.11.   An exact determination of the Te edge was complicated by the fact that the Te composition could not be monitored in one nanorod as it aged in solution and additionally that the average nanorod length decreased as a result of coalescence. Nonetheless, the edge of the heterojunction interface could be estimated with reasonable accuracy by examining the Te profiles in several different nanorods and averaging their diffusion lengths.   Figure 2.12 shows additional plots of the Se to Cd and Te to Cd ratios

determined from the EDS maps to further illustrate how the diffusion length was determined. These plots reveal that significant Se and Te interdiffusion has occurred after 1 hour of aging in solution and that after 7 hours of aging the Se and Te concentrations have become uniform.
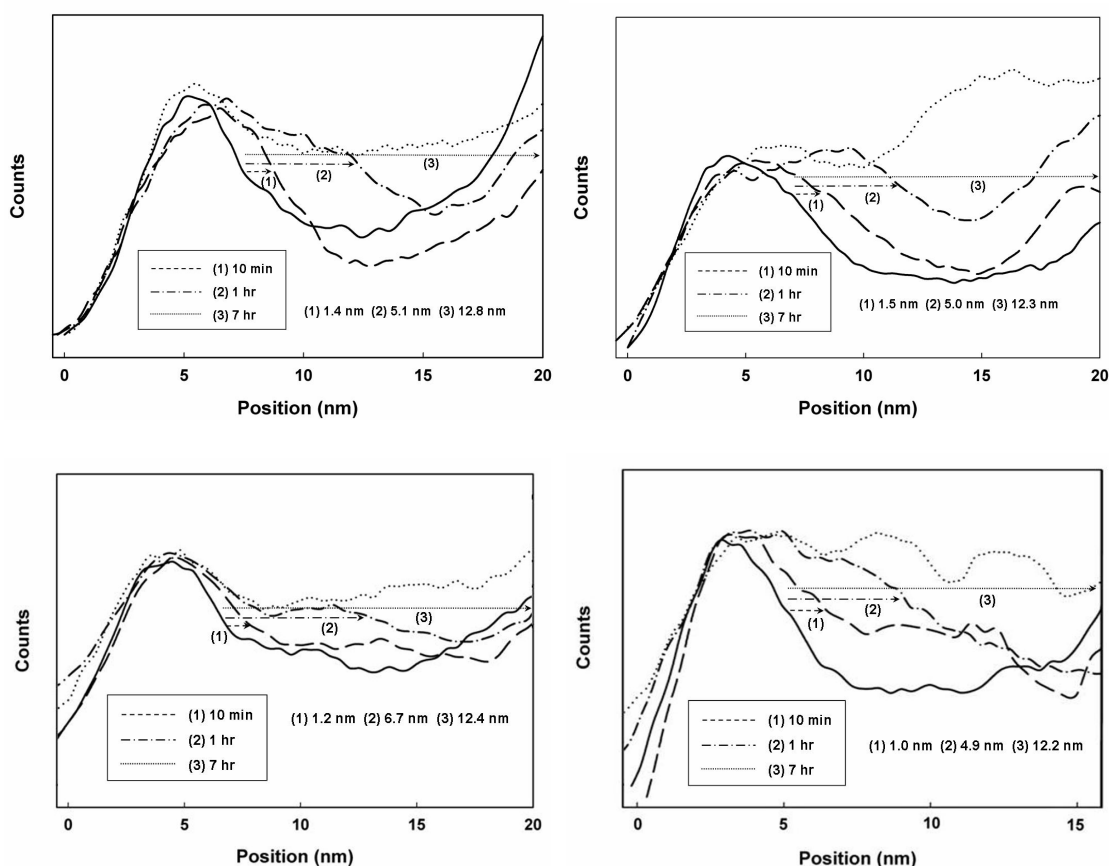
Figure 2.11. Nanobeam EDS maps of Te for four different nanorods after different aging times, illustrating how the diffusion lengths were determined. The average nanorod length decreased over time due to their coalescence, so the Te profiles are shown only at one end of the nanorods. However, to estimate the average diffusion length with aging time, both ends of the nanorods were examined. After 7 hr of aging, the Te and Se concentration profiles became uniform (with the exception of a small amount of residual Te deposition at the ends of the nanorods, as discussed above) and the diffusion lengths were estimated as half the nanorod length.
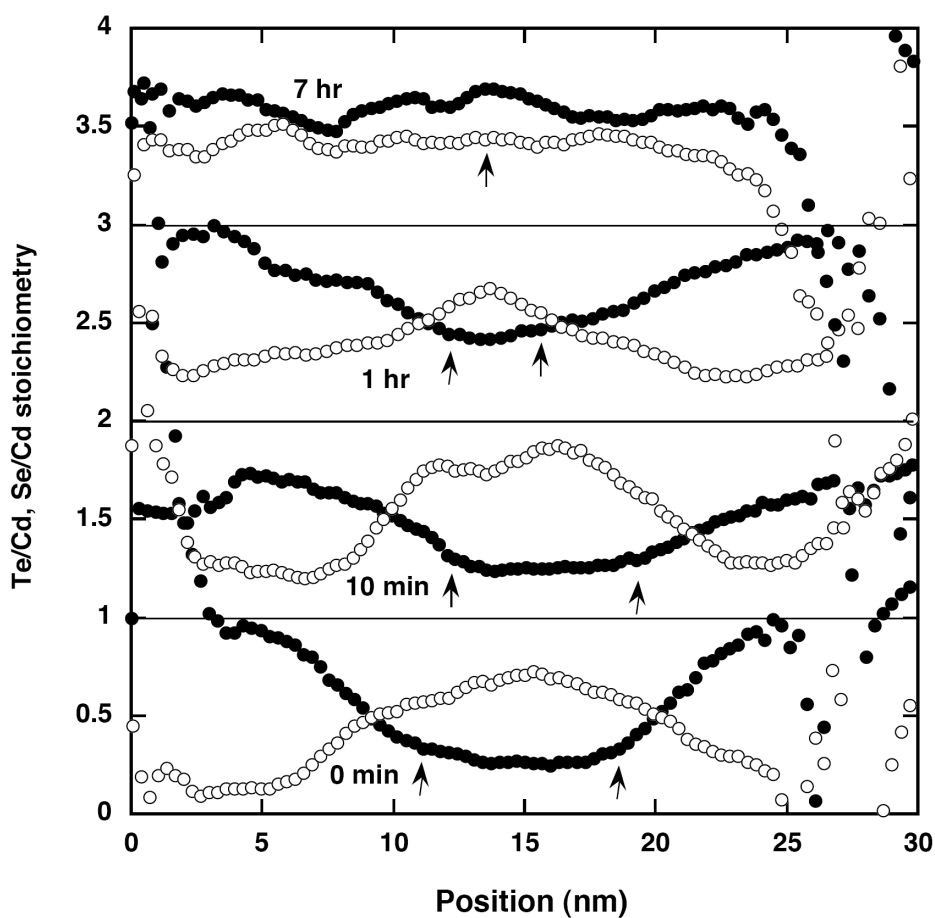
Figure 2.12. Te/Cd (●) and Se/Cd (o) stoichiometry determined from EDS mapping data as a function of position along the length of four nanorods isolated after the aging times indicated in the plot. The curves are offset in the vertical direction. The arrows indicate the Te edge in the nanorods. The Te present in the mid-section of the nanorods is the result of sidewall deposition. After 7 hours of aging, the Te and Se compositions are uniform along the lengths of the nanorods with a slight excess of Te relative to Se, which is consistent with XRD data and results from continued Te deposition from residual reactant as the nanorods are aged in solution. Note that the compositions at the ends of the nanorods exhibit a significant amount of scatter and in some cases deviate above 1 or below 0 as a result of the relatively small measurement signals as the diameter narrows abruptly at the ends of the nanorods.

2.3.3.2 Determination of diffusion coefficient

Performing the elemental maps on each nanorod is a relatively time intensive process and it is not practical to measure tens or hundreds of nanorods; however, elemental maps of four nanorods at each aging time were obtained and averaged to minimize the error in ℓ as much as possible. Figure 2.13 shows a plot of ℓ^2 versus the aging time, showing a linear dependence that indicates that strain at the CdTe/CdSe interface (Figure 2.14) is not affecting D.[94,95] A linear curve fit to the data in Figure 7 gives a value of $D = 1.5 \times 10^{-17}$ cm^2/sec, which is close to the literature value[91] of 2×10^{-17} cm^2/sec.
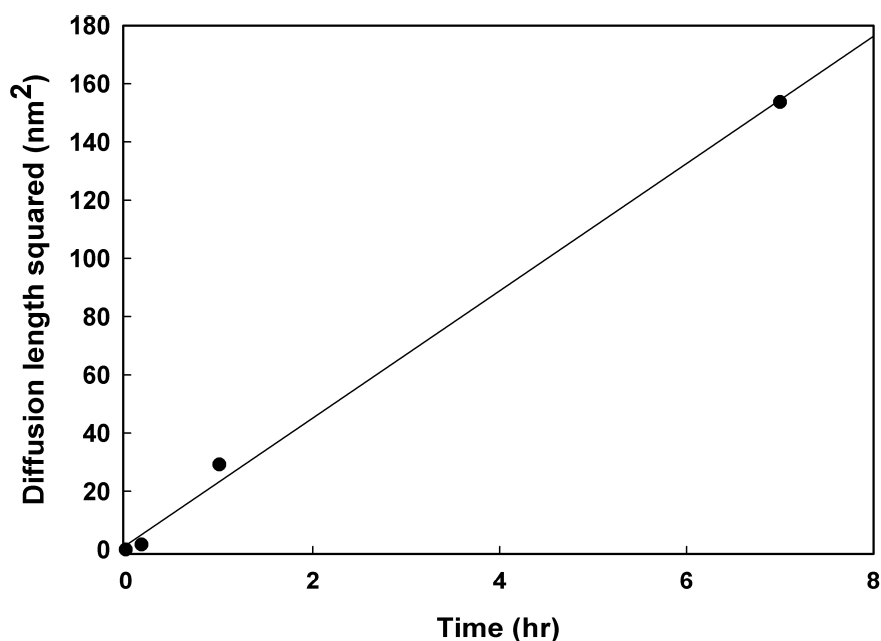
Figure 2.13. Plot of the square of the Te diffusion length measured by EDS mapping versus aging time. D estimated from a linear fit of the data to Eqn (2.5) is 1.5×10^{-17} cm^2/sec. (Each point on the plot is a diffusion length averaged for four different nanorods—as shown in Figures 2.11 and 2.12.)

2.3.3.3 Strain at the interface

Figure 2.14 shows high resolution TEM images of a CdTe/CdSe/CdTe nanorod and FFTs taken at different positions along the nanorod. The crystal structure of the tips of the nanorod matches CdTe, whereas the center of the nanorod matches CdSe. At the interface between the CdTe ends and the CdSe cores, the lattice spacing gradually changes from CdTe to CdSe and there is no sign of a dislocation at the heterojunction.
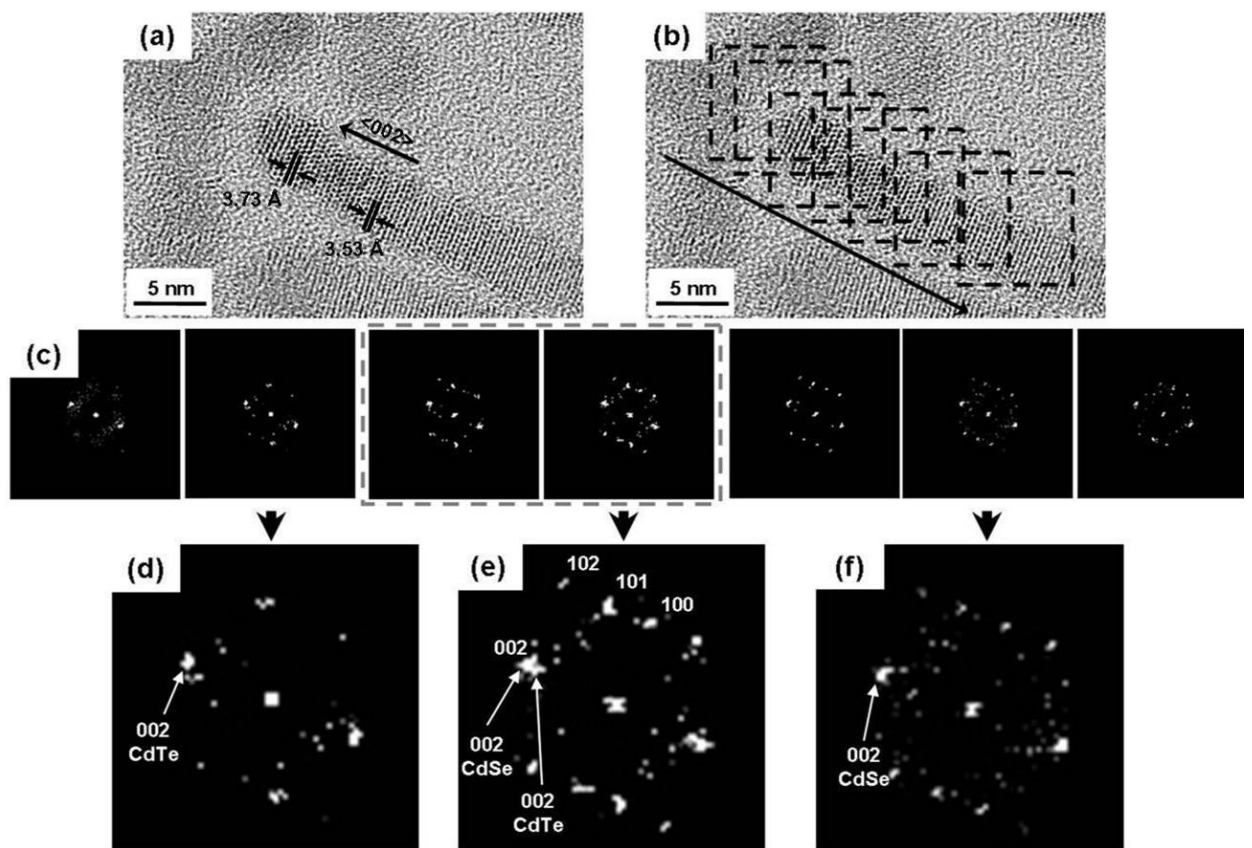
Figure 2.14. (a) High-resolution TEM image of a CdTe/CdSe/CdTe heterojunction nanorod. (c) FFTs of the regions of the nanorod outlined by the squares in (b) from top left to bottom right. The zone axis in (b) is [2110]. The nanorod is elongated in the [002] direction. (d)-(f) Higher magnification of the second, fourth, and sixth FFTs in (c). (d) and (f) match the expected diffraction patterns for CdTe and CdSe, respectively, and the diffraction spots in (e) are slightly broadened compared to a pure sum of spots of CdTe and CdSe, indicative of the existence of different lattice spacings made by strain at the interface.

33

2.4 CONCLUSIONS

In summary, both coalescence and Te-Se interdiffusion occur as CdTe/CdSe/CdTe nanorods are aged in solution at 300°C. The rates of Se-Te interdiffusion and nanorod coalescence were measured. Although there is strain at the epitaxial CdTe/CdSe interface due to the lattice mismatch, this strain does not appear to influence the rate of Te-Se interdiffusion. A continuum viscous flow model provided a reasonable approximation of the measured coalescence rates.

2.5 REFERENCES

(1)   Mews, A.; Eychmuller, A.; Giersig, M.; Schooss, D.; Weller, H. *J Phys Chem-Us* **1994**, *98*, 934-941.

(2)   Kamalov, V. F.; Little, R.; Logunov, S. L.; ElSayed, M. A. *J Phys Chem-Us* **1996**, *100*, 6381-6384.

(3)   Dorfs, D.; Eychmuller, A. *Z Phys Chem* **2006**, *220*, 1539-1552.

(4)   Manna, L.; Scher, E. C.; Li, L. S.; Alivisatos, A. P. *J Am Chem Soc* **2002**, *124*, 7136-7145.

(5)   Mokari, T.; Rothenberg, E.; Popov, I.; Costi, R.; Banin, U. *Science* **2004**, *304*, 1787-1790.

(6)   Shieh, F.; Saunders, A. E.; Korgel, B. A. *J Phys Chem B* **2005**, *109*, 8538-8542.

(7)   Halpert, J. E.; Porter, V. J.; Zimmer, J. P.; Bawendi, M. G. *J Am Chem Soc* **2006**, *128*, 12590-12591.

(8)   Kumar, S.; Jones, M.; Lo, S. S.; Scholes, G. D. *Small* **2007**, *3*, 1633-1639.

(9)   Jones, M.; Kumar, S.; Lo, S. S.; Scholes, G. D. *J Phys Chem C* **2008**, *112*, 5423-5431.

(10)   Milliron, D. J.; Hughes, S. M.; Cui, Y.; Manna, L.; Li, J. B.; Wang, L. W.; Alivisatos, A. P. *Nature* **2004**, *430*, 190-195.

(11)   Yong, K. T.; Sahoo, Y.; Swihart, M. T.; Prasad, P. N. *Adv Mater* **2006**, *18*, 1978.

(12)   Robinson, R. D.; Sadtler, B.; Demchenko, D. O.; Erdonmez, C. K.; Wang, L. W.; Alivisatos, A. P. *Science* **2007**, *317*, 355-358.

(13)   Chen, X. B.; Lou, Y. B.; Samia, A. C.; Burda, C. *Nano Lett* **2003**, *3*, 799-803.

(14)   Shenoy, V. B. *Phys Rev B* **2005**, *71*.

(15)   Dingreville, R.; Qu, J. M.; Cherkaoui, M. *J Mech Phys Solids* **2005**, *53*, 1827-1854.

(16)   Wang, Y. L.; Cai, L.; Xia, Y. N. *Adv Mater* **2005**, *17*, 473.

(17)   Peng, S.; Sun, S. H. *Angew Chem Int Edit* **2007**, *46*, 4155-4158.

(18)   Yin, Y. D.; Erdonmez, C. K.; Cabot, A.; Hughes, S.; Alivisatos, A. P. *Adv Funct Mater* **2006**, *16*, 1389-1399.

(19)   Puntes, V. F.; Krishnan, K. M.; Alivisatos, A. P. *Science* **2001**, *291*, 2115-2117.

(20)   Jun, Y. W.; Jung, Y. Y.; Cheon, J. *J Am Chem Soc* **2002**, *124*, 615-619.

(21)   Peng, Z. A.; Peng, X. G. *J Am Chem Soc* **2002**, *124*, 3343-3353.

(22)   Saunders, A. E.; Koo, B.; Wang, X. Y.; Shih, C. K.; Korgel, B. A. *Chemphyschem* **2008**, *9*, 1158-1163.

(23)   Hawa, T.; Zachariah, M. R. *Phys Rev B* **2007**, *76*.

(24)   Friedlander, S. K.; Wu, M. K. *Phys Rev B* **1994**, *49*, 3622-3624.

(25)   Herring, C. *Cc/Phys Chem Earth* **1979**, P16-P16.

(26)   Kokkonis, P.; Leute, V. *Solid State Ionics* **2005**, *176*, 2681-2688.

(27)   Balasubramanian, R.; Wilcox, W. R. *Int J Thermophys* **1990**, *11*, 25-35.

(28)   Kumikov, V. K.; Khokonov, K. B. *J Appl Phys* **1983**, *54*, 1346-1350.

(29)   Khreis, O. M. *Solid State Commun* **2004**, *132*, 767-771.

(30)   Gillin, W. P.; Dunstan, D. J. *Phys Rev B* **1994**, *50*, 7495-7498.

Chapter 3: Synthesis of CuInSe$_2$ Nanocrystals with Trigonal Pyramidal Shape†

3.1 INTRODUCTION

The ternary I-III-VI$_2$ chalcopyrite materials like CuInSe$_2$ are particularly interesting candidates for PVs due to their photostability, high light absorption coefficient and demonstrated high device efficiency.[41]   In particular, the colloidal nanocrystals are beneficial for lower cost PVs since they could be synthesized in large quantities and then dispersed in solvents for low-temperature deposition on various substrates.[30]   However, there are only a few examples of the nanocrystal synthesis of CuInSe$_2$ and other I-III-VI$_2$ chalcopyrite compounds in solution[43-50] and moreover the reported CuInSe$_2$ nanocrystals possessed relatively broad size distributions, composition and phase impurities, and poor dispersibility.

In this chapter, the developed synthetic method of monodisperse chalcopyrite (tetragonal) CuInSe$_2$ nanocrystals is provided.   The nanocrystals have trigonal pyramidal shape with one polar and three non-polar surface facets.   When drop-cast onto carbon substrates, the nanocrystals self-assemble into close-packed monolayers with triangular (honeycomb) lattice structure.

3.2 EXPERIMENTAL SECTION

Copper(I) chloride (CuCl, Aldrich, 99.995+ %) and indium(III) chloride (InCl$_3$, Aldrich, 99.999 %), selenourea (99+ %, STREM; 99.9+ %, ACROS), oleylamine (Fluka) were purchased and used as received.

---

† Portions of this chapter appear in *Journal of the American Chemical Society* 131, 3134–3135 (**2009**).

3.2.1 Nanocrystal Synthesis

In a typical synthesis, a mixture of 0.05 g of CuCl (0.5 mmol of Cu), 0.11 g of InCl$_3$ (0.5 mmol of In), and 10 mL of oleylamine is vigorously stirred and degassed in the reaction flask for 30 minutes at 60 ºC by pulling vacuum on the Schlenk line. The mixture is then heated to 130 ºC under nitrogen for 10 minutes. During heating, the solution turns from blue to yellow, indicating the formation of oleylamine complexes with Cu and In. Meanwhile, the selenium reactant solution is prepared by dissolving 0.123 g of selenourea (1.0 mmol) in 1 mL of oleylamine at 200 ºC under nitrogen on a Schlenk line. This In/Cu/oleylamine reactant solution is cooled to 100ºC and the selenium reactant solution is added by syringe. Immediately after injection of the Se reactant, the reaction mixture is heated to 240 ºC at a rate of 15 ºC/min. After 1 hour, the nanocrystals are removed from the heating mantle and allowed to cool to room temperature. 30 mL of ethanol is then added to precipitate the nanocrystals, followed by centrifugation at 7000 rpm for 3 minutes. The supernatant is discarded. The nanocrystals redisperse in a variety of non-polar organic solvents, including chloroform, hexane, and toluene. Prior to characterization, dispersions are typically centrifuged again at 7000 rpm for 5 min to remove inadequately capped nanocrystals. A typical reaction yields ~120 mg of CuInSe$_2$ nanocrystals.

3.2.1.1 Use of selenourea

The use of selenourea as the Se reactant turned out to be relatively important. Initially, we tried to use trioctylphosphine:selenium (TOP:Se), commonly used for CdSe and ZnSe nanocrystal synthesis,[57,96] but this did not work well. The presence of the phosphine was found to inhibit the formation of the chalcopyrite compound, most likely by forming relatively strong phosphine complexes with Cu and In. Oleylamine dissolves CuCl and InCl$_3$ upon heating to provide a Cu and In reactant solution, and then

bonds well to the CuInSe$_2$ surface to provide an effective steric barrier between particles to prevent their aggregation.
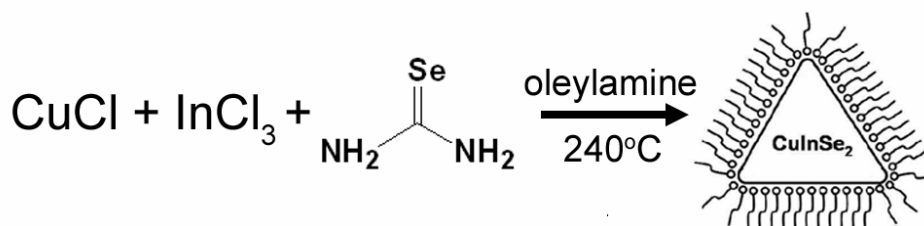
Figure 3.1.   Reaction scheme for CuInSe$_2$ nanocrystal synthesis.

3.2.2 Characterization methods

TEM images were acquired using either a Phillips EM280 microscope operated at 80 kV or a JEOL 2010F microscope equipped with a field emission gun operated at 200 kV.   TEM samples were prepared by drop-casting nanocrystals dispersed in chloroform onto carbon-coated nickel TEM grids (200-mesh, Electron Microscopy Sciences).   The JEOL 2010F is equipped with an Oxford EDS detector, which was used for elemental analysis of the nanocrystal composition.

3.3 RESULTS AND DISCUSSION

3.3.1 Synthesis of CuInSe$_2$ Nanocrystals

TEM images of CuInSe$_2$ nanocrystals are shown in Figures 3.2 and 3.3.   The nanocrystals are monodisperse with triangular shape and crystalline.   By energy dispersive X-ray spectroscopy (EDS), the 1:1:2 Cu:In:Se stoichiometry of the

nanocrystals was 1:1:2 and X-ray diffraction (XRD) confirmed their chalcopyrite (tetragonal) (JCPDS Card No. 40-1487) crystal structure (Figure 3.4). The {112} and {220} lattice spacings of $CuInSe_2$ were visible in many of the nanocrystals imaged by high resolution TEM. The optical properties of the nanocrystals are also consistent with chalcopyrite $CuInSe_2$. The optical gap determined from room temperature absorbance spectra of the nanocrystals dispersed in chloroform (Figure 3.5) of 1 eV, matches the bulk band gap of chalcopyrite $CuInSe_2$ (E_g = ~1 eV). Note that the nanocrystals are not small enough to exhibit quantum confinement effects.
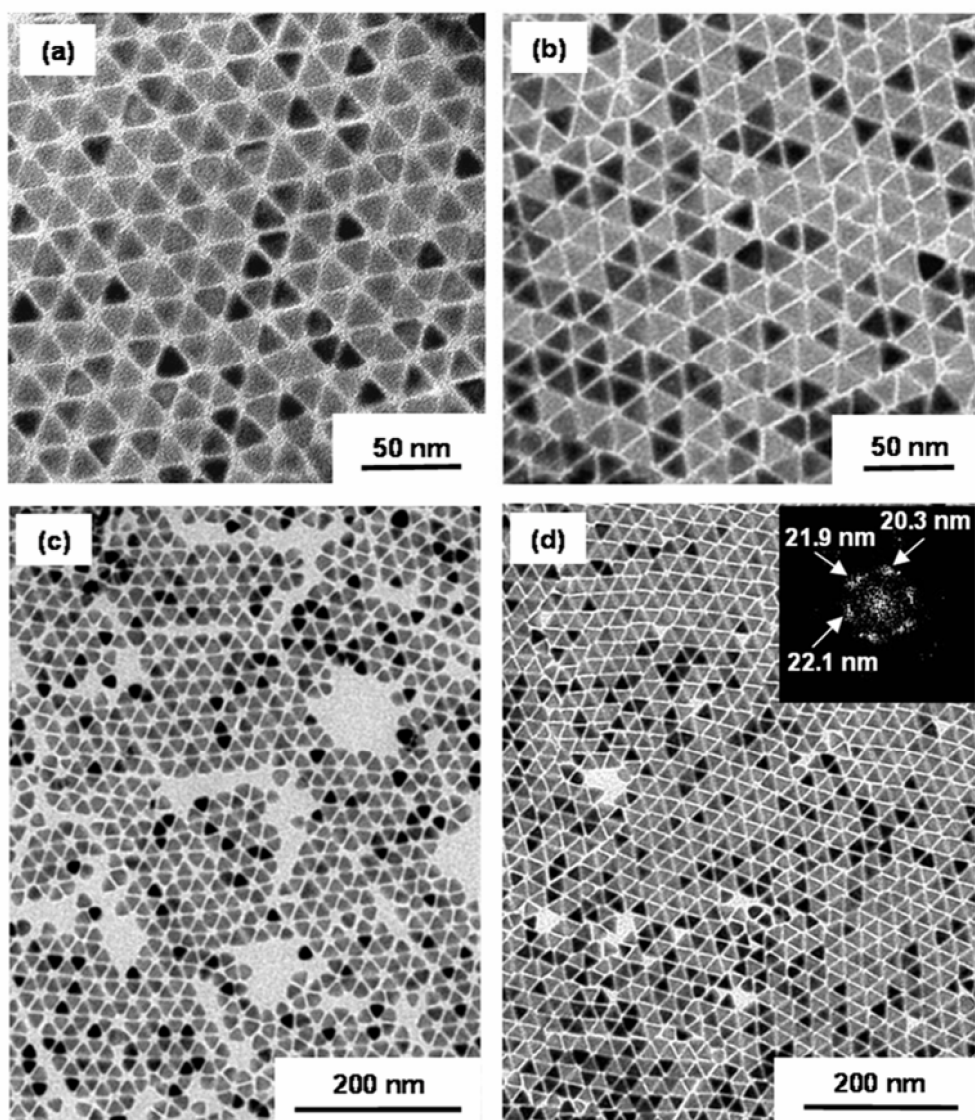
Figure 3.2. TEM images of CuInSe$_2$ nanocrystals from two different reactions: Samples (a) and (c) were made using selenourea from STREM and (b) and (d) were made with selenourea from ACROS. The nanocrystals in (a) and (c) have an average length of 16.1 nm on two sides and 16.9 nm on the other side and the nanocrystals in (b) and (d) have an average length of 16.4 nm on two sides and 17.5 nm on the other side. The inset in (d) shows a fast Fourier transform (FFT) of the region of (d), revealing the positional order of nanocrystals in the monolayer.

40
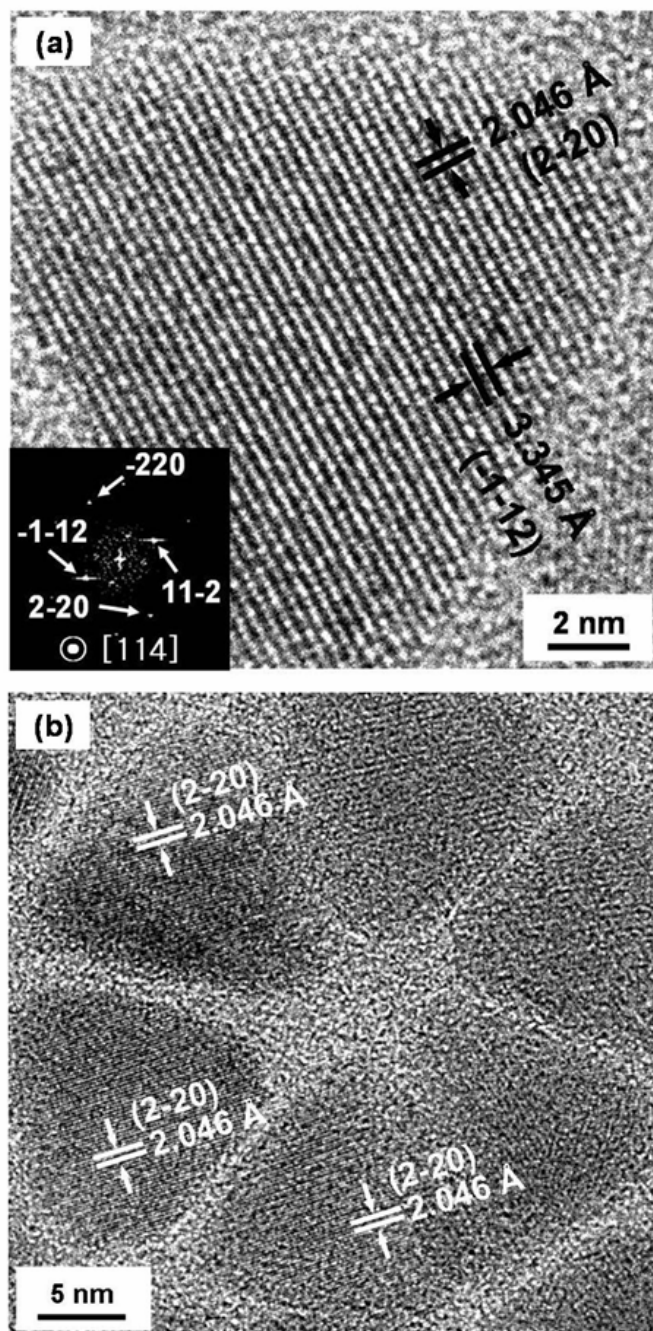
Figure 3.3. High resolution TEM images of CuInSe$_2$ nanocrystals. The inset in (a) is an FFT of the TEM image, which indexes to chalcopyrite (tetragonal) CuInSe$_2$. The measured *d*-spacings of 3.35 Å and 2.05 Å correspond to the {112} and {220} lattice planes of bulk tetragonal CuInSe$_2$ of 3.351 Å and 2.046 Å (JCPDS Card No. 40-1487).
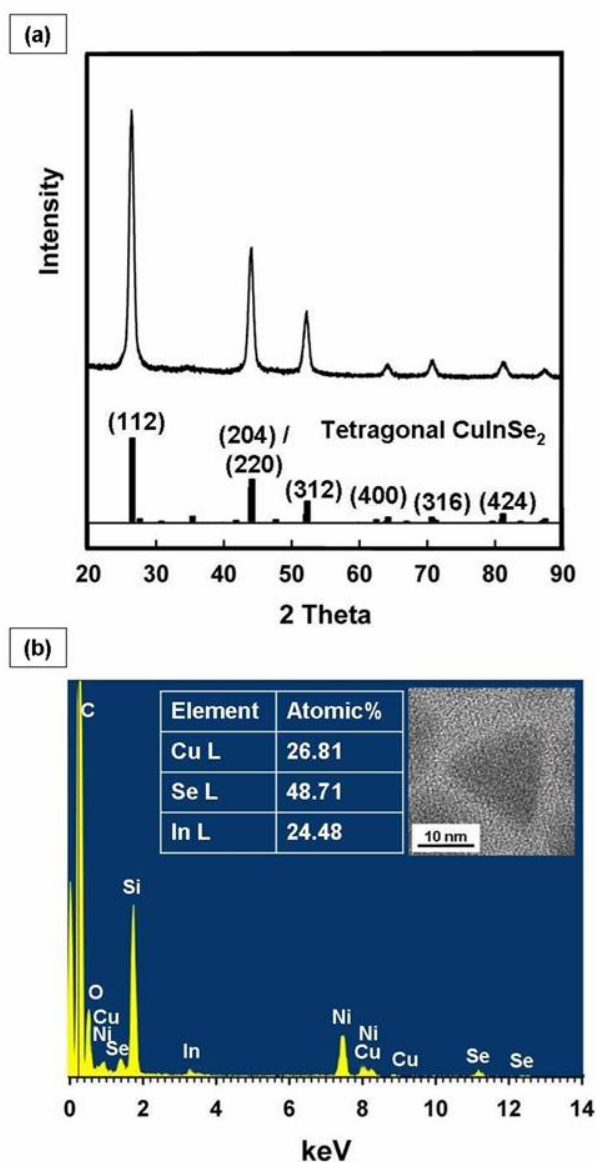
Figure 3.4. (a) XRD ($\lambda = 1.54$ Å) and (b) EDS of CuInSe$_2$ nanocrystals. The diffraction pattern indexes to chalcopyrite (tetragonal) CuInSe$_2$ (JCPDS Card No. 40-1487). The breadth of the XRD peaks is consistent with the nanoscale particle size observed by TEM. The EDS is consistent with CuInSe$_2$. The inset in (b) is an HRTEM image of the nanocrystal measured by EDS. In the EDS data, the Ni, C and Si signals are from the nickel grid, the carbon support and the background in the TEM. XRD was performed with (~200 μm thick nanocrystal films on quartz substrates using a Bruker-Nonius D8 Advance powder diffractometer with Cu Kα radiation ($\lambda = 1.54$ Å). Diffraction patterns were obtained at a scan rate of 12 deg / min in 0.01 deg increments for 12 hr, rotating the sample at 15 deg / min.
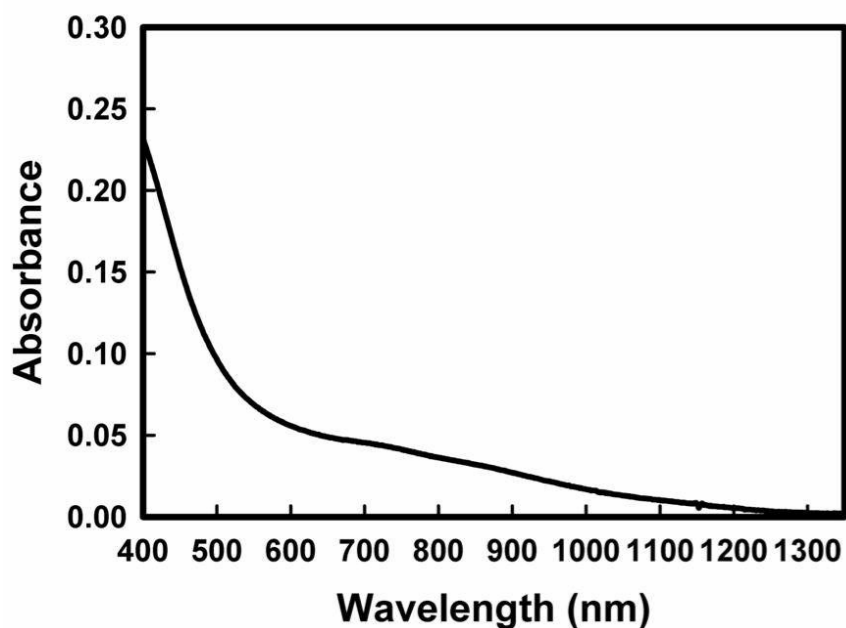
Figure 3.5.   Room temperature UV-visible absorbance spectra of an optically clear dispersion of CuInSe$_2$ nanocrystals in chloroform.   The spectra were collected on a Varian Cary 5000 Scan spectrophotometer.

3.3.2 Oleylamine etching of CuInSe$_2$ nanocrystals

The CuInSe$_2$ nanocrystals were stable for several weeks when stored dispersed in organic solvents, except when excess oleylamine was present in the solution.   The free oleylamine disintegrated the nanocrystals over the course of several days, as shown in the TEM images in Figure 3.6.   Oleylamine appears to be etching the nanocrystal surface at specific facets.   This etching by oleylamine might be similar to what Allen and Bawendi[50] observed for their Cu-In-Se nanocrystals, where their as-synthesized nanocrystals reportedly redissolved if kept in the TOP/oleylamine reaction solution for too long.
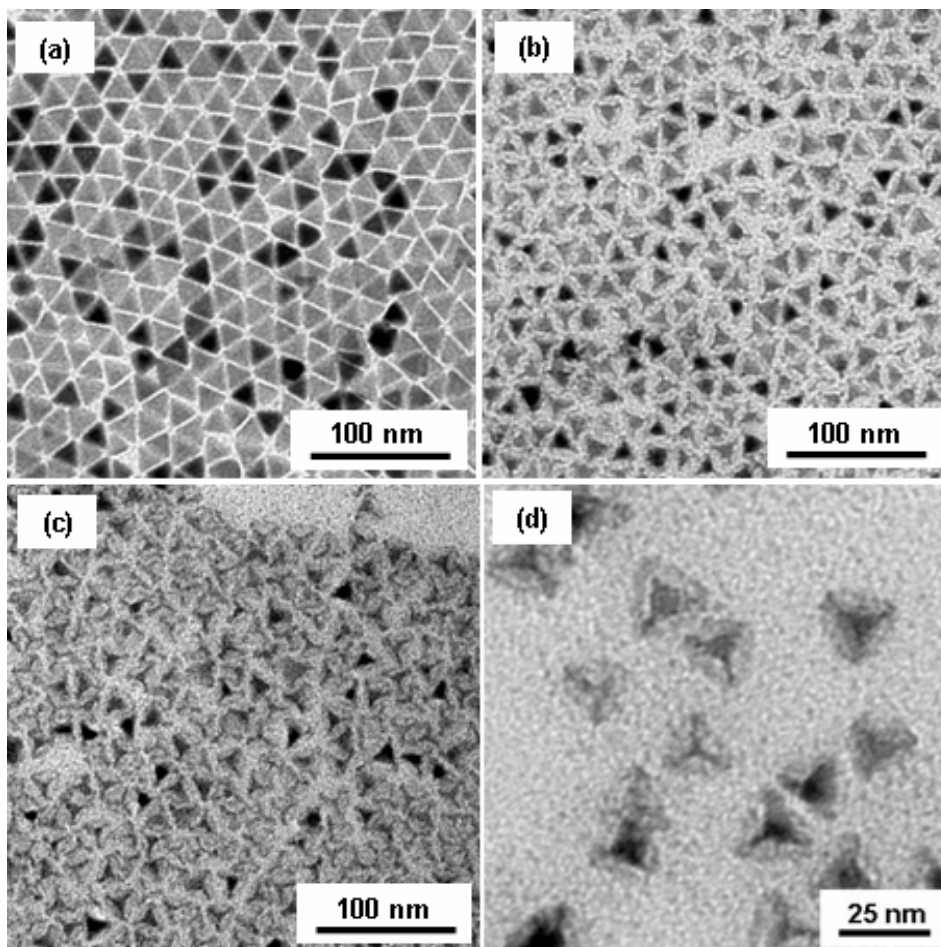
Figure 3.6. TEM images of CuInSe$_2$ nanocrystals after dispersing in chloroform at room temperature with excess oleylamine for (a) 1 day, (b) 9 days and (c,d) 13 days. The shape of the etched nanocrystals is consistent with a pyramidal shape.[97]

3.3.2.1 Effect of oleylamine etching

The etching of CuInSe$_2$ nanocrystals was confirmed by comparing nanocrystals in the presence and absence of excess oleylamine in solution. In a typical synthesis, the nanocrystals are precipitated with 30 mL of ethanol after the reaction, centrifuged, redispersed in a minimal amount of chloroform (a few mL) and reprecipitated with 30

mL of ethanol. This procedure effectively removes all of the excess oleylamine. When nanocrystals purified using this procedure were stored as dispersions, the nanocrystals were stable, as shown in the TEM images in Figure 3.7. After purification, if a drop of oleylamine (~ 2 μL) was added to the nanocrystal dispersion, the particles were observed to slowly dissolve over the course of days, as the TEM images show in Figure 3.7c. If the nanocrystals were not completely purified using the two precipitations after synthesis, then the nanocrystals were observed to etch, but at a slower rate than when oleylamine was intentionally added in excess. The nanocrystals in the TEM images in Figure 3.7a were precipitated only once with only 10 mL of ethanol (followed by centrifugation).
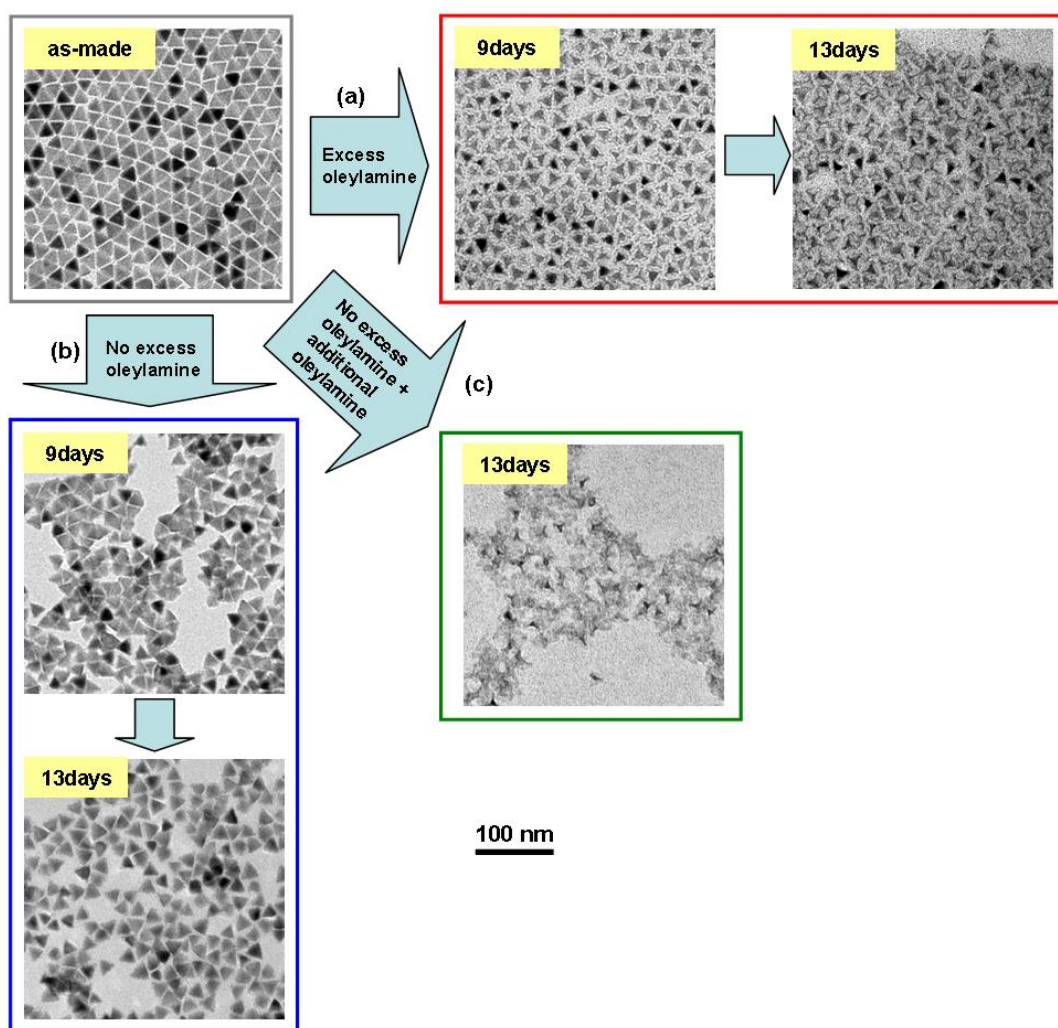
Figure 3.7. TEM images of CuInSe$_2$ nanocrystals after being stored in chloroform with varying amounts of excess oleylamine, as described above.

3.3.3 Self-Assembly into triangular lattices

The CuInSe$_2$ nanocrystals were sufficiently monodisperse to form close-packed ordered monolayers when drop-cast onto carbon TEM substrates, as shown in Figures 3.2 and 3.8. The triangular shape of the nanocrystals leads to triangular packing order in the monolayer, with each nanocrystal surrounded by only three nearest neighbors. This is a

honeycomb lattice, structurally analogous to a graphene sheet. To date, there have been only a few observations of close-packed triangle-shaped nanocrystals.[98,99] High resolution TEM images of the $CuInSe_2$ nanocrystals revealed that they shared a common crystallographic orientation with respect to the substrate. The nanocrystals in Figure 3.3 for example, are being viewed down the [114] zone axis, showing their (-1-12) and (2-20) lattice planes. These nanocrystals are all lying on the substrate on (114) facets and appear to have the same crystallographic orientation with respect to their triangular shape.
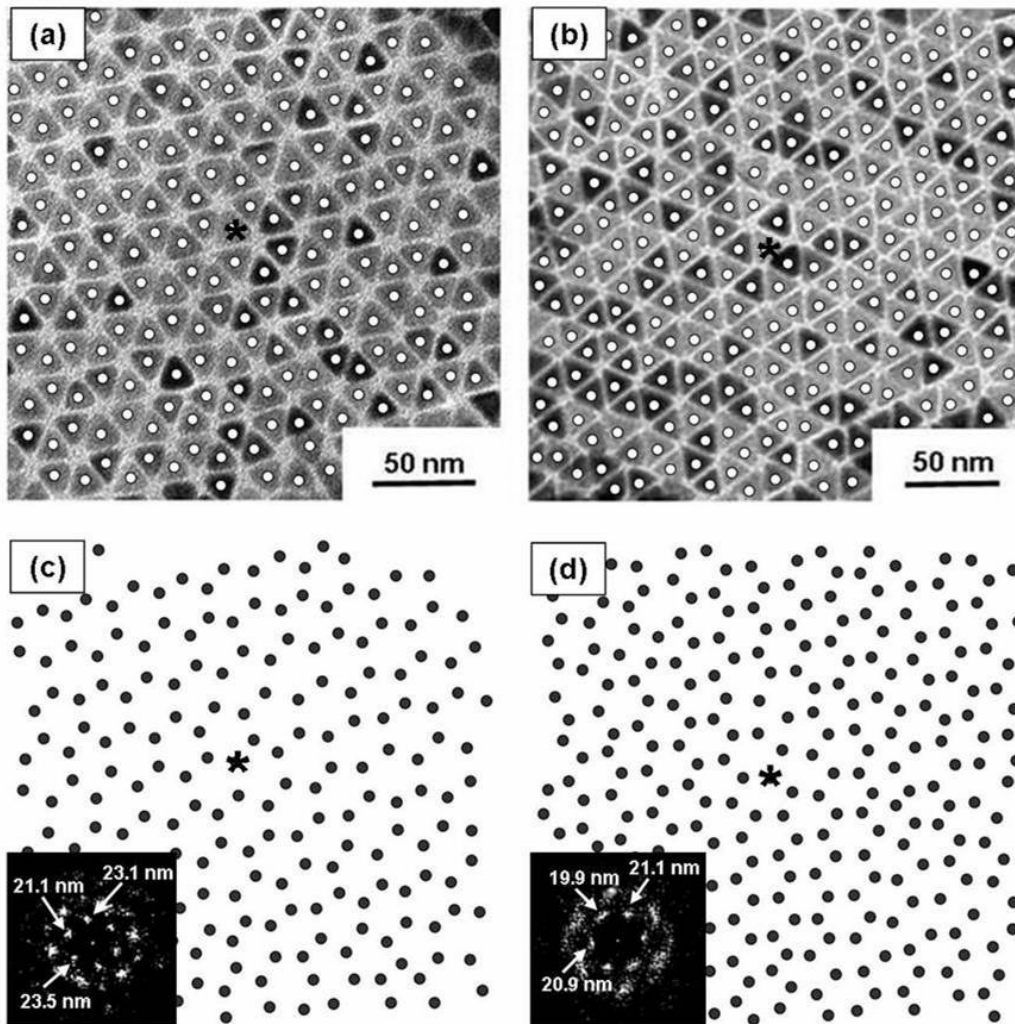
Figure 3.8. (a,b) TEM images of CuInSe$_2$ nanocrystal monolayers. White dots located at the center of the nanocrystals (a,b) help to illustrate the honeycomb structure of the monolayer in (c,d). The insets in (c) and (d) are FFTs of (a) and (b): the spot patterns reveal the positional order of particles in the monolayer of (a) and (b).

3.3.4 Three dimensional shape

It is difficult to determine the three-dimensional shape of the nanocrystals from the two-dimensional images from TEM. SEM on the other hand provides three-dimensional images of the nanocrystals. Figure 3.9 shows an SEM image of CuInSe$_2$ nanocrystals dropcast onto a Si wafer with native oxide. When drop-cast onto the silicon substrates, the nanocrystals did not deposit as an ordered monolayer and they are randomly oriented on the substrate. The nanocrystals are clearly not flat triangular platelets, but are pyramidal in shape. This information, combined with the TEM images showing the crystallographic orientation within the nanocrystals provides enough information to deduce the relationship between the CuInSe$_2$ crystal structure and the nanocrystal shape.
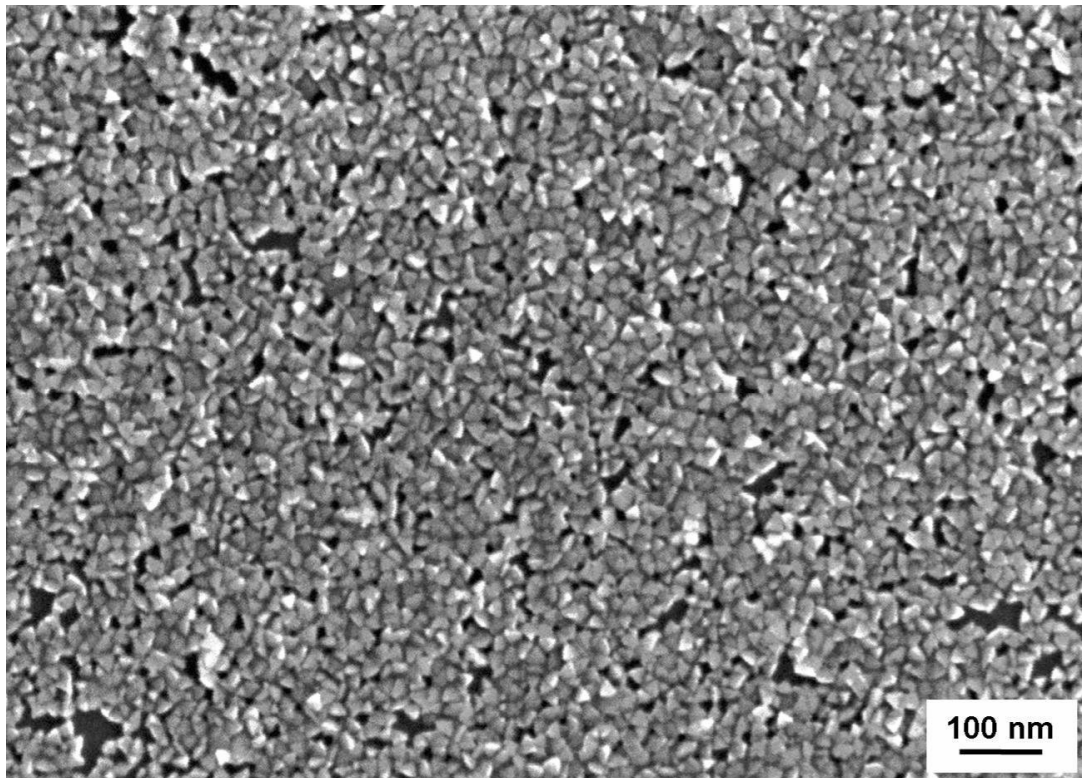
Figure 3.9.   SEM image of CuInSe$_2$ nanocrystals on a SiO$_2$-coated Si substrate.   The image was acquired with a Zeiss Supra 40 VP SEM at a working voltage of 10 kV and working distance of 8 mm.

3.3.5 Crystallographic model of CuInSe$_2$ nanocrystals

Figure 3.10a shows a crystallographic model of a trigonal pyramidal CuInSe$_2$ nanocrystal with the same crystallographic orientation as observed by TEM (as in Figure 3.3 for example).   The nanocrystal is viewed down the [114] zone axis and shows the (-1-12) and (2-20) lattice spacings.   In Figure 3.10b, the nanocrystal is portrayed slightly off the [114] zone axis to illustrate its three-dimensional pyramidal structure.   The nanocrystal lays flat on a (114) facet on the carbon TEM substrate, and its triangular shape extends from a $\left(\overline{1}\,\overline{1}\,2 \right)$ basal plane in the [11-2] direction to its triangular apex.

The other two exposed surface facets on the top of the nanocrystal are most likely the (-114) and (1-14) planes.
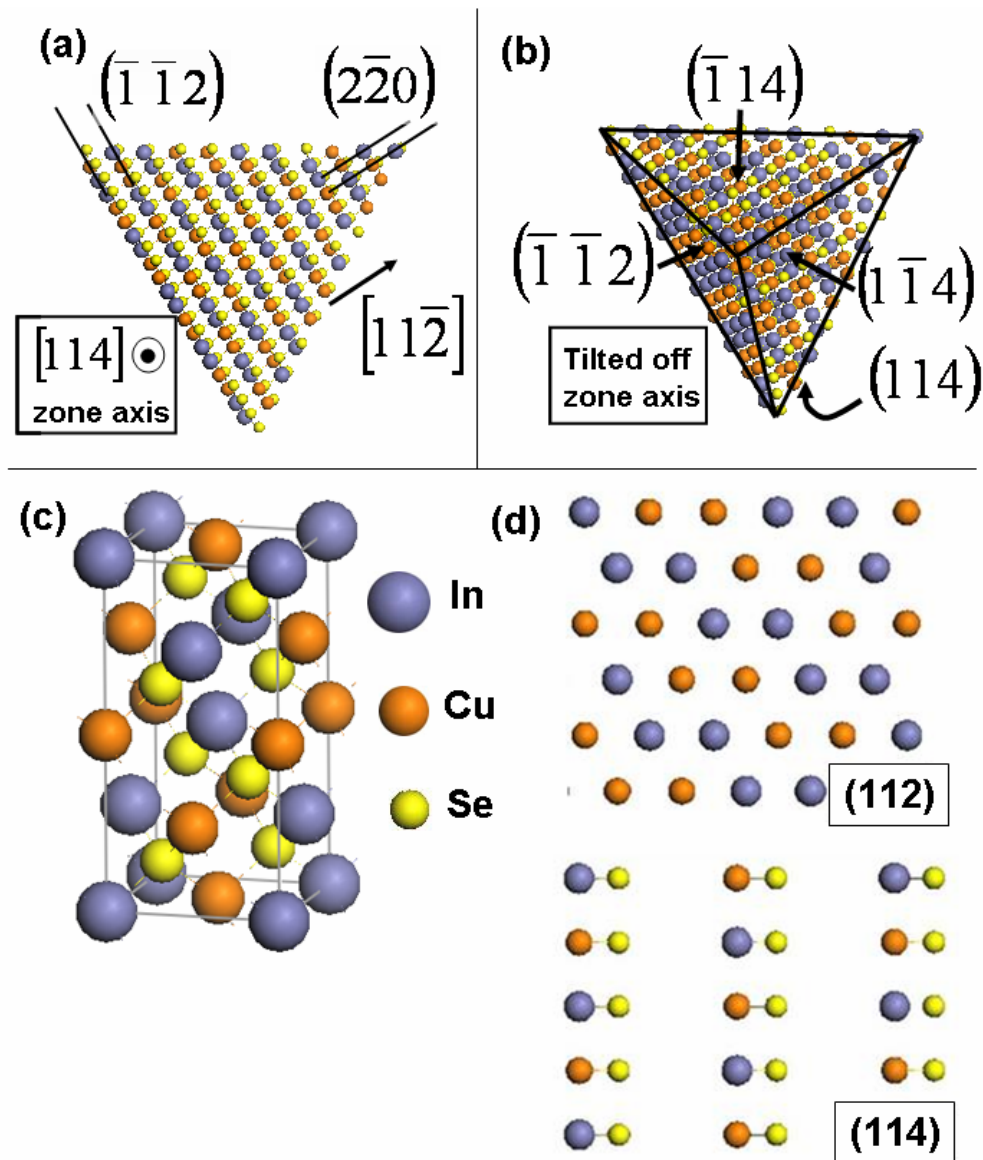
Figure 3.10. Crystallographic models of a CuInSe$_2$ nanocrystal with trigonal pyramidal shape (a) viewed down the [114] zone axis like the nanocrystals imaged by TEM image Figure 3.3 and (b) viewed slightly off the [114] zone axis to illustrate the three-dimensional shape of the nanocrystal and its (-1-12) and (-114) and (1-14) faceted surfaces; (c) the unit cell of chalcopyrite (tetragonal) CuInSe$_2$; and (d) the (112) and (114) surfaces of CuInSe$_2$.

3.3.5.1 Polarity of nanocrystal surfaces

In chalcopyrite (tetragonal) $CuInSe_2$, the (112) and (114) planes are structurally equivalent to the (111) and (112) planes, respectively, of a cubic sphalerite crystal.   The (112) surfaces are polar in the absence of surface reconstruction because they are terminated entirely by either cations or anions and thus exhibit a net positive or negative charge.   The $CuInSe_2$ (114) surfaces on the other hand are non-polar, as they are terminated by equal numbers of cations and anions, making them charge neutral.   Figure 3.10d provides an illustration of these (112) and (114) surfaces.   The pyramidal structure results from the combination of these polar and non-polar surface facets.   This is in many ways similar to nanorod and trigonal pyramid-shaped CdS, CdSe and CdTe nanocrystals[6,100-110] and disk-shaped Cu_2S[111] and CuS[112] nanocrystals, in which surface facets of different polarity exhibit significantly different growth rates, thus leading to non-spherical nanocrystals.   In the $CuInSe_2$ trigonal pyramidal nanocrystals, either a cation or anion-terminated (-1-12) surface must be relatively stable, while the opposing (11-2) surface is relatively reactive, leading to fast growth in the [11-2] direction.   The three other sidewall facets are terminated by non-polar {114} surfaces.   The other non-polar surfaces of chalcopyrite $CuInSe_2$—the (110) surfaces—are not observed.   This is consistent with what is known about $CuInSe_2$, as Jaffe *et al.*[113] and Zhang *et al.*[114] have shown that the (112)/(-1-1-2) surfaces are more stable than the (110) surfaces due to their particular ability to reconstruct via defect formation

3.4 CONCLUSIONS

In summary, monodisperse $CuInSe_2$ nanocrystals were synthesized.   They exhibit a trigonal pyramid hape as a result of their chalcopyrite crystal structure and the corresponding surface facet polarity.   Oleylamine is an effective capping ligand to

control CuInSe$_2$ nanocrystal growth, but when present in excess in solution it can also etch the nanocrystal surfaces.   When dropcast onto carbon substrates, the nanocrystals deposit on their (114) surfaces and form close-packed monolayers with triangular order. When dropcast on silicon substrates (with native oxide), the nanocrystals do not exhibit the same facet-selective deposition and do not form ordered monolayers.

3.5 REFERENCES

(1)   Repins, I.; Contreras, M. A.; Egaas, B.; DeHart, C.; Scharf, J.; Perkins, C. L.; To, B.; Noufi, R. *Prog Photovoltaics* **2008**, *16*, 235-239.

(2)   Wu, Y.; Wadia, C.; Ma, W. L.; Sadtler, B.; Alivisatos, A. P. *Nano Lett* **2008**, *8*, 2551-2555.

(3)   Yang, Y. H.; Chen, Y. T. *J Phys Chem B* **2006**, *110*, 17370-17374.

(4)   Li, B.; Xie, Y.; Huang, J. X.; Qian, Y. T. *Adv Mater* **1999**, *11*, 1456-1459.

(5)   Jiang, Y.; Wu, Y.; Mo, X.; Yu, W. C.; Xie, Y.; Qian, Y. T. *Inorg Chem* **2000**, *39*, 2964.

(6)   Gou, X. L.; Cheng, F. Y.; Shi, Y. H.; Zhang, L.; Peng, S. J.; Chen, J.; Shen, P. W. *J Am Chem Soc* **2006**, *128*, 7222-7229.

(7)   Castro, S. L.; Bailey, S. G.; Raffaelle, R. P.; Banger, K. K.; Hepp, A. F. *Chem Mater* **2003**, *15*, 3142-3147.

(8)   Malik, M. A.; O'Brien, P.; Revaprasadu, N. *Adv Mater* **1999**, *11*, 1441-1444.

(9)   Zhong, H. Z.; Li, Y. C.; Ye, M. F.; Zhu, Z. Z.; Zhou, Y.; Yang, C. H.; Li, Y. F. *Nanotechnology* **2007**, *18*.

(10)   Allen, P. M.; Bawendi, M. G. *J Am Chem Soc* **2008**, *130*, 9240.

(11)   Murray, C. B.; Norris, D. J.; Bawendi, M. G. *J Am Chem Soc* **1993**, *115*, 8706-8715.

(12)   Hines, M. A.; Guyot-Sionnest, P. *J Phys Chem B* **1998**, *102*, 3655-3657.

(13)   Metraux, G. S.; Cao, Y. C.; Jin, R. C.; Mirkin, C. A. *Nano Lett* **2003**, *3*, 519-522.

(14)   Zhang, Y. W.; Sun, X.; Si, R.; You, L. P.; Yan, C. H. *J Am Chem Soc* **2005**, *127*, 3260-3261.

(15)   Shevchenko, E. V.; Talapin, D. V.; Kotov, N. A.; O'Brien, S.; Murray, C. B. *Nature* **2006**, *439*, 55-59.

(16)   Manna, L.; Scher, E. C.; Alivisatos, A. P. *J Am Chem Soc* **2000**, *122*, 12700-12706.

(17)   Manna, L.; Wang, L. W.; Cingolani, R.; Alivisatos, A. P. *J Phys Chem B* **2005**, *109*, 6183-6192.

(18)   Barnard, A. S.; Xu, H. F. *J Phys Chem C* **2007**, *111*, 18112-18117.

(19)   Asokan, S.; Krueger, K. M.; Colvin, V. L.; Wong, M. S. *Small* **2007**, *3*, 1164-1169.

(20)   Sapra, S.; Poppe, J.; Eychmuller, A. *Small* **2007**, *3*, 1886-1888.

(21)   Sadowski, T.; Ramprasad, R. *Phys Rev B* **2007**, *76*.

(22)   Wang, W.; Banerjee, S.; Jia, S. G.; Steigerwald, M. L.; Herman, I. P. *Chem Mater* **2007**, *19*, 2573-2580.

(23)   Xu, X. X.; Liu, F.; Yu, K. H.; Huang, W.; Peng, B.; Wei, W. *Chemphyschem* **2007**, *8*, 703-711.

(24)   Lou, W. J.; Chen, M.; Wang, X. B.; Liu, W. M. *J Phys Chem C* **2007**, *111*, 9658-9663.

(25)   Pinna, N.; Weiss, K.; Urban, J.; Pileni, M. P. *Adv Mater* **2001**, *13*, 261.

(26)   Rempel, J. Y.; Trout, B. L.; Bawendi, M. G.; Jensen, K. F. *J Phys Chem B* **2006**, *110*, 18007-18016.

(27)   Shieh, F.; Saunders, A. E.; Korgel, B. A. *J Phys Chem B* **2005**, *109*, 8538-8542.

(28)   Sigman, M. B.; Ghezelbash, A.; Hanrath, T.; Saunders, A. E.; Lee, F.; Korgel, B. A. *J Am Chem Soc* **2003**, *125*, 16050-16057.

(29)   Ghezelbash, A.; Korgel, B. A. *Langmuir* **2005**, *21*, 9451-9456.

(30)   Jaffe, J. E.; Zunger, A. *Phys Rev B* **2001**, *64*.

(31)   Zhang, S. B.; Wei, S. H. *Phys Rev B* **2002**, *65*.

Chapter 4: Effect of Excess CuCl on the Formation of Monodisperse Trigonal Pyramidal CuInSe$_2$ Nanocrystals

4.1 INTRODUCTION

The importance of monodisperse nanocrystals has been significantly increased due to the dependence of electrical, magnetic, and optical properties on their size, shape, and composition.[56]   The mechanism for the formation of monodisperse nanocrystals has been studied based upon burst nucleation and separated growth.[60-64]   It is so far revealed that diverse variables (such as reaction condition, reactivity, or kind of reactant) could influence the monodispersity of nanocrystals provided by colloidal synthetic methods. However, the complexity and subtlety of the effect of those variables on monodispersity still requires profound study on each individual case.

In this chapter, it is shown that the amount of excess CuCl precursor affected the monodispersity of trigonal pyramidal CuInSe$_2$ nanocrystals, which I previously reported (as shown in Chapter 3).[65]   Although the synthetic process previously showed the importance of precise synthetic ways, reaction temperature, and choice of oleylamine for the formation of monodisperse CuInSe$_2$ nanocrystals, more study was needed on the factors to influence the monodispersity such as precursor concentration related to reaction kinetics.

4.2 EXPERIMENTAL SECTION

Copper(I) chloride (CuCl, Aldrich, anhydrous, beads, ≥99.99+ %), indium(III) chloride (InCl$_3$, Aldrich, 99.999 %), selenourea (ACROS, 99.9+ %), and oleylamine (Aldrich, 70%) were purchased and used as received.

4.2.1 Nanocrystal preparation

In a typical synthesis, a mixture of CuCl, InCl$_3$, and oleylamine is vigorously stirred and degassed in the reaction flask for 30 minutes at 60 ℃ on the Schlenk line in the glovebox.   The amount of InCl$_3$ and oleylamine are fixed as 0.11 g (0.5 mmol of In) and 10 mL, respectively.   On the other hand, the amount of CuCl varies adding an excess amount from 0 % to 75 % in each reaction.   The mixture is then heated to 130 ℃ under nitrogen for 10 minutes.   During heating, the solution turns from blue to yellow, indicating the formation of oleylamine complexes with Cu and In.   Meanwhile, the selenium reactant solution is prepared by dissolving 0.123 g of selenourea (1.0 mmol) in 1 mL of oleylamine at 200 ℃ under nitrogen on a Schlenk line.   The In/Cu/oleylamine reactant solution is cooled to 100 ℃ and the selenium reactant solution is added by syringe.   Immediately after injection of the Se reactant, the reaction mixture is heated to 240 ℃ at a rate of 15 ℃/min.   After 1 hour, the nanocrystals are removed from the heating mantle and allowed to cool to room temperature.   20 mL of ethanol is then added to precipitate the nanocrystals, followed by centrifugation at 8000 rpm for 1 min. The supernatant is discarded.   The nanocrystals redisperse in a variety of non-polar organic solvents, including chloroform, hexane, and toluene.   Prior to characterization, dispersions are typically centrifuged again at 4000 rpm for 3 min to remove inadequately capped nanocrystals, followed by an additional washing process with centrifugation at 7000 rpm for 3 min.   A typical reaction yields ~100 mg of CuInSe$_2$ nanocrystals.

4.2.2 Characterization methods

TEM images were acquired on either a JEOL 2010F microscope equipped with a field emission gun operated at 200 kV or an FEI Tecnai microscope operated at 80 kV. TEM samples were prepared by drop-casting from chloroform dispersions onto carbon-

coated Ni TEM grids (200-mesh, Electron Microscopy Sciences). The JEOL 2010F has an Oxford X-ray energy dispersive spectroscopy (EDS) detector, which was used for elemental analysis.

XRD patterns were obtained from nanocrystal films that were approximately 200 μm thick on quartz substrates. A Bruker-Nonius D8 Advance powder diffractometer with Cu Kα radiation ($\lambda = 1.54$ Å) was used with a scan rate of 6 deg/min in 0.01 deg increments, collecting for 12 hr with that sample rotating at 15 deg/min.

Room temperature UV-visible absorbance spectra were collected on a Varian Cary 5000 Scan spectrophotometer with samples dispersed in chloroform in quartz cuvettes.

4.3 RESULTS

4.3.1 Formation of Nanocrystals with different amounts of Excess CuCl

Figure 4.1 shows TEM images of the nanocrystals synthesized adding different amounts of excess CuCl into a reaction solution including stoichiometric CuCl, $InCl_3$ and selenourea (Cu:In:Se=1:1:2) in oleylamine. It is revealed that the nanocrystals appreared to be more monodisperse as the amount of excess CuCl increased until 45 % excess CuCl where highly monodisperse trigonal pyramidal $CuInSe_2$ nanocrystals formed. On the other hand, beyond 45 % excess CuCl point, the nanocrystals lost a trigonal shape (Figure 4.1f) and finally became polydisperse (Figure 4.1g).
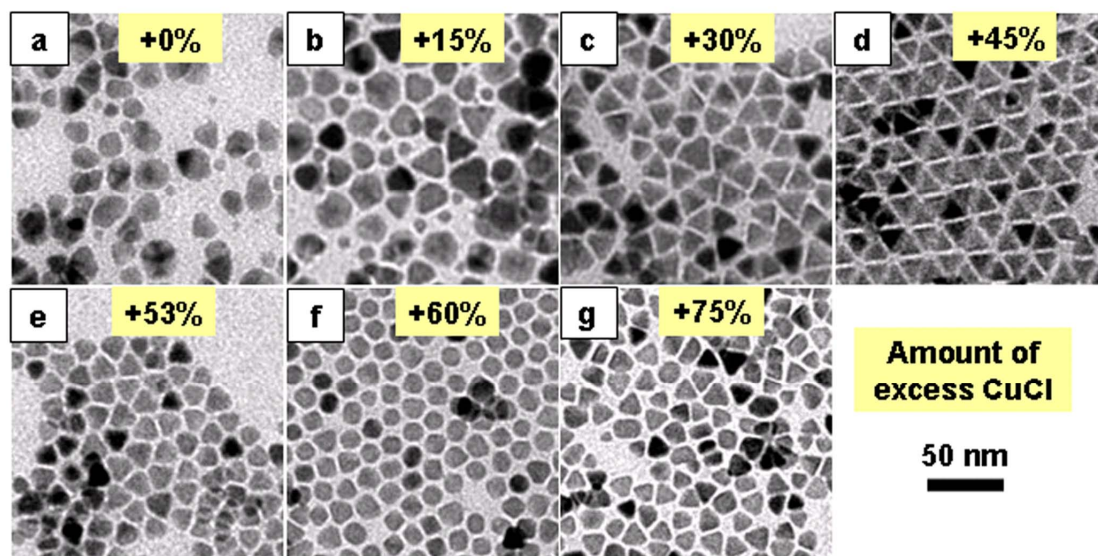
Figure 4.1. TEM images of nanocrystals synthesized using different amounts of excess CuCl: (a) 0 %, (b) 15 %, (c) 30 %, (d) 45 %, (e) 53 %, (f) 60 %, and (g) 75 %. All particle dimensions are measured and shown in Figure 4.3. It is shown that the highest monodispersity occurred with 45 % excess CuCl into a reaction solution.

4.3.1.1 Quantitative analysis

Plots of average particle size, relative standard deviation of size, and percentage of shapes versus amount of excess CuCl were shown in Figures 4.2a, 4.2b, and 4.2c, respectively. Size histograms are shown in Figure 4.3. While Figure 4.2a shows that average particle sizes are in a similar range (13-17 nm), relative standard deviations show a sudden drop and increase in Figure 4.2b, which implies that the amount of excess CuCl plays an important role on the formation of monodisperse $CuInSe_2$ nanocrystals. Moreover, it is shown that particle shapes vary depending on the amount of excess CuCl in the reaction solution. Figure 4.2c showed that a percentage of triangular (in fact, this is a trigonal pyramidal shape in three dimension[65]) particles most drastically changed as the excess CuCl amount increased. The triangular shape had the highest percentage

(95 %) at the excess CuCl amount of 45 % as well as the case of highest monodispersity (relative standard deviation of size=9.9 %). This corresponds that the CuInSe$_2$ nanocrystals made with 45 % excess CuCl showed very high monodispersity in both size and shape in the TEM image (Figure 4.1d). Note that the tendency of increasing monodispersity (in both size and shape) was broken after 45 % excess CuCl.
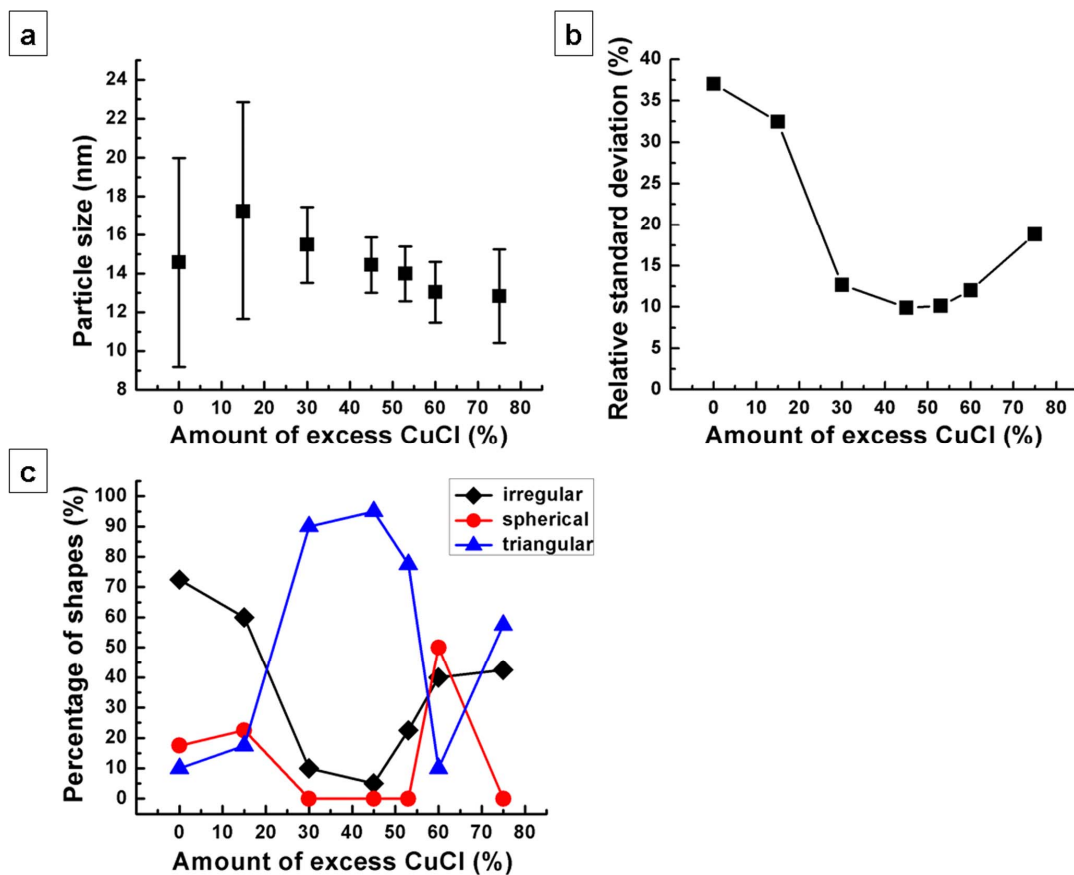
Figure 4.2. Plots of (a) average particle size, (b) relative standard deviation of size, and (c) percentage of shapes versus amount of excess CuCl. (a) revealed that all particle sizes are within a similar range, but (b) and (c) showed a sudden change in both size and shape at the 45 % excess CuCl amount, where the most monodisperse triangular CuInSe$_2$ nanocrystals formed.
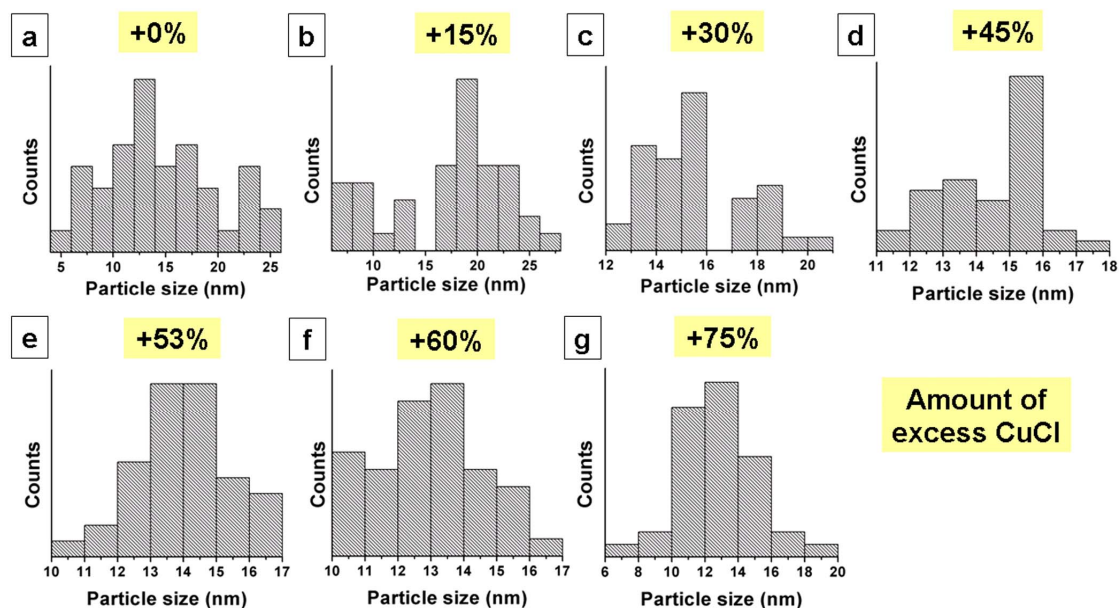
Figure 4.3. Size histograms of nanocrystals synthesized using different amounts of excess CuCl, which were constructred from TEM images in Figure 4.1.

4.3.2 Crystal structure and composition of nanocrystals

The XRD patterns of the nanocrystals synthesized with different amounts of excess CuCl were shown in Figure 4.4a.   This revealed that while the nanocrystals had a $CuInSe_2$ chalcopyrite structure until the highest monodispersity point (45 % CuCl excess), the crystal structure slightly changed beyond that point.   In order to elucidate the slight change in XRD peaks, the I, II, and III patterns indicated in Figure 4.4a were enlarged in Figure 4.4b.   Here, it is shown that the patterns of 60 % and 75 % excess CuCl had an explicit peak shift to a longer 2 theta, which corresponds to Cu_2Se (cubic) structure.   It is presumed that the monodispersity break after 45 % excess CuCl is attributed to the crystal structure change due to using a relatively large amount of CuCl precursor.   The patterns of 60 % excess CuCl showed a little trace of $CuInSe_2$ crystal structure in addition to Cu_2Se structure, possibly indicating a mixture of $CuInSe_2$ (small

portion) and Cu$_2$Se (large portion) nanocrystals. Figure 4.4c showed atomic compositional ratios of corresponding nanocrystals using EDS. They revealed a transform of Cu:In:Se ratio from 1:1:2 ratio to 2:1:0 from 0 % to 75 % of excess CuCl. The EDS from 60 % confirmed that those nanocrystals contained a mixture of Cu$_2$Se and CuInSe$_2$ as previously implied in its XRD peaks in Figure 4.4b.

c		Atomic%				
Element		+0%	+45%	+53%	+60%	+75%
Cu L		24.58	23.36	28.88	49.45	60.69
Se L		51.10	52.79	50.40	44.57	39.31
In L		24.32	23.85	20.73	5.99	0.00
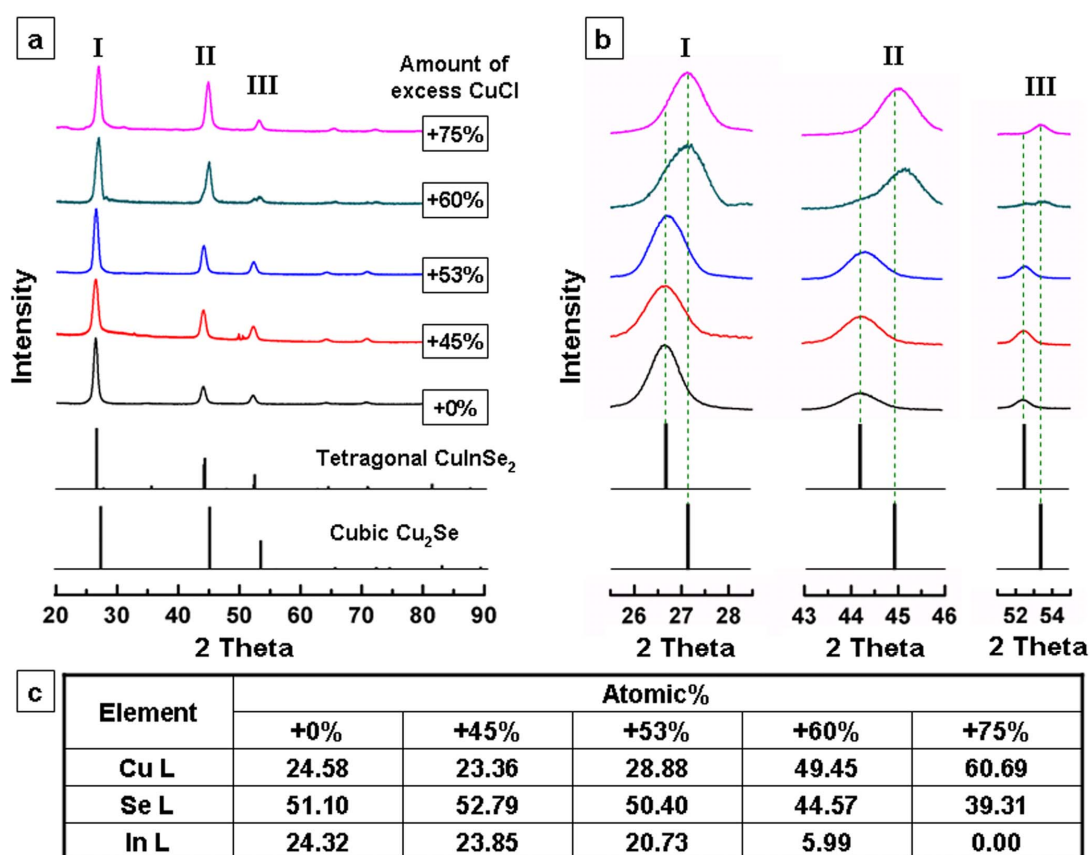
Figure 4.4. (a,b) XRD and (c) EDS of the nanocrystals synthesized using different amounts of excess CuCl.   The stick patterns for chalcopyrite (tetragonal) CuInSe$_2$ (JCPDS No. 040-1487) and cubic Cu$_2$Se (JCPDS No. 01-088-2043) are provided for references in (a).   (b) shows enlarged peaks of I, II, and III shown in (a), indicating an explicit peak shift of +60 % and +75 % to a longer 2 theta (Cu$_2$Se position).   EDS also shows a significant change from +60 %, finally having approximately 2:1:0 ratio of Cu:In:Se at +75 %.

60

4.3.3 Optical properties of nanocrystals

UV-vis absorbance spectra from the same sets of nanocrystals were shown in Figure 4.5. This also confirmed that the nanocrystals made by excess CuCl of +0 % and +45 % showed the expected band gap energy of ~1 eV typical of bulk $CuInSe_2$. However, the absorbance from +60 % and +75 % ones had extra broad peaks at longer wavelength (1000-1200 nm). This could be explained as a typical absorbance peak of Cu_2Se.[115,116]
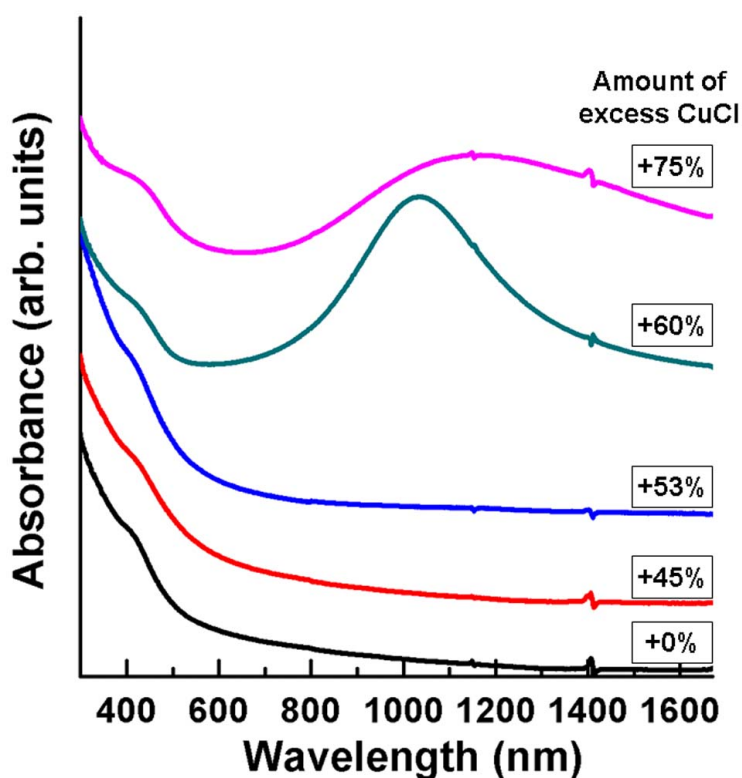
Figure 4.5. Room temperature UV-vis absorbance spectra of an optically clear dispersion (in chloroform) of the nanocrystals synthesized using different amounts of excess CuCl. The absorption edges until ~45 % correspond to an optical gap of 1 eV (bulk $CuInSe_2$), however, the broad absorbance peaks of +60 % and +75 % indicate the existence of Cu_2Se.

4.4 DISCUSSION

4.4.1 Effect of excess CuCl on nucleation-growth process

Based upon kinetics of colloidal nanocrystal formation,[60,64] the effect of excess CuCl precursor on the formation of monodisperse $CuInSe_2$ nanocrystals was deduced. The colloidal nanocrystal formation is mostly explained as a nucleation-growth mechanism, comprising three reaction steps: (1) monomer formation (P→M), (2) nucleation ($xM→C_x$), and (3) growth ($C_x+yM↔C_{x+y}$) where P: precursor, M: monomer, C: crystal. In order to obtain monodisperse nanocrystals, the nucleation reaction (2) has to be retarded so that no preliminary nucleation occurs before a burst nucleation. After a sudden nucleation where a large amount of nuclei form in a very short time, only growth dominates without more nucleation process owing to a small amount of reactants left (the reaction step (3)), leading a formation of monodisperse nanocrystals.

The separation of metal and selenium precursors and the use of oleylamine were our efforts to satisfy the first mechanism (retardation of nucleation). Note that oleylamine effectively coordinates with each precursor,[65] forming stable monomers in the reaction step (1), and metal salt precursors and selenium source (selenourea) are initially isolated and converted to a complex form with oleylamine in each reaction container in order to well stabilize the monomers prior to fast reaction.

In spite of this endeavor, the reaction step (2) is insufficiently retarded in case of a stoichiometric reaction of $CuInSe_2$ nanocrystals. (See the polydisperse particles in Figure 4.1a) It is presumably because indium precursor is relatively reactive since indium poorly forms a coordination complex rather than copper. However, if excess amount of CuCl is added, the total portion of coordinated (stable) complex increases due to an immediate formation of CuCl-oleylamine complex. Thus, the reaction step (2) could be efficiently delayed by adding excess amount of CuCl. This is followed by high

accumulated monomer concentration and subsequent burst nucleation, resulting in the formation of monodisperse $CuInSe_2$ nanocrystals (Figure 4.1d). However, if the amount of excess CuCl was over a certain point (which turned out to be 45 %), the monodispersity was also broken (Figures 4.1f and 4.1g) possibly because too overloaded CuCl made a different reaction process making Cu-rich crystal structure such as Cu_2Se as shown XRD and EDS data of Figure 4.4.

4.4.1.1 Effect of excess CuCl on nanocrystal shape

Not only size but also shape can be influenced by using an excess CuCl. The trigonal pyramidal $CuInSe_2$ nanocrystals were revealed to contain three nonpolar {114} facets and one polar {112} facet by our group.[65] Based upon that crystallographic model, one can notice that the number of cations (Cu or In) is larger than that of anions (Se) on the nanocrystal surface. Therefore, more amount of CuCl (or $InCl_3$) might be needed for the formation of the trigonal pyramidal $CuInSe_2$ nanocrystals intrinsically having cation-rich composition. This statement is plausible since the $CuInSe_2$ nanocrystals have a small size (~10 nm) where the portion of atoms on the surface is significant. As a proof, it was shown in Figure 4.2c that the number of triangular particles was conspicuously lower when less amount of excess CuCl was used. For the case of large amount of excess CuCl, the portion of triangular particles rather decreased due to the same reason of the formation of different materials as explained above.

4.5 CONCLUSIONS

The effect of excess CuCl on the formation of monodisperse trigonal pyramidal $CuInSe_2$ nanocrystals was investigated. It was revealed that 45 % excess CuCl lead the most monodisperse trigonal pyramidal $CuInSe_2$ nanocrystals in their size and shape. In addition, the monodispersity trend was suddenly changed around 45 % of excess CuCl,

accompanying with the transform of crystals structure from $CuInSe_2$ to Cu_2Se. The formation mechanism of monodisperse trigonal pyramidal $CuInSe_2$ nanocrystals was suggested with regard to excess amount of CuCl precursor, based on the nucleation-growth model of colloidal nanocrystal formation.

4. 6 REFERENCES

(1)   El-Sayed, M. A. Accounts of Chemical Research **2004**, 37, 326-333.

(2)   Kwon, S. G.; Hyeon, T. Accounts of Chemical Research **2008**, 41, 1696-1709.

(3)   Peng, X. G.; Wickham, J.; Alivisatos, A. P. Journal of the American Chemical Society **1998**, 120, 5343-5344.

(4)   Talapin, D. V.; Rogach, A. L.; Haase, M.; Weller, H. Journal of Physical Chemistry B **2001**, 105, 12278-12285.

(5)   Casula, M. F.; Jun, Y. W.; Zaziski, D. J.; Chan, E. M.; Corrias, A.; Alivisatos, A. P. Journal of the American Chemical Society **2006**, 128, 1675-1682.

(6)   Kwon, S. G.; Piao, Y.; Park, J.; Angappane, S.; Jo, Y.; Hwang, N. M.; Park, J. G.; Hyeon, T. Journal of the American Chemical Society **2007**, 129, 12571-12584.

(7)   Koo, B.; Patel, R. N.; Korgel, B. A. Journal of the American Chemical Society **2009**, 131, 3134.

(8)   Gurin, V. S.; Alexeenko, A. A.; Yumashev, K. V.; Prokoshin, R.; Zolotovskaya, S. A.; Zhavnerko, G. A. Materials Science & Engineering C-Biomimetic and Supramolecular Systems **2003**, 23, 1063-1067.

(9)   Jagminas, A.; Juskenas, R.; Gailiute, I.; Statkute, G.; Tomasiunas, R. Journal of Crystal Growth **2006**, 294, 343-348.

Chapter 5: Wurtzite-Chalcopyrite Polytypism in CuInS$_2$ Nanodisks[†]

5.1 INTRODUCTION

The wurtzite CuInS$_2$ nanocrystals were synthesized via colloidal synthetic procedures by several research groups.[66,77-81]   However, there is still a need to obtain refined nanocrystals with improved size and shape control.

In this chapter, it is reported that monodisperse and wurtzite CuInS$_2$ nanodisks were synthesized.   Wurtzite crystal structure of CuInS$_2$ nanodisks were revealed by X-ray diffraction (XRD) and high resolution transmission electron microscopy (TEM) of the CuInS$_2$ nanodisks revealed a significant amount of polytypism with most of the nanodisks having domains of chalcopyrite CuInS$_2$ interfaced with wurtzite CuInS$_2$ across $(002)_w/(112)_{ch}$ stacking faults.   This is the first example of wurtzite-chalcopyrite polytypism in a I-III-VI$_2$ compound and is a consequence of the high surface area to volume ratio of the nanodisks and the colloidal synthesis.

5.2 EXPERIMENTAL SECTION

Copper(I) chloride (CuCl, Aldrich, 99.995+ %), indium(III) chloride (InCl$_3$, Aldrich, 99.999 %), Copper(II) acetylacetonate (Cu(acac)$_2$, Aldrich, 99.99+%), thiourea (Fluka, ≥99.0 %), and oleylamine (Fluka) were purchased and used as received.

5.2.1 Nanocrystal synthesis

A mixture of 0.05 g of CuCl (0.5 mmol of Cu), 0.11 g of InCl$_3$ (0.5 mmol of In), 0.076 g of thiourea (1.0 mmol of S), and 10 mL of oleylamine is vigorously stirred (this solution has a dark brown color) and degassed in the reaction flask for 30 minutes at 60ºC by pulling vacuum on a Schlenk line.   The flask is then filled with nitrogen and heated

---

[†] The contents of this chapter appear in *Chemistry of Materials* 21(9), 1962-1966 (**2009**)

to 240ºC at a rate of 15ºC/min.   During the heating process, smoke begins to evolve at about 200ºC and the color turns a darker color, indicating nanocrystal nucleation and growth.   After allowing the reaction to proceed for one hour, the reaction flask is removed from the heating mantle and allowed to cool to room temperature.   30 mL of ethanol is then added to precipitate the nanocrystals, followed by centrifugation at 7000 rpm for 3 minutes.   The supernatant is discarded.   The nanocrystals redisperse in a variety of non-polar organic solvents, including chloroform, hexane, and toluene.   Prior to characterization, dispersions are centrifuged again at 6000 rpm for 1 min to remove inadequately capped nanocrystals.   A typical reaction yields approximately 200 mg of $CuInS_2$ nanocrystals.

5.2.2 Characterization methods

Nanocrystals were imaged by scanning and transmission electron microscopy (SEM and TEM).   TEM images were acquired on a JEOL 2010F microscope equipped with a field emission gun operated at 200 kV.   TEM samples were prepared by drop-casting from chloroform dispersions onto carbon-coated Ni TEM grids (200-mesh, Electron Microscopy Sciences). The JEOL 2010F has an Oxford X-ray energy dispersive spectroscopy (EDS) detector, which was used for elemental analysis.   SEM images were acquired with a Zeiss Supra 40 VP SEM at a working voltage of 10-15 kV and working distance of 6 mm.

XRD patterns were obtained from nanocrystal films that were approximately 200 μm thick on quartz substrates.   A Bruker-Nonius D8 Advance powder diffractometer with Cu Kα radiation ($\lambda = 1.54$ Å) was used with a scan rate of 6 deg/min in 0.01 deg increments, collecting for 12 hr with that sample rotating at 15 deg/min.

Room temperature UV-visible absorbance spectra were collected on a Varian Cary 5000 Scan spectrophotometer with samples dispersed in chloroform in quartz cuvettes.

.

5.3 RESULTS AND DISCUSSION

5.3.1 Synthesis of CuInS$_2$ Nanodisks

Figures 5.1 and 5.2 show TEM and SEM images of the CuInS$_2$ nanodisks synthesized by heating CuCl, InCl$_3$ and thiourea in oleylamine at 240°C. The nanodisks are monodisperse with average diameter and thickness of 13.4 nm and 5.7 nm. The standard deviation about the mean diameter is ±12.0%. The disk shape of the particles is easily observed, as they either deposit flat with their faces on the substrate or on their sides, in some cases stacking face-to-face into columns extended parallel to the substrate (See for example Figures 5.1c, 5.2c and 5.2d). EDS (Figure 5.3b) confirmed that the nanodisks are composed of CuInS$_2$, with Cu:In:S atomic ratios very near to 1:1:2. The optical absorption edge in the UV-vis absorbance spectra also corresponds to the expected band gap energy of 1.53 eV typical of bulk CuInS$_2$ (Figure 5.4).
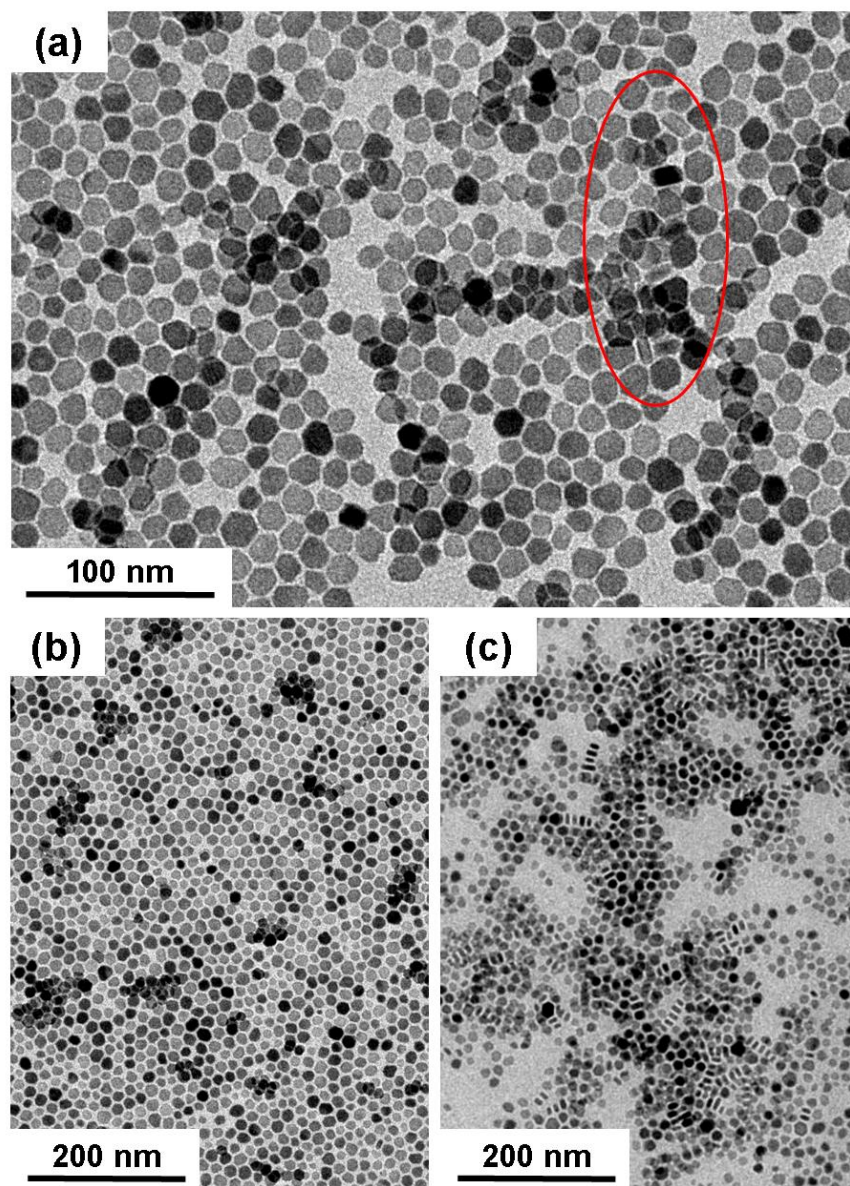
Figure 5.1. TEM images of CuInS$_2$ nanodisks. The dimensions are 13.4 ± 1.6 nm (diameter) and 5.7 ± 0.6 nm (thickness). The red oval in (a) highlights a region of nanodisks oriented on their sides and the image in (c) shows many nanodisks on their sides.
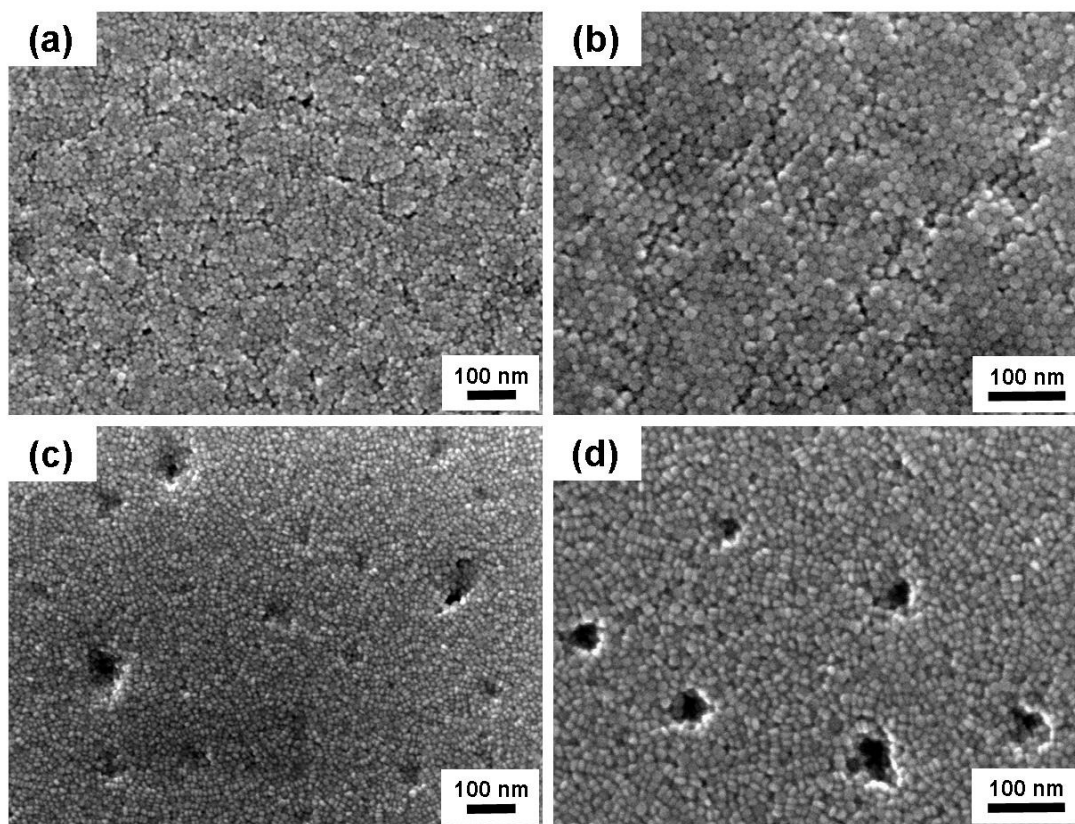
Figure 5.2. SEM images of CuInS$_2$ nanodisks on silicon substrates coated with either (a,b) native oxide or (c,d) silicon nitride (Si$_3$N$_4$). In these two cases, the orientation of the nanodisks is different on the substrates, resting either on their faces as in (a) and (b) or on their sides as in (c) and (d).

69
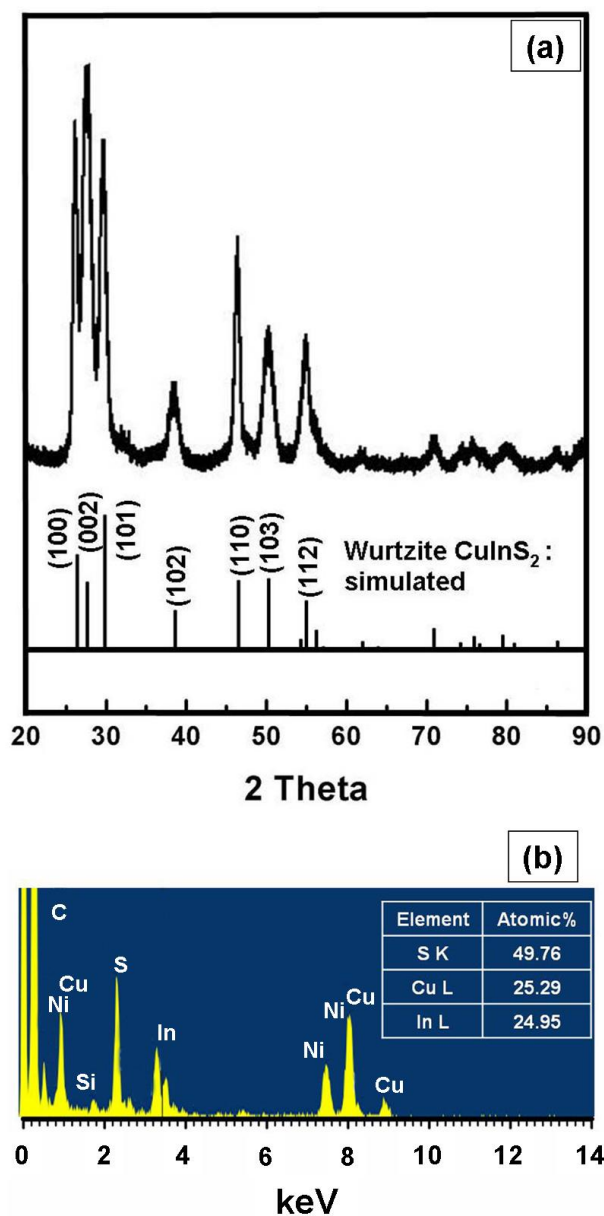
Figure 5.3. XRD and (b) EDS of CuInS$_2$ nanodisks. The stick patterns for wurtzite CuInS$_2$ shown in (a) were calculated with the CaRIne Crystallography 3.1 program using the following lattice parameters: space grou, P63mc (No. 186) and unit cell dimensions $a = b = 3.897(3)$ Å, $c = 6.441(0)$ Å.[66] The Ni, C and Si signals in the EDS data are from the nickel grid, the carbon support and the background in the TEM.
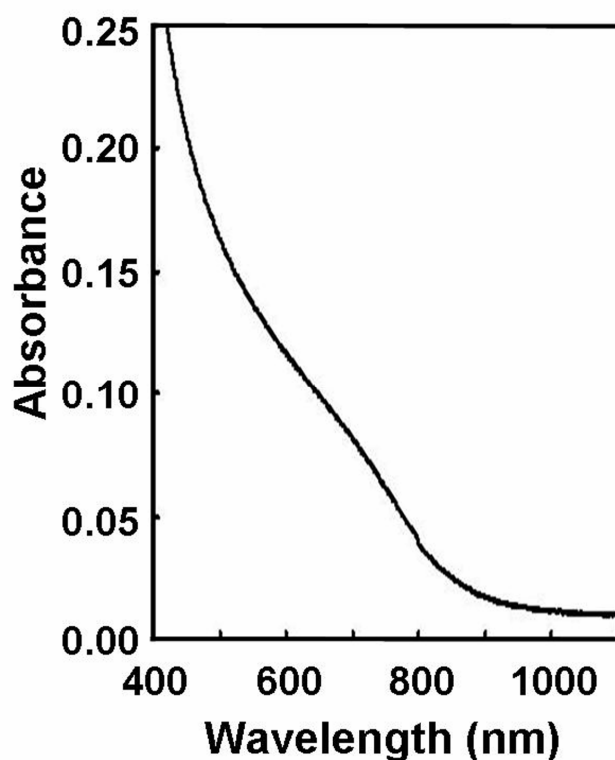
Figure 5.4. Room temperature UV-vis absorbance spectra of an optically clear dispersion of $CuInS_2$ nanocrystals in chloroform. The absorption edge corresponds to an optical gap of 1.53 eV, which is consistent with bulk $CuInS_2$.

5.3.2 Wurtzite CuInS$_2$ Nanodisks

The XRD patterns (Figure 5.3a) from the nanodisks, however, were characteristic of a hexagonal wurtzite structure as opposed to the expected tetragonal chalcopyrite structure. Although the wurtzite phase was unexpected, Pan, *et al.*[66] has also recently observed the formation of wurtzite $CuInS_2$ nanocrystals. The XRD pattern calculated using the lattice parameters reported by Pan, *et al.*[66] (space group: P63mc (No. 186) and unit cell dimensions $a = b = 3.897(3)$ Å, $c = 6.441(0)$ Å) gave a good match to the experimental diffraction pattern, as shown in Figure 5.3a.

5.3.2.1 XRD comparison

Figure 5.5 shows a comparison of the experimental XRD pattern with the simulated wurtzite $CuInS_2$ pattern and other possible crystal phases, such as chalcopyrite $CuInS_2$ and impurities, like hexagonal Cu_2S, and hexagonal CuS. The experimental diffraction patterns matches wurtzite $CuInS_2$ phase, with the exception of a small peak at $2\Theta=32^o$ that corresponds to the chalcopyrite (211) diffraction peak, further verifying the existence of the chalcopyrite phase in the nanodisks.

Wurtzite CuInS$_2$: simulated

(100)
(002)
(101)
(102)
(110)
(103)
(112)

JCPDS 27-0159
Tetragonal
(Chalcopyrite)
CuInS$_2$

JCPDS 26-1116
hexagonal Cu$_2$S

JCPDS 6-0464
hexagonal CuS

Only wurtzite
Only chalcopyrite
Both wurtzite &
chalcopyrite

2 Theta
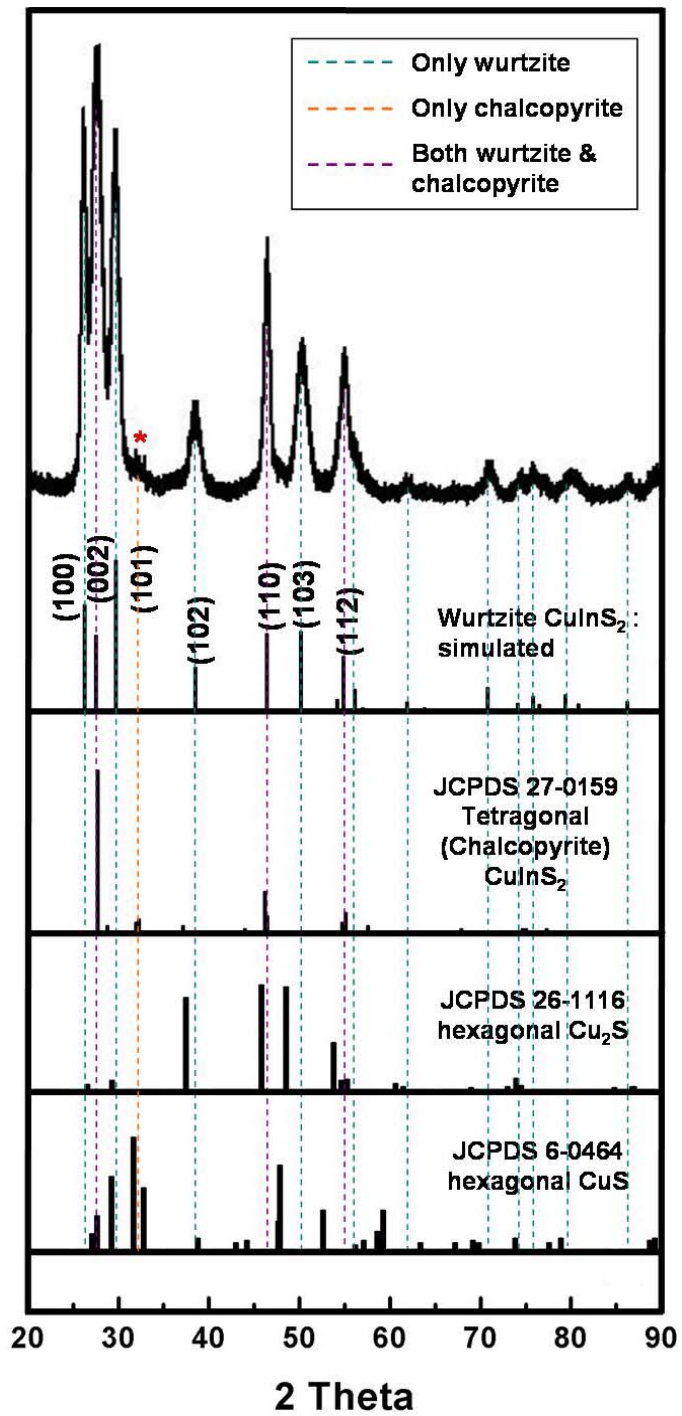
Figure 5.5.   Comparison of an experimental XRD pattern with several other possible crystal phases.   The colored and dashed lines provide references for the wurtzite and chalcopyrite $CuInS_2$ phases.   The red asterisk indicates a peak corresponding to the $(211)_{ch}$ diffraction peak.

5.3.3 HRTEM analysis

The nanodisks were further studied by high resolution TEM.   Figure 5.6 shows TEM images of the nanodisks with two different orientations on the substrate.   The FFT of the image in Figure 5.6a corresponds to a crystal with a hexagonal structure with the nanodisk being viewed down the [001] zone axis (i.e., the c-axis of the wurtzite $CuInS_2$ crystal structure).   The top and bottom faces of the disk are bounded by {002} planes, as illustrated in Figure 5.6c.   Similar crystallographic orientations have been observed for CuS and Cu_2S nanodisks with hexagonal crystal structure.[111,112]
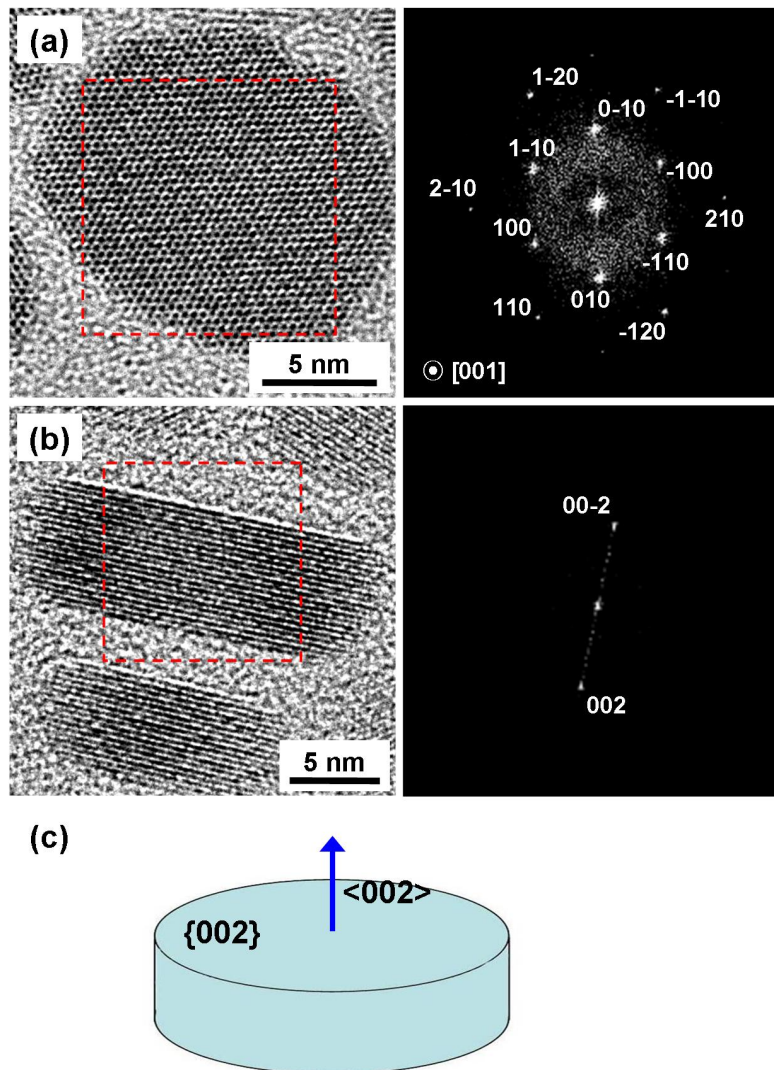
Figure 5.6. TEM images of CuInS$_2$ nanodisks with two different orientations on the substrate: (a) lying flat and (b) standing on edge. The FFTs are consistent with wurtzite CuInS$_2$: the (100) spots do not appear in the chalcopyrite structure. (c) Illustration of the crystallographic orientation of the nanodisks based on TEM images like those in (a) and (b).

5.3.4 Polytypism of CuInS$_2$ nanodisks

Extensive TEM revealed that a significant amount of chalcopyrite CuInS$_2$ was also present in the nanodisks. We noticed that stacking faults were present in many nanodisks imaged on their sides. A careful structural analysis of the TEM images

showed that part of the crystal was actually in the chalcopyrite phase. This was surprising because XRD quite clearly showed that the nanodisks were composed of wurtzite $CuInS_2$. But a more careful look at the XRD peak intensities also revealed that wurtzite-chalcopyrite polytypism was present in the sample. The diffraction peak positions matched wurtzite $CuInS_2$, but the intensities of the peaks corresponding to chalcopyrite—i.e., the wurtzite (002), (110), and (112) peaks—were slightly higher than expected. Most nanodisks turned out to have crystalline wurtzite domains interfaced with chalcopyrite domains across $(002)_w/(112)_{ch}$ stacking faults, like the nanodisk in Figure 5.7.
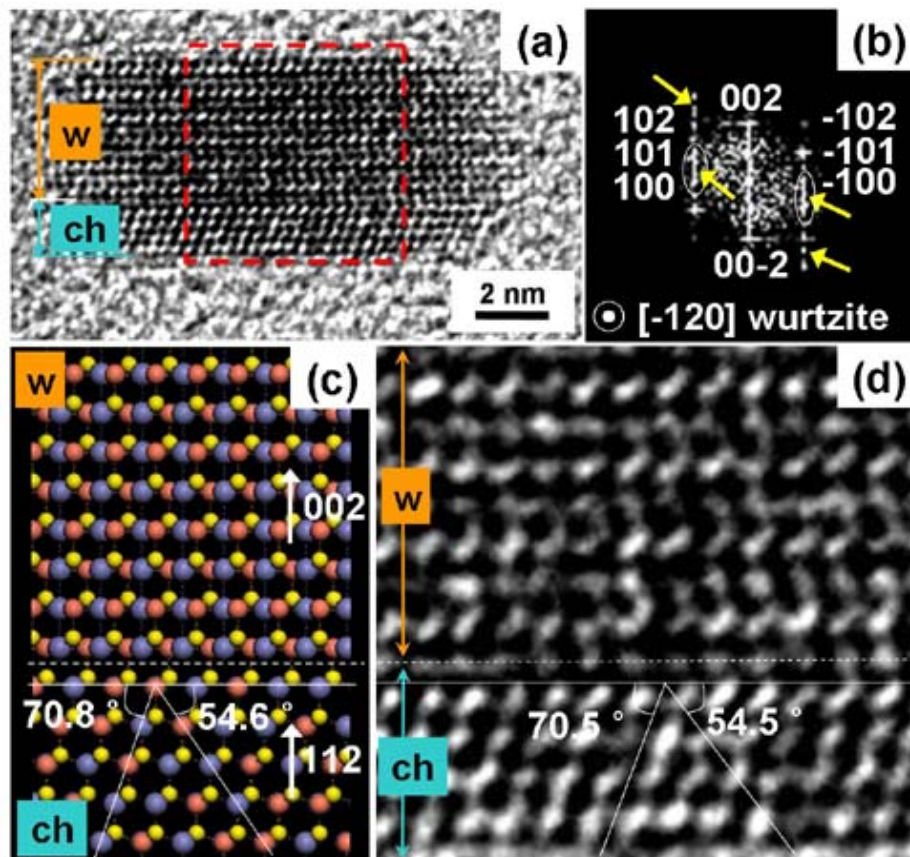
Figure 5.7. (a) HRTEM image of the CuInS$_2$ nanocrystal with [-120] zone axis and (b) FFT of the red square area in (a). The FFT shows multiple diffraction spots (indicated by yellow arrows) from chalcopyrite structure at the lower part. (c) A crystal model showing the {-120} wurtzite plane and its equivalent {0-24} chalcopyrite plane. The crystal models were generated using Materials Studio and the angles between lattice planes were calculated by CaRIne Crystallography 3.1 program. (d) Magnified image of the region bordered by the red square in (a) with the same scale as the simulated crystal in (c). ("w" and "ch" indicate wurtzite and chalcopyrite, respectively.)

The crystal phase of the nanodisks is therefore most accurately described as *polytypic*, as both wurtzite and chalcopyrite crystal domains coexist within each nanodisk. For example, the FFT in Figure 5.7b generated from the crystalline region outlined by the red square in (a) has more spots (indicated by the yellow arrows) than expected for a wurtzite crystal imaged down the [-120] zone axis. These additional spots arise from the change in crystal structure to chalcopyrite across the stacking fault.

5.3.4.1 FFT analysis

Figure 5.8 shows additional TEM images of polytypic nanodisks and Figure 5.9 shows another example of a nanodisk imaged on its side and the FFTs generated from different positions of the crystal showing the wurtzite-chalcopyrite polytypism.
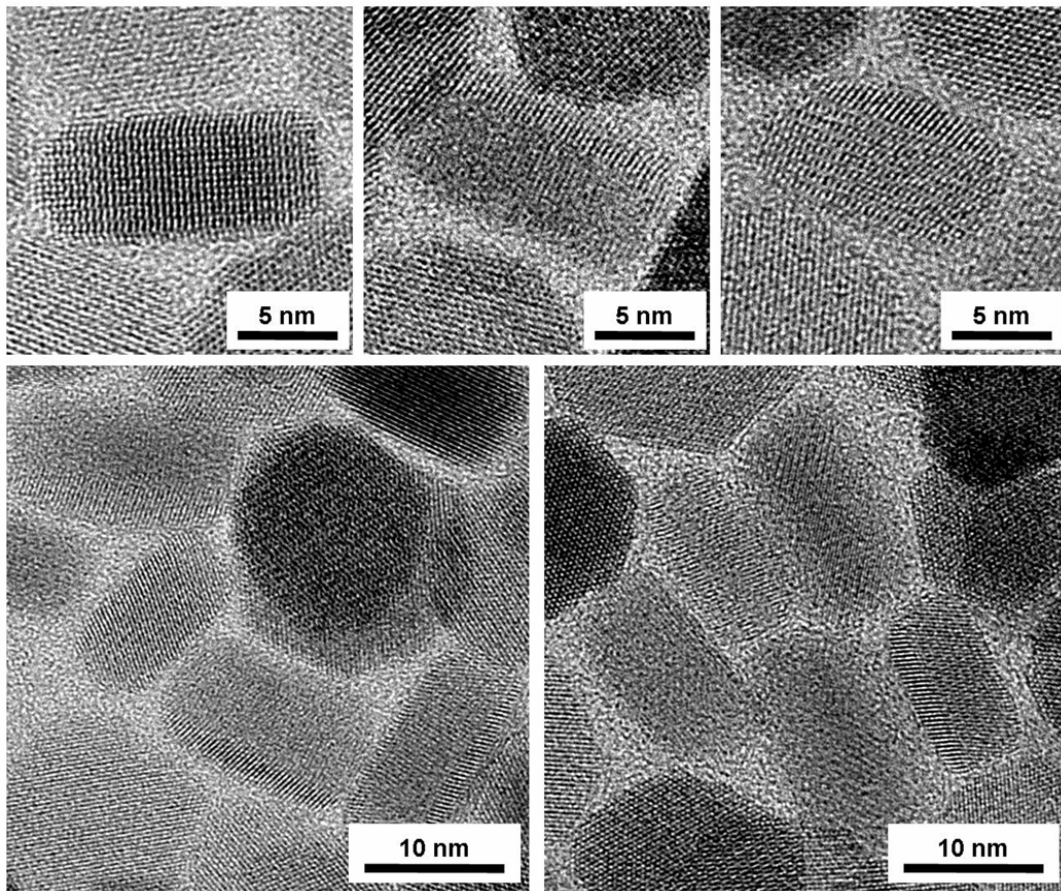
Figure 5.8. HRTEM images of CuInS$_2$ nanodisks oriented on their sides, exhibiting wurtzite-chalcopyrite polytypism.
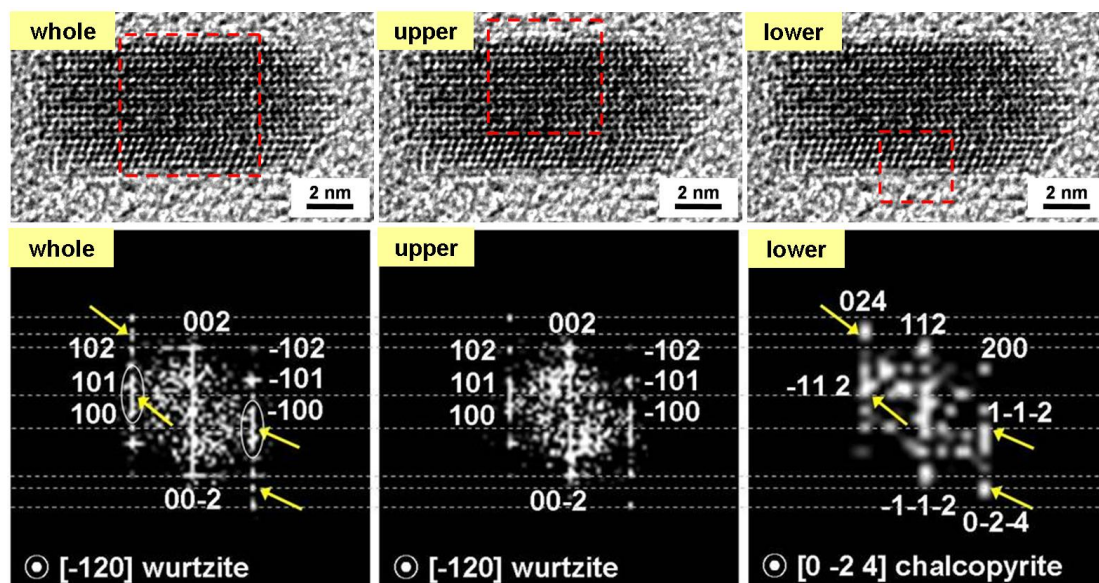
Figure 5.9. FFTs generated from a TEM image of a CuInS$_2$ nanodisk at the different regions of the crystal outlined in red. The additional spots in the FFT arise from the crystalline chalcopyrite domain ([0-24] zone axis), indicated by yellow arrows under the wurtzite domain.

It should be appreciated that the wurtzite-chalcopyrite polytypism can only be observed in TEM images of nanodisks with particular orientations on the substrate. For example, nanodisks oriented on their faces (like the one imaged in Figure 5.6b) and imaged down the [001]$_w$ zone axis appear to be single crystals as the (002)$_w$/(112)$_{ch}$ stacking faults within the interior of the nanodisk are not visible when viewed in this crystallographic direction. The stacking faults are only observable when the crystal is imaged down the [-120]$_w$ zone axis.

5.3.5 Different Cu precursor effect

CuInS$_2$ nanodisks with wurtzite crystal structure were also obtained when the synthesis was carried out using Cu(acac)$_2$ in place of CuCl as the Cu source. (Copper(II) acetylacetonate (Cu(acac)$_2$, 99.99+%) was obtained from Aldrich and used as

received.) Figures 5.10 and 5.11 show TEM images of the CuInS$_2$ nanodisks. The high resolution TEM images (Figure 5.11) show that the nanodisks exhibit wurtzite-chalcopyrite polytypism, but that the nanodisks exhibit a larger presence of chalcopyrite CuInS$_2$ than the nanodisks made using CuCl. The relative intensities of the diffraction peaks in the XRD data (Figure 5.12) are consistent with the conclusions drawn from the TEM images. Specifically, the intensities of peaks characteristic of the chalcopyrite phase—which are those that overlap with the wurtzite (002), (110), and (112) peaks—are more intense in the sample made with Cu(acac)$_2$ than nanodisks made with CuCl.
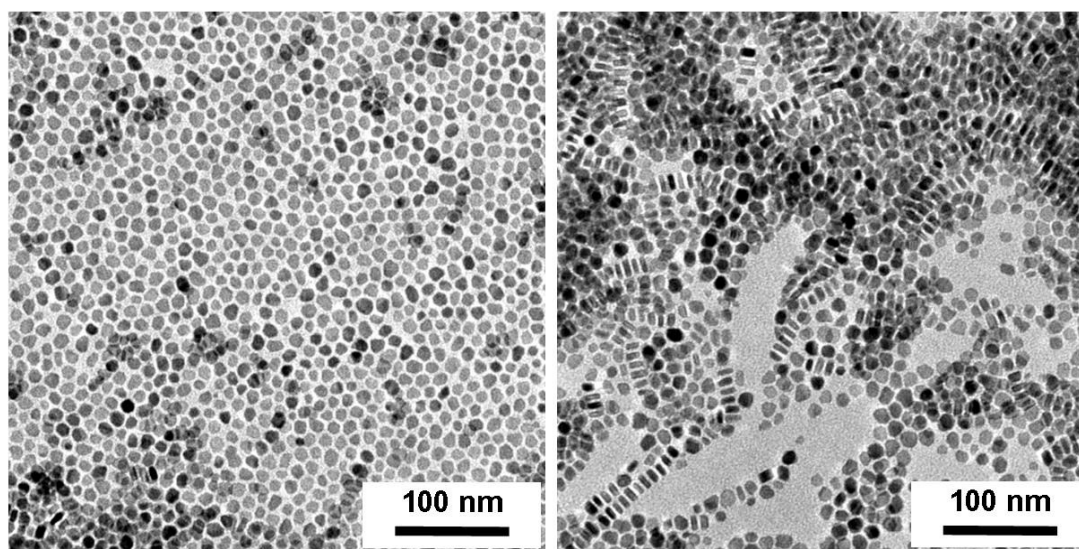
Figure 5.10.   TEM images of wurtzite CuInS$_2$ nanodisks synthesized using Cu(acac)$_2$ in place of CuCl.   The average diameter is 11.5 nm.
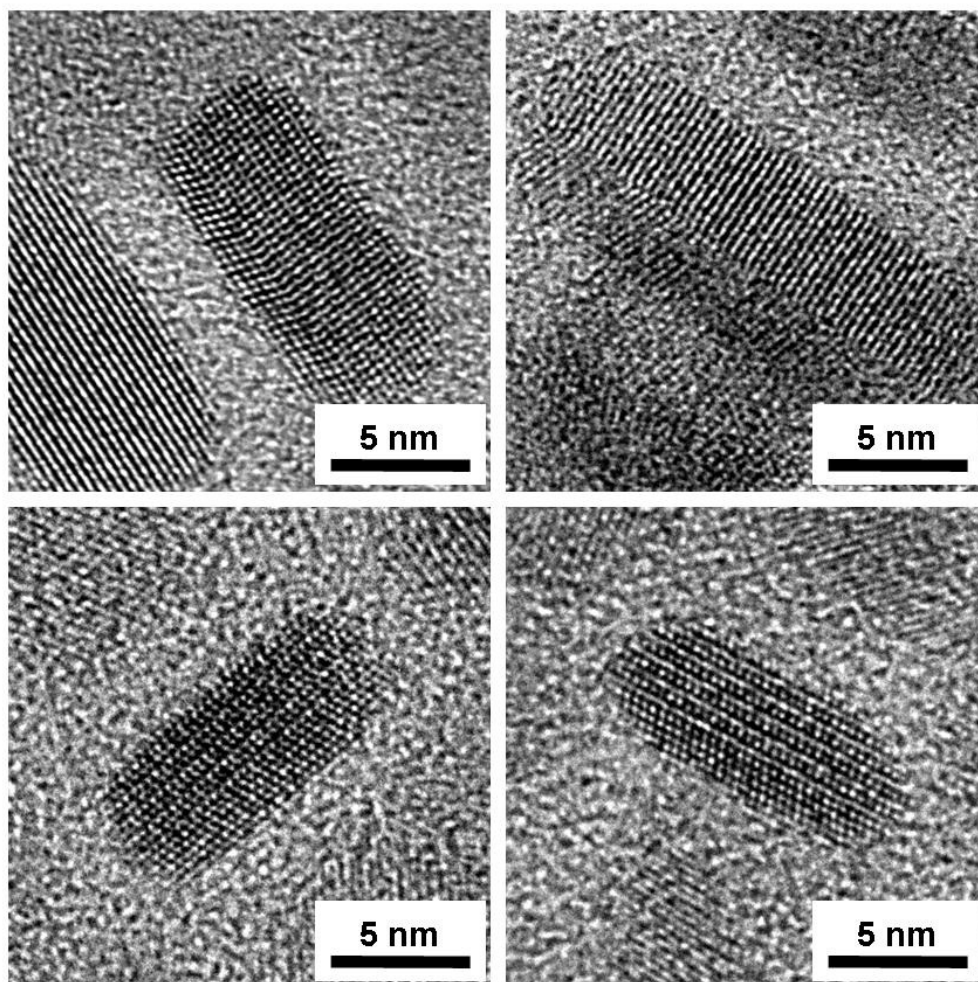
Figure 5.11. HRTEM images of CuInS$_2$ nanodisks synthesized using Cu(acac)$_2$ in place of CuCl. The nanodisks exhibit wurtzite-chalcopyrite polytypism, but the chalcopyrite domains are more significant in these nanodisks, as also confirmed by XRD.
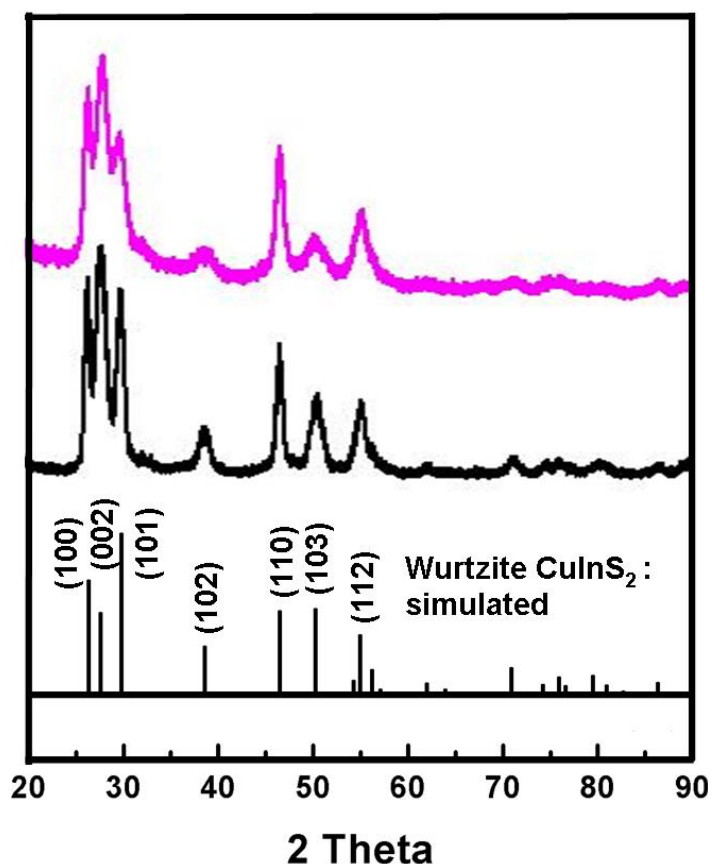
Figure 5.12. XRD of CuInS$_2$ nanodisks synthesized using either CuCl (black curve) or Cu(acac)$_2$ (pink curve) as the Cu source. The slight difference in relative peak intensities of the two samples indicates that the nanodisks made with Cu(acac)$_2$ are slightly richer in chalcopyrite content.

5.4 CONCLUSION

In conclusion, a new synthetic route was developed that produced monodisperse CuInS$_2$ nanodisks. The nanodisks exhibited wurtzite-chalcopyrite polytypism with the coexistence of both wurtzite and chalcopyrite domains interface across $(002)_w/(112)_{ch}$ stacking faults. This is the first example of wurtzite-chalcopyrite polytypism in I-III-VI$_2$ compounds that we are aware of.

5.5 REFERENCES

(1)   Pan, D. C.; An, L. J.; Sun, Z. M.; Hou, W.; Yang, Y.; Yang, Z. Z.; Lu, Y. F. *J Am Chem Soc* **2008**, *130*, 5620.

(2)   Connor, S. T.; Hsu, C. M.; Weil, B. D.; Aloni, S.; Cui, Y. *J Am Chem Soc* **2009**, *131*, 4962-4966.

(3)   Qi, Y. X.; Liu, Q. C.; Tang, K. B.; Liang, Z. H.; Ren, Z. B.; Liu, X. M. *J Phys Chem C* **2009**, *113*, 3939-3944.

(4)   Koo, B.; Patel, R. N.; Korgel, B. A. *Chem Mater* **2009**, *21*, 1962-1966.

(5)   Nose, K.; Soma, Y.; Omata, T.; Otsuka-Yao-Matsuo, S. *Chem Mater* **2009**, *21*, 2607-2613.

(6)   Batabyal, S. K.; Tian, L.; Venkatram, N.; Ji, W.; Vittal, J. J. *J Phys Chem C* **2009**, *113*, 15037-15042.

(7)   Ghezelbash, A.; Korgel, B. A. *Langmuir* **2005**, *21*, 9451-9456.

(8)   Sigman, M. B.; Ghezelbash, A.; Hanrath, T.; Saunders, A. E.; Lee, F.; Korgel, B. A. *J Am Chem Soc* **2003**, *125*, 16050-16057.

Chapter 6: Wurtzite CuInSe$_2$ and Cu(In$_x$Ga$_{1-x}$)Se$_2$ (CIGS) Nanocrystals: Synthesis, Structure, and Polytypism

6.1 INTRODUCTION

Nanocrystals of CIGS materials are being developed as a printable "solar pigment." A variety of CIGS nanocrystals have recently been synthesized and prototype PVs have been made from these materials.[51-53,55,117] In some cases, unexpected crystal structure has been observed.[66,77-81] For example, Pan, *et al.* recently found that their CuInS$_2$ nanocrystals exhibited a wurtzite (hexagonal) crystal structure, instead of the expected cubic phase.[66] I have also observed wurtzite CuInS$_2$ in nanocrystals.[79] This is very interesting, as the wurtzite phase is not stable at room temperature in the bulk relative to chalcopyrite and other cubic phases such as sphalerite or ordered vacancy compound.[76] Wurtzite CuInS$_2$ occurs only as a high temperature phase (1045-1090 ^{o}C).[76] In contrast, wurtzite phases of CuInSe$_2$ and CIGS are not known to occur in the bulk, and have not been observed in nanocrystals.[83]

Synthetic routes for CuInSe$_2$ and CIGS nanocrystals have recently been developed by several research groups.[43,44,46-53,65,117-119] Alternative phases to chalcopyrite have been observed in CuInSe$_2$ nanocrystals, such as sphalerite (compositionally disordered)[52] and ordered vacancy compounds,[50] however, wurtzite crystal structure has not been observed.[83] In this chapter, I report CuInSe$_2$ and Cu(In$_x$Ga$_{1-x}$)Se$_2$ nanocrystals with wurtzite (hexagonal) crystal structure.

X-ray diffraction (XRD) revealed wurtzite crystal structure in CuInSe$_2$ and Cu(In$_x$Ga$_{1-x}$)Se$_2$ nanocrystals. Extenstive high resolution transmission electron microscopy (TEM) imaging showed that the nanocrystals in fact were polytypic, consisting of both chalcopyrite and wurtzite crystal structure within the same

nanocrystals, similar to what I showed to be the case in $CuInS_2$ nanodisks.[79]   Elemental mapping in the nanocrystals by nanobeam energy dispersive spectroscopy (EDS) line scans revealed compositional variations between the chalcopyrite and wurtzite phases.

6.2 EXPERIMENTAL SECTION

Copper(I) chloride (CuCl, Aldrich, 99.995+ %), indium(III) acetylacetonate $(In(acac)_3$, Aldrich, 99.99 %), gallium(III) chloride $(GaCl_3$, Aldrich, 99.999 %), selenourea (ACROS, 99.9+ %), selenium (Aldrich, 99.99 %), and octadecylamine (Aldrich, 97 %) were purchased and used as received.

6.2.1 Nanocrystal Synthesis

In a typical wurtzite $CuInSe_2$ nanocrystal synthesis, a mixture of 0.05 g of CuCl (0.5 mmol of Cu), 0.206 g of $In(acac)_3$ (0.5 mmol of In), 0.123 g of selenourea (1.0 mmol of Se), and 10 g of octadecylamine is vigorously stirred and degassed in the reaction flask for 30 minutes at 80 ℃ by pulling vacuum on a Schlenk line. (For the synthesis of wurtzite $CuIn_{0.8}Ga_{0.2}Se_2$, 0.25 mmol of $In(acac)_3$ and 0.25 mmol of $GaCl_3$ are used and for the synthesis of wurtzite $CuIn_{0.6}Ga_{0.4}Se_2$, 0.25 mmol of $In(acac)_3$ and 0.375 mmol of $GaCl_3$ are used instead of 0.5 mmol $In(acac)_3$ described above.)   The solution color is black.   The flask is then filled with nitrogen and heated to 240 ℃ at a rate of 15 ℃/min. During the heating process, smoke begins to evolve at about 200 ℃ and the color turns a darker color, indicating nanocrystal nucleation and growth.   After allowing the reaction to proceed for one hour, the reaction flask is removed from the heating mantle and allowed to cool to room temperature.   30 mL of ethanol is then added to precipitate the nanocrystals, followed by centrifugation at 7000 rpm for 3 minutes.   The supernatant is discarded.   The nanocrystals redisperse in a variety of non-polar organic solvents, including chloroform, hexane, and toluene.   The dispersions are centrifuged again at

6000 rpm for 1 min to remove inadequately capped nanocrystals. The washing process is repeated in order to remove remaining reactants and by-products. A typical reaction yields approximately 120 mg of wurtzite $CuInSe_2$ nanocrystals.

6.2.2 Characterization Methods

Nanocrystals were imaged by transmission electron microscopy (TEM). TEM images were acquired on either a JEOL 2010F microscope equipped with a field emission gun operated at 200 kV or an FEI Tecnai microscope operated at 80 kV. TEM samples were prepared by drop-casting from chloroform dispersions onto carbon-coated Ni TEM grids (200-mesh, Electron Microscopy Sciences). The JEOL 2010F has an Oxford X-ray energy dispersive spectroscopy (EDS) detector, which was used for elemental analysis. XRD patterns were obtained from nanocrystal films that were approximately 200 μm thick on quartz substrates. A Bruker-Nonius D8 Advance powder diffractometer with Cu Kα radiation ($\lambda = 1.54$ Å) was used with a scan rate of 6 deg/min in 0.01 deg increments, collecting for 12 hr with that sample rotating at 15 deg/min. Room temperature UV-visible absorbance spectra were collected on a Varian Cary 5000 Scan spectrophotometer with samples dispersed in chloroform in quartz cuvettes.

6.3 RESULTS AND DISCUSSION

6.3.1 Synthesis of wurtzite $CuInSe_2$ Nanocrystals

$CuInSe_2$ and $Cu(In_xGa_{1-x})Se_2$ nanocrystals with wurtzite crystal structure were synthesized by combining copper(I) chloride (CuCl), indium(III) acetylacetonate (In(acac)$_3$), gallium(III) chloride (GaCl$_3$), and selenourea in octadecylamine at air-free conditions at 240 ^{o}C:
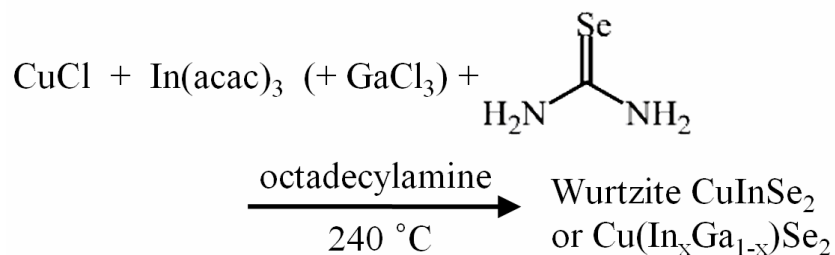
Figure 6.1. Reaction scheme for wurtzite $CuInSe_2$ nanocrystal synthesis.

Note that similar reaction conditions, but with the use of elemental Se as the Se source, leads to chalcopyrite $CuInSe_2$ and CIGS nanocrystals.[44,48,49,51-53,117,119] The use of selenourea was necessary to form wurtzite nanocrystals, as well as careful control of the reaction procedure. But we had also previously synthesized monodisperse chalcopyrite $CuInSe_2$ nanocrystals with a trigonal pyramidal shape by initially combining metal precursors in oleylamine and subsequently injecting selenourea at a low temperature, followed by heating to 240 °C.[65] Wurtzite $CuInSe_2$ and CIGS nanocrystals are obtained only when metal precursors and selenourea are mixed together in octadecylamine prior to heating.

Figure 6.2 shows TEM images of $CuInSe_2$ and $CuIn_{0.8}Ga_{0.2}Se_2$ nanocrystals with wurtzite crystal structure, synthesized by heating metal precursors and selenourea in oleylamine at 240 °C. Unlike $CuInSe_2$ nanocrystals synthesized by other methods, these $CuInSe_2$ nanocrystals have a disk-like shape (Figures 6.2a and 6.2c). Combining metal precursors and selenourea may play a role to make this different shape of $CuInSe_2$ nanocrystals. Similarly, we have found that the use of thiourea resulted in a disk shape under a similar condition.[79] Their average diameter and thickness were 16.7 nm and 9.4 nm, respectively. The disk shape was confirmed by TEM imaging of the substrate at different tilt angles. Figure 6.3 shows a field of $CuInSe_2$ nanocrystals imaged by TEM

before and after tilting the sample. When the sample was tilted by 12.8°, the edges of the particles appeared to overlap, indicating that the nanocrystals had a disk shape and were oriented on their edges. This type of image analysis has been used in the past to discern disks from rods in the past for a variety of other materials.[111,120]
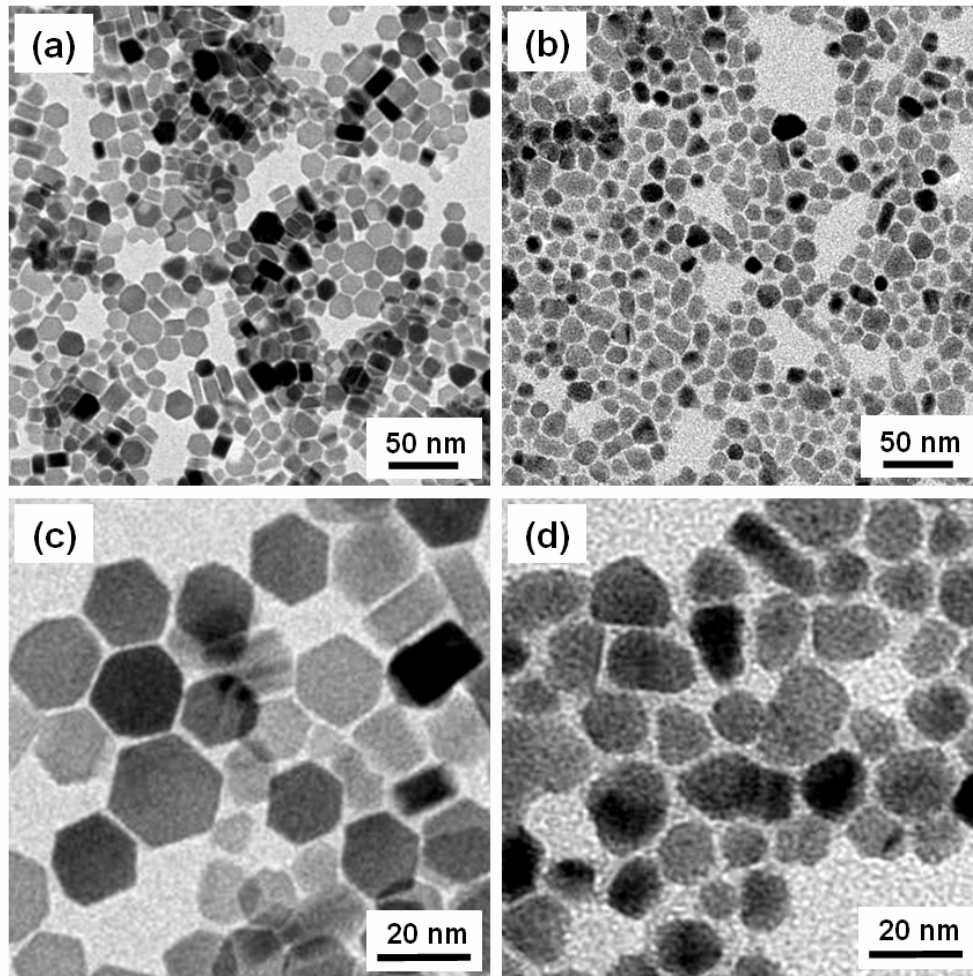
Figure 6.2. TEM images of (a, c) $CuInSe_2$ and (b, d) $CuIn_{0.8}Ga_{0.2}Se_2$ nanocrystals. The $CuInSe_2$ nanocrystals were shaped like disks, with average diameter of 16.7 nm and thickness of 9.4 nm. The $CuIn_{0.8}Ga_{0.2}Se_2$ nanocrystals had a tapered bullet shape with average dimensions of 11.3 nm (short side) and 16.9 nm (long side).
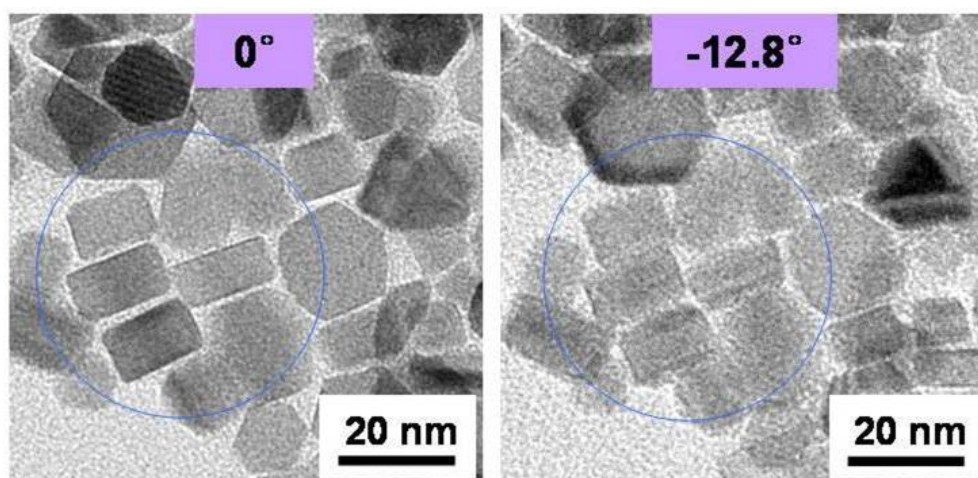
Figure 6.3. TEM images of CuInSe$_2$ nanocrystals viewed with the substrate at different tilt angles. The nanodisks circled in blue are oriented on their edges.

Figures 6.2b and 6.2d show TEM images of CuIn$_{0.8}$Ga$_{0.2}$Se$_2$ (CIGS) nanocrystals made by including a Ga reactant in the reaction. These CIGS nanocrystals have a tapered shape, like a bullet. The average size of the CuIn$_{0.8}$Ga$_{0.2}$Se$_2$ nanocrystals is 11.3 nm (short side) and 16.9 nm (long side). From EDS, the Cu:In:Se composition of the disk-shaped CuInSe$_2$ nanocrystals was 1:1:2 (atomic ratios) and tapered the Cu:In:Ga:Se ratio of the CuIn$_{0.8}$Ga$_{0.2}$Se$_2$ nanocrystals was nearly 1:0.8:0.2:2 in Figure 6.4. The band gap energies determined from the absorption edge in UV-vis-NIR absorbance spectra were 1.036 eV and 1.136 eV, which corresponds to the expected band gap energy of 1.04 eV and 1.13 eV typical of bulk CuInSe$_2$ and CuIn$_{0.8}$Ga$_{0.2}$Se$_2$ (Figure 6.5).[121]
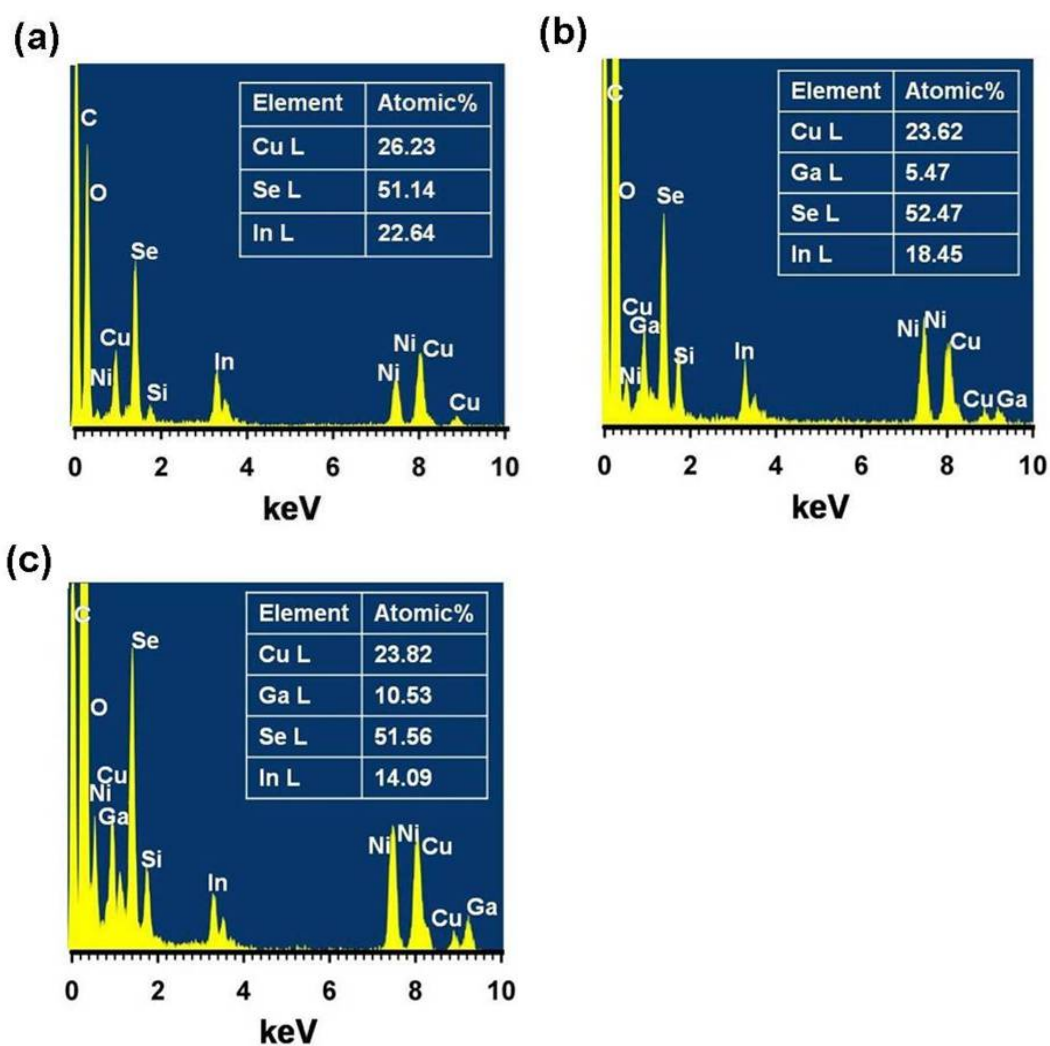
Figure 6.4. Atomic ratios of (a) CuInSe$_2$, (b) CuIn$_{0.8}$Ga$_{0.2}$Se$_2$, and (c) CuIn$_{0.6}$Ga$_{0.4}$Se$_2$ nanocrystals measured by EDS. Averaged ratios over several nanocrystals are nearly (a) Cu:In:Se=1:1:2, (b) Cu:In:Ga:Se=1:0.8:0.2:2, and (c) Cu:In:Ga:Se=1:0.6:0.4:2, respectively. The Ni, C and Si signals are from the nickel grid, the carbon support and the background in the TEM.
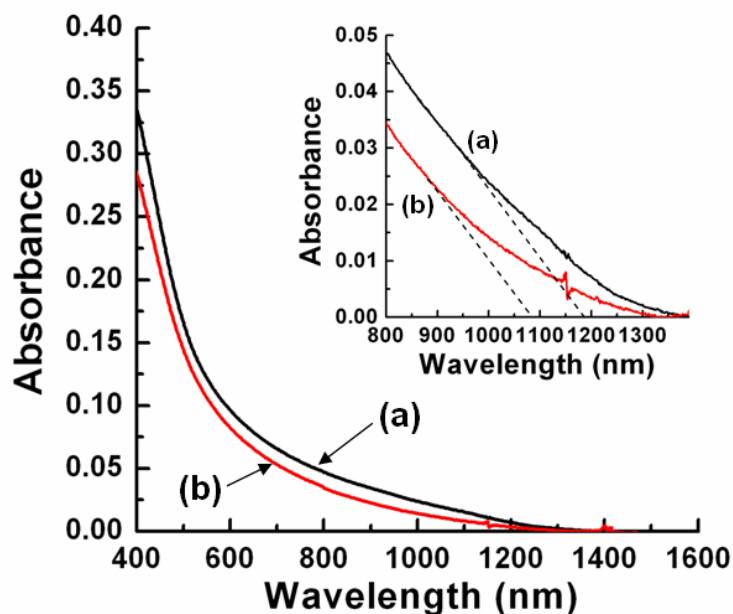
Figure 6.5. Room temperature UV-vis-NIR absorbance spectra of $CuInSe_2$ and $CuIn_{0.8}Ga_{0.2}Se_2$ nanocrystals dispersed in chloroform. The absorption edges correspond to optical gaps of 1.04 and 1.13 eV, respectively.

6.3.2 Wurtzite crystal structure

XRD (Figure 6.6) revealed that the nanocrystals had a wurtzite crystal structure. EDS confirmed that the nanocrystals were composed of $CuInSe_2$ and CIGS. The wurtzite (100), (101), and (103) peaks were weaker for the $CuIn_{0.8}Ga_{0.2}Se_2$ nanocrystals (Figure 6.6b) than the $CuInSe_2$ nanocrystals, but were still apparent. The (002) peak positions from the $CuInSe_2$ and $CuIn_{0.8}Ga_{0.2}Se_2$ nanocrystals are compared in the inset in Figure 6.6. The (002) peaks appear at higher 2theta for the nanocrystals with higher Ga content, consistent with the expected smaller lattice spacing. CIGS nanocrystals with higher Ga content were also synthesized—$CuIn_{0.6}Ga_{0.4}Se_2$ nanocrystals—and the XRD patterns also showed these materials to have wurtzite crystal structure (Figure 6.6c). See the TEM image of the nanocrystals in Figure 6.7. The reference peak positions for

the (002) peaks from $CuIn_{0.8}Ga_{0.2}Se_2$ and $CuIn_{0.6}Ga_{0.4}Se_2$ were determined as a function of Ga composition (red and blue vertical lines in an inset of Figure 6.6) using Vegard's law, using the (112) peak positions of chalcopyrite $CuInSe_2$ (JCPDS#00-040-1487) and $CuIn_{0.7}Ga_{0.3}Se_2$ (JCPDS#00-035-1102).   The (112) peak positions of the chalcopyrite compounds are equivalent to the (002) wurtzite peak positions.
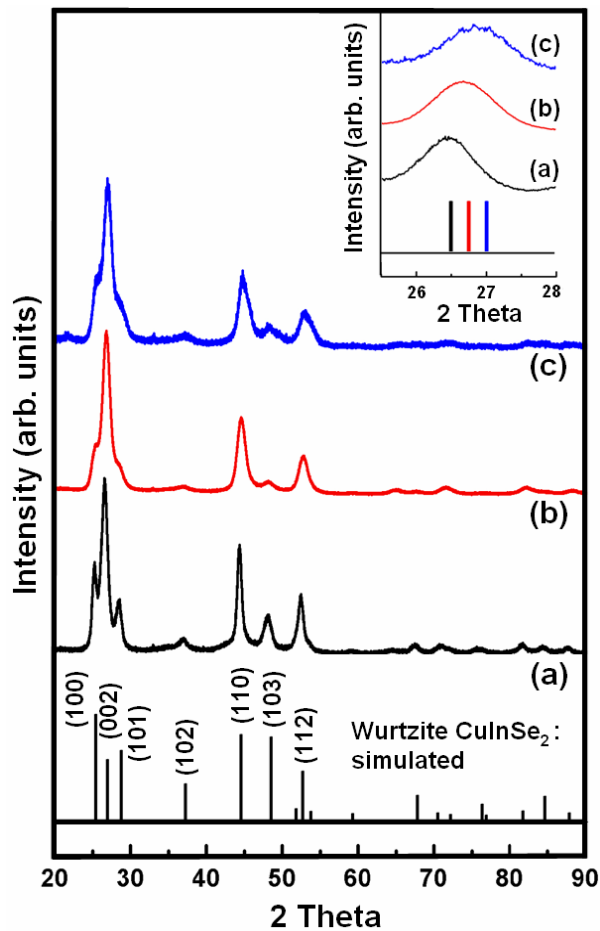
Figure 6.6.   XRD of (a) $CuInSe_2$, (b) $CuIn_{0.8}Ga_{0.2}Se_2$, and (c) $CuIn_{0.6}Ga_{0.4}Se_2$ nanocrystals.   The stick patterns for wurtzite $CuInSe_2$ shown were calculated with the CaRIne Crystallography 3.1 program with space group, P63mc (No. 186) and unit cell dimensions $a = b = 4.085(8)$ Å, $c = 6.676(5)$ Å).   (Inset) Magnification of the (002) peaks compared to the expected peak positions based on Vegard's law using 112 peak positions of chalcopyrite $CuInSe_2$ (JCPDS#00-040-1487) and $CuIn_{0.7}Ga_{0.3}Se_2$ (JCPDS#00-035-1102).
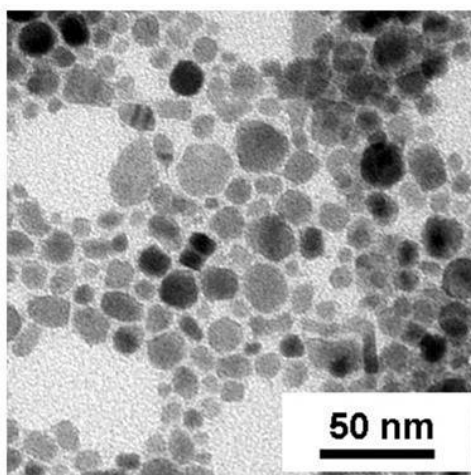
Figure 6.7. TEM image of $CuIn_{0.6}Ga_{0.4}Se_2$ nanocrystals.

6.3.3 HRTEM analysis

Figures 6.8a and 6.8b show high resolution TEM images of the $CuInSe_2$ nanodisks with two different orientations on the substrate. The FFT of the image in Figure 6.8a corresponds to a crystal with a wurtzite (hexagonal) structure with the nanodisk being viewed down the [001] zone axis (i.e., the *c*-axis of the wurtzite $CuInSe_2$ crystal structure). The (100) spots in the FFT do not appear in the chalcopyrite structure. Figure 6.8b shows [002] growth direction (thickness direction) of the $CuInSe_2$ nanodisks. The top and bottom faces of the disk are bounded by wurtzite {002} planes.

6.3.3.1 Polytypism of nanocrystals

Figure 6.8c shows that the $CuInSe_2$ nanodisks exhibit structural polytypism, with both wurtzite and chalcopyrite domains in the same nanocrystal, similar to we observed recently in the case of $CuInS_2$ nanodisks synthesized using metal chlorides and thiourea.[79] The wurtzite (002), (110), and (112) peaks—corresponding to chalcopyrite—in the XRD patterns have a higher intensity revealed the presence of

93

wurtzite-chalcopyrite polytypism in the same way shown in the case of wurtzite $CuInS_2$ nanodisks.   Polytypism was also observed in bullet-shaped $CuIn_{0.8}Ga_{0.2}Se_2$ nanocrystals. Figure 6.8d shows a $CuIn_{0.8}Ga_{0.2}Se_2$ nanocrystal with both wurtzite and chalcopyrite crystal domains.   The $CuIn_{0.8}Ga_{0.2}Se_2$ nanocrystals exhibited regions with significant amounts of twinning, which was not observed in the $CuInSe_2$ nanodisks.   The nanocrystal in Figure 6.8d when viewed down the $[-120]_W$ zone axis shows the wurtzite-twinning-chalcopyrite polytypism.   In Figure 6.8d, the yellow arrows in the FFT point to the diffraction spots corresponding to the chalcopyrite domain of the nanocrystals, the pink arrows point to the diffraction spots associated with the twin planes.   Since the twinning structure has smaller number of stacking faults in chalcopyrite than wurtzite (Note that chalcopyrite → ABCABCABCABC, twinning → ABCABC/BACBA, and wurtzite → AB/AB/AB/AB/AB/AB.   "/" indicates a stacking fault.), the XRD patterns of $CuIn_{0.8}Ga_{0.2}Se_2$ nanocrystals showed stronger peaks corresponding to chalcopyrite than $CuInSe_2$ nanodisks.   Additional HRTEM images of polytypic $CuInSe_2$ and $CuIn_{0.8}Ga_{0.2}Se_2$ nanocrystals are shown in Figures 6.9 and 6.10.
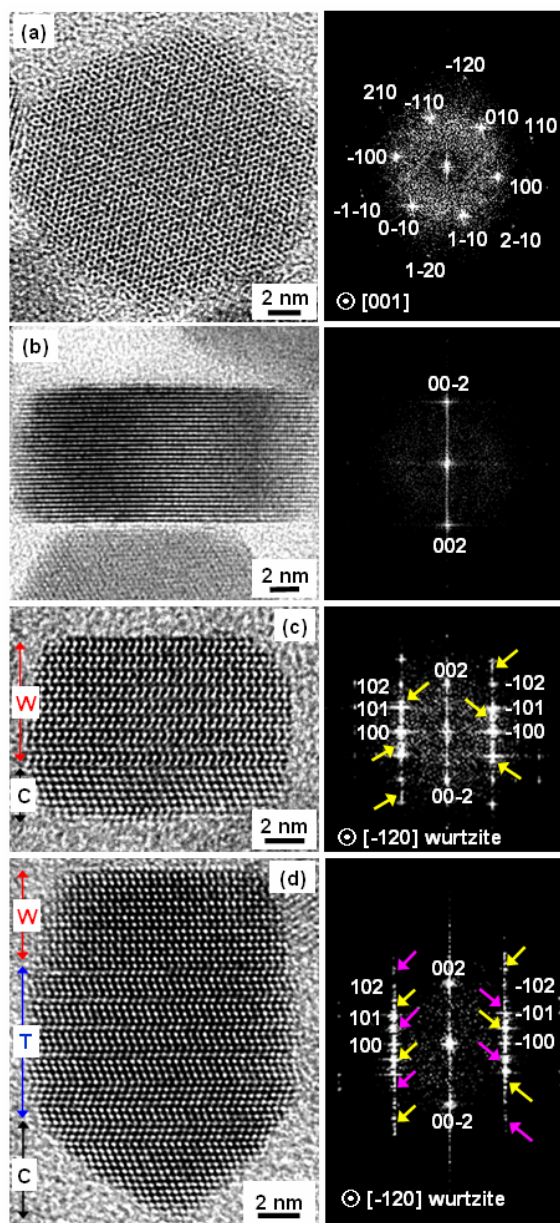
Figure 6.8. HRTEM images and associated Fast Fourier transforms (FFTs) of (a-c) CuInSe$_2$ nanodisks and (d) CuIn$_{0.8}$Ga$_{0.2}$Se$_2$ nanocrystals. (a) and (b) show CuInSe$_2$ nanodisks with two different orientations on the substrate. (c) and (d) showed HRTEM images and FFTs with [-120]$_W$ zone axis of CuInSe$_2$ and CuIn$_{0.8}$Ga$_{0.2}$Se$_2$ nanocrystals, respectively. The FFT shows multiple diffraction spots, where yellow arrows indicated chalcopyrite structure at the lower parts of both and pink arrows revealed twinning structure at the middle part of CuIn$_{0.8}$Ga$_{0.2}$Se$_2$ nanocrystals. ("W", "C", and "T" indicate wurtzite, chalcopyrite, and twinning, respectively.)
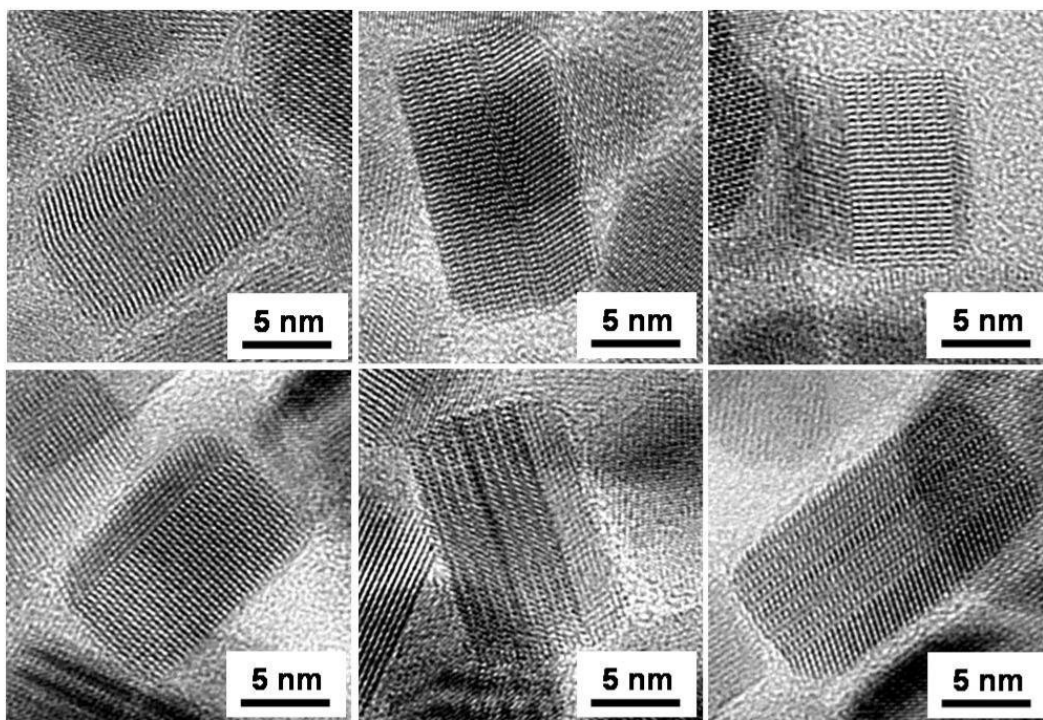
Figure 6.9. HRTEM images revealing polytypism of wurtzite $CuInSe_2$ nanodisks.
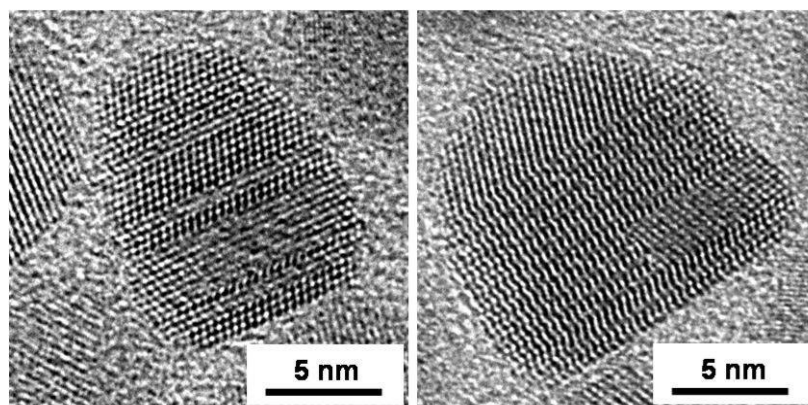
Figure 6.10. HRTEM images showing polytypism of wurtzite $CuIn_{0.8}Ga_{0.2}Se_2$ nanoparticles.

6.3.4 Compositional analysis

The compositional profiles along the length of individual nanocrystals were determined by STEM-EDS mapping. Drift corrected spectrum profiles were obtained by initially selecting a reference area in STEM image and regulating the scanning direction not to stray from the reference area. This technique was used in my previous work.[122] Figure 6.11 shows EDS line scans of two different nanocrystals. The composition along the length of the nanocrystals is relatively uniform, as expected, with stoichiometric ratios of Cu:In:Se=1:1:2 for $CuInSe_2$ and Cu:In:Ga:Se=1:0.8:0.2:2 for $CuIn_{0.8}Ga_{0.2}Se_2$ when averaged through the whole nanocrystal. However, closer examination revealed a slight difference in composition between the chalcopyrite and wurtizite domains. One part of the nanocrystal is slightly Cu-rich (~10.3%) and the other part is slightly In-rich (~11.4%). It turned out to be relatively easy to correlate the measured composition profiles with the crystal structure, because the shape of the nanocrystals was influenced by the crystal structure. For both the $CuInSe_2$ and $CuIn_{0.8}Ga_{0.2}Se_2$ nanocrystals, the chalcopyrite domains exhibited significant tapering in their diameter, whereas the wurtzite domains had less. In the $CuIn_{0.8}Ga_{0.2}Se_2$ nanocrystals, the wurtzite part of the nanocrystals had uniform diameter. This enabled an easy determination of the chalcopyrite and wurtzite domains in the nanocrystal that could be correlated with the EDS maps, without the need to resolve the lattice with HRTEM. In fact, EDS line scans after HRTEM imaging had very low intensity possibly because a previous electron beam transmission through the nanoparticles consumed a significant amount of X-ray emission, prior to operating EDS line scans (Figure 6.12). The chalcopyrite domains were found to be slightly Cu-rich (~10.3%) and the wurtzite domains were slightly In-rich (~11.4%). This is possibly due to the surface reconstruction of $CuInSe_2$ crystal facets, such as Cu-on-In (Cu_{In}) or In-on-Cu (In_{Cu}).[114]
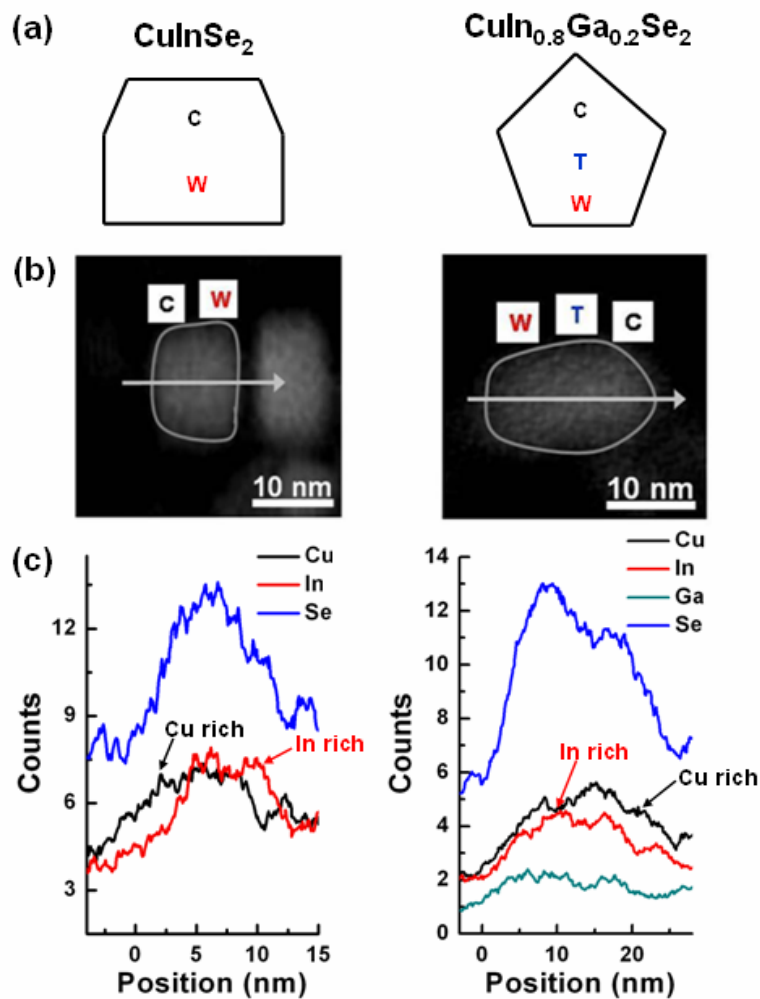
Figure 6.11. (a) Illustration showing a relation between shape and crystal structure, (b) Z-contrast images obtained by high angle annular dark field (HAADF) scanning transmission electron microscopy (STEM), and (c) EDS line scans of $CuInSe_2$ nanodisks and $CuIn_{0.8}Ga_{0.2}Se_2$ nanocrystals viewed in their sides. The average atomic ratios obtained from EDS line scans were close to corresponding stoichiometric ratios. However, a more careful look showed that chalcopyrite parts were Cu-rich and wurtzite parts were In-rich in general.
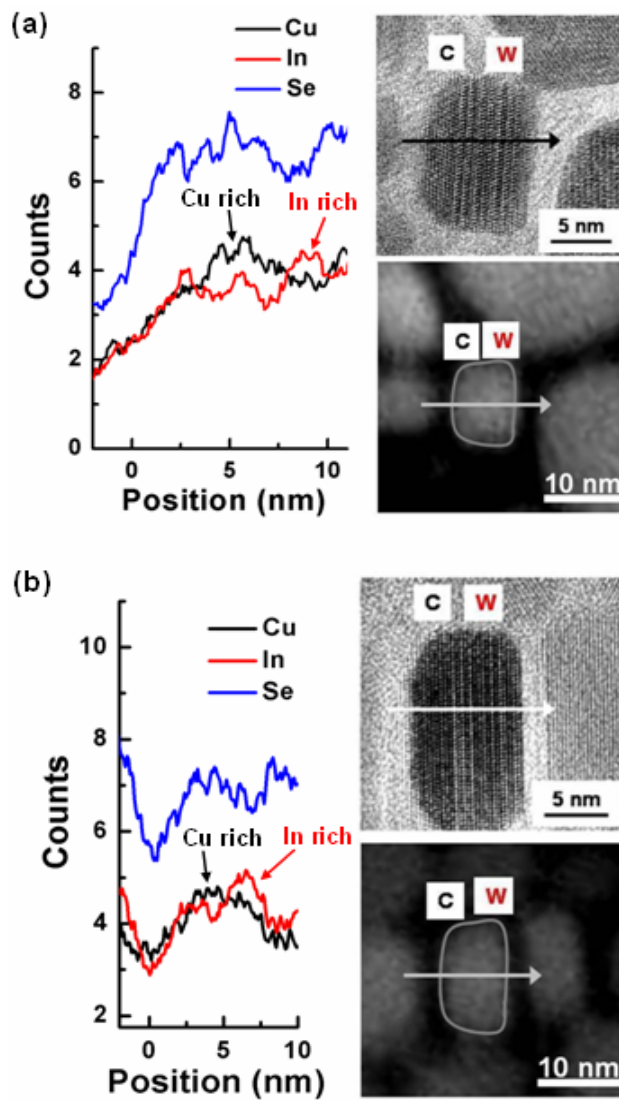
Figure 6.12. EDS line scans after HRTEM imaging. Each figure shows EDS line scans and corresponding HRTEM and Z-contrast images of polytypic wurtzite CuInSe$_2$ nanocrystals. It is shown that the EDS signal counts after HRTEM imaging were relatively low (<10).

6.4 CONCLUSIONS

In summary, we have observed wurtzite crystal structure in CuInSe$_2$ and Cu(In$_x$Ga$_{1-x}$)Se$_2$ nanocrystals. The nanocrystals exhibit wurtzite-chalcopyrite

polytypism as we recently observed in the CuInS$_2$ nanodisks.[79] EDS line scan was performed to reveal a slight deviation of atomic composition ratio in individual CuInSe$_2$ and CIGS nanocrystals.

6.5 REFERENCES

(1)   Panthani, M. G.; Akhavan, V.; Goodfellow, B.; Schmidtke, J. P.; Dunn, L.; Dodabalapur, A.; Barbara, P. F.; Korgel, B. A. *J Am Chem Soc* **2008**, *130*, 16770-16777.

(2)   Guo, Q.; Kim, S. J.; Kar, M.; Shafarman, W. N.; Birkmire, R. W.; Stach, E. A.; Agrawal, R.; Hillhouse, H. W. *Nano Lett* **2008**, *8*, 2982-2987.

(3)   Tang, J.; Hinds, S.; Kelley, S. O.; Sargent, E. H. *Chem Mater* **2008**, *20*, 6906-6910.

(4)   Ahn, S.; Kim, K.; Yoon, K. *Curr Appl Phys* **2008**, *8*, 766-769.

(5)   Guo, Q.; Ford, G. M.; Hillhouse, H. W.; Agrawal, R. *Nano Lett* **2009**, *9*, 3060-3065.

(6)   Pan, D. C.; An, L. J.; Sun, Z. M.; Hou, W.; Yang, Y.; Yang, Z. Z.; Lu, Y. F. *J Am Chem Soc* **2008**, *130*, 5620.

(7)   Connor, S. T.; Hsu, C. M.; Weil, B. D.; Aloni, S.; Cui, Y. *J Am Chem Soc* **2009**, *131*, 4962-4966.

(8)   Qi, Y. X.; Liu, Q. C.; Tang, K. B.; Liang, Z. H.; Ren, Z. B.; Liu, X. M. *J Phys Chem C* **2009**, *113*, 3939-3944.

(9)   Koo, B.; Patel, R. N.; Korgel, B. A. *Chem Mater* **2009**, *21*, 1962-1966.

(10)   Nose, K.; Soma, Y.; Omata, T.; Otsuka-Yao-Matsuo, S. *Chem Mater* **2009**, *21*, 2607-2613.

(11)   Batabyal, S. K.; Tian, L.; Venkatram, N.; Ji, W.; Vittal, J. J. *J Phys Chem C* **2009**, *113*, 15037-15042.

(12)   Binsma, J. J. M.; Giling, L. J.; Bloem, J. *J Cryst Growth* **1980**, *50*, 429-436.

(13)   Park, J. S.; Dong, Z.; Kim, S.; Perepezko, J. H. *J Appl Phys* **2000**, *87*, 3683-3690.

(14)   Li, B.; Xie, Y.; Huang, J. X.; Qian, Y. T. *Adv Mater* **1999**, *11*, 1456-1459.

(15) Malik, M. A.; O'Brien, P.; Revaprasadu, N. *Adv Mater* **1999**, *11*, 1441-1444.

(16) Castro, S. L.; Bailey, S. G.; Raffaelle, R. P.; Banger, K. K.; Hepp, A. F. *Chem Mater* **2003**, *15*, 3142-3147.

(17) Yang, Y. H.; Chen, Y. T. *J Phys Chem B* **2006**, *110*, 17370-17374.

(18) Gou, X. L.; Cheng, F. Y.; Shi, Y. H.; Zhang, L.; Peng, S. J.; Chen, J.; Shen, P. W. *J Am Chem Soc* **2006**, *128*, 7222-7229.

(19) Zhong, H. Z.; Li, Y. C.; Ye, M. F.; Zhu, Z. Z.; Zhou, Y.; Yang, C. H.; Li, Y. F. *Nanotechnology* **2007**, *18*.

(20) Peng, H. L.; Schoen, D. T.; Meister, S.; Zhang, X. F.; Cui, Y. *J Am Chem Soc* **2007**, *129*, 34-35.

(21) Allen, P. M.; Bawendi, M. G. *J Am Chem Soc* **2008**, *130*, 9240.

(22) Nose, K.; Omata, T.; Otsuka-Yao-Matsuo, S. *J Phys Chem C* **2009**, *113*, 3455-3460.

(23) Koo, B.; Patel, R. N.; Korgel, B. A. *J Am Chem Soc* **2009**, *131*, 3134.

(24) Puntes, V. F.; Zanchet, D.; Erdonmez, C. K.; Alivisatos, A. P. *J Am Chem Soc* **2002**, *124*, 12874-12880.

(25) Sigman, M. B.; Ghezelbash, A.; Hanrath, T.; Saunders, A. E.; Lee, F.; Korgel, B. A. *J Am Chem Soc* **2003**, *125*, 16050-16057.

(26) Wei, S. H.; Zhang, S. B.; Zunger, A. *Appl Phys Lett* **1998**, *72*, 3199-3201.

(27) Koo, B.; Korgel, B. A. *Nano Lett* **2008**, *8*, 2490-2496.

(28) Zhang, S. B.; Wei, S. H. *Phys Rev B* **2002**, *65*.

Chapter 7: Conclusions and future research directions

7.1 CONCLUSIONS

7.1.1 CdTe/CdSe/CdTe heterojunction nanorods

Chapeter 2 showed that the rates of heterojunction interdiffusion and coalescence of CdTe/CdSe/CdTe nanorods were reported and compared to model predictions. The Se and Te composition profiles were mapped in individual nanorods aged in hot solvents for different amounts of time to determine the Te in CdSe diffusion coefficient and evaluate the influence of strain on the interdiffusion rates across the heterojunctions. Although there is strain at the epitaxial CdTe/CdSe interface due to the lattice mismatch, this strain does not appear to influence the rate of Te-Se interdiffusion. The measured rod-to-sphere coalescence rates were compared to rates predicted using a continuum viscous flow model for nanorod-to-sphere coalescence. Se and Te interdiffusion rates appear to be independent of strain at the CdSe/CdTe interface and the continuum model gives a reasonable approximation to the measured coalescence rates.

7.1.2 CuInSe$_2$ nanocrystals

7.1.2.1 Synthesis and characterization

In Chapter 3, it was shown that monodisperse CuInSe$_2$ nanocrystals were synthesized. They exhibit a trigonal pyramid shape as a result of their chalcopyrite crystal structure and the corresponding surface facet polarity. Oleylamine is an effective capping ligand to control CuInSe$_2$ nanocrystal growth, but when present in excess in solution it can also etch the nanocrystal surfaces. When dropcast onto carbon substrates, the nanocrystals deposit on their (114) surfaces and form close-packed monolayers with triangular order. When dropcast on silicon substrates (with native

102

oxide), the nanocrystals do not exhibit the same facet-selective deposition and do not form ordered monolayers.

7.1.2.2 Effect on monodispersity

Chapter 4 suggested that how excess CuCl could affect the formation of monodisperse trigonal pyramidal $CuInSe_2$ nanocrystals. It was revealed that 45 % excess CuCl lead the most monodisperse trigonal pyramidal $CuInSe_2$ nanocrystals in their size and shape. In addition, the monodispersity trend was suddenly changed around 45 % of excess CuCl, accompanying with the transform of crystals structure from $CuInSe_2$ to Cu_2Se. The formation mechanism of monodisperse trigonal pyramidal $CuInSe_2$ nanocrystals was suggested with regard to excess amount of CuCl precursor, based on the nucleation-growth model of colloidal nanocrystal formation.

7.1.3 Wurtzite $CuInS_2$ and $CuInSe_2$ nanocrystals

Chapters 5 and 6 showed that wurtzite-type I-III-VI_2 nanocrystals were synthesized.

7.1.3.1 Wurtzite $CuInS_2$ nanodisks

A new synthetic route was developed that produced monodisperse $CuInS_2$ nanodisks as shown in Chapter 5. The nanodisks exhibited wurtzite-chalcopyrite polytypism with the coexistence of both wurtzite and chalcopyrite domains interface across $(002)_w/(112)_{ch}$ stacking faults. This is the first example of wurtzite-chalcopyrite polytypism in I-III-VI_2 compounds that we are aware of.

7.1.3.2 Wurtzite $CuInSe_2$ and$Cu(In_xGa_{1-x})Se_2$ nanocrystals

It was observed that $CuInSe_2$ and $Cu(In_xGa_{1-x})Se_2$ nanocrystals had wurtzite crystal structure as shown in Chapter 6. X-ray diffraction (XRD) revealed wurtzite crystal structure in $CuInSe_2$ and $Cu(In_xGa_{1-x})Se_2$ nanocrystals. Extensive high

resolution transmission electron microscopy (TEM) imaging showed that the nanocrystals in fact were polytypic, consisting of both chalcopyrite and wurtzite crystal structure within the same nanocrystals, similar to what I showed to be the case in $CuInS_2$ nanodisks. Elemental mapping in the nanocrystals by nanobeam energy dispersive spectroscopy (EDS) line scans revealed compositional variations between the chalcopyrite and wurtzite phases.

7.2 FUTURE RESEARCH DIRECTIONS

7.2.1 Model for coalescence and interdiffusion

Although the continuum model suggested for the coalescence and interdiffusion of CdTe/CdSe/CdTe heterostructures gives a reasonable approximation to the measured coalescence rates, there are many questions that remain to be answered about the coalescence rate of non-spherical nanocrystals, which require more accurate predictive models for coalescence that can be compared directly to experimental measurements such as these. For example, how significantly do the capping ligands influence the coalescence rates? The adsorbed capping ligands should lower the nanocrystal surface tension,[123] which should in turn slow the coalescence rate. The role of the ligands in slowing nanorod coalescence could be particularly influential in situations in which nanocrystals aggregate into linear chains, as in the oriented attachment mechanism.[35,124] In the case of the CdTe/CdSe/CdTe nanorods studied here, the phosphonic acid ligands adsorb more strongly to the non-polar side facets than the polar surfaces at the ends of the nanorods, [125,126] which may further stabilize the rod shape by lowering the surface tension on specific crystal facets. More accurate, predictive models of chemical and physical transformations in nanocrystals, such as the coalescence and atomic interdiffusion studied

here, are needed; however, it appears that relatively simple continuum models can nevertheless provide some rough guidelines for how fast these processes occur.

7.2.2 Photovoltaic nanocrystal synthesis

An eventual goal for I-III-VI$_2$ nanocrystals is to establish low-cost photovoltaic devices. Our group has been exploring this area, and had a reasonable efficiency with CuInS$_2$, CuInSe$_2$, and Cu(In$_x$Ga$_{1-x}$)Se$_2$ (CIGS) nanocrystal inks for printable photovoltaics as shown in Figures 7.1 and 7.2.[51]
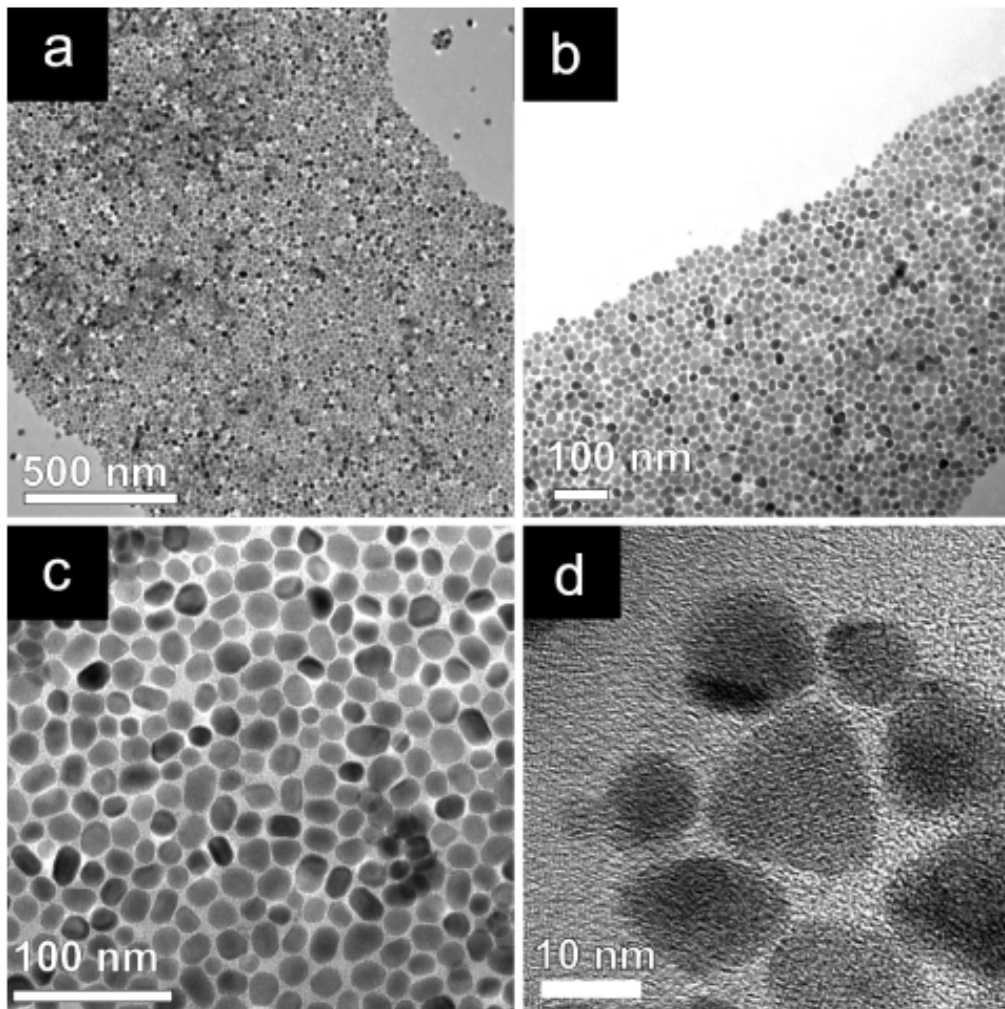
Figure 7.1. TEM image of CuInSe$_2$ nanocrystals. Courtesy of M. G. Panthani *et al.*, *Journal of the American Chemical Society*, 130, 16770, 2008.
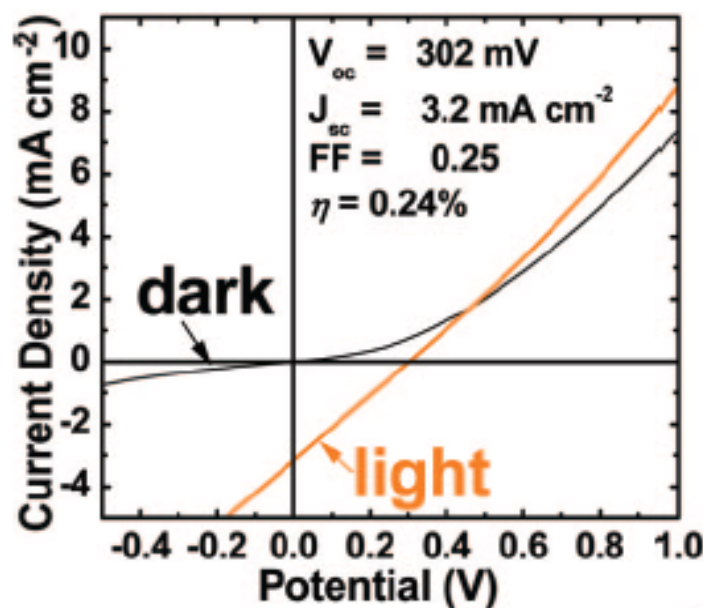
Figure 7.2. Current-voltage characteristics of a CuInSe$_2$ nanocrystal PV device. Courtesy of M. G. Panthani *et al.*, *Journal of the American Chemical Society*, 130, 16770, 2008.

In addition to make Cu(In,Ga)Se$_2$ (CIGS) nanocrystals, it will be also interesting to determine if more complicated chemistry is possible using synthetic approaches similar to those reported here; for example, as in the synthesis of CZTS materials, like Cu$_2$ZnSnSe$_4$, which are also potential candidates for photovoltaic devices. In fact, our group also has succeeded in synthesizing Cu$_2$ZnSnSe$_4$ nanocrystals and applying those nanocrystals to photovoltaic devices, as shown in Figures 7.3 and 7.4.[127]
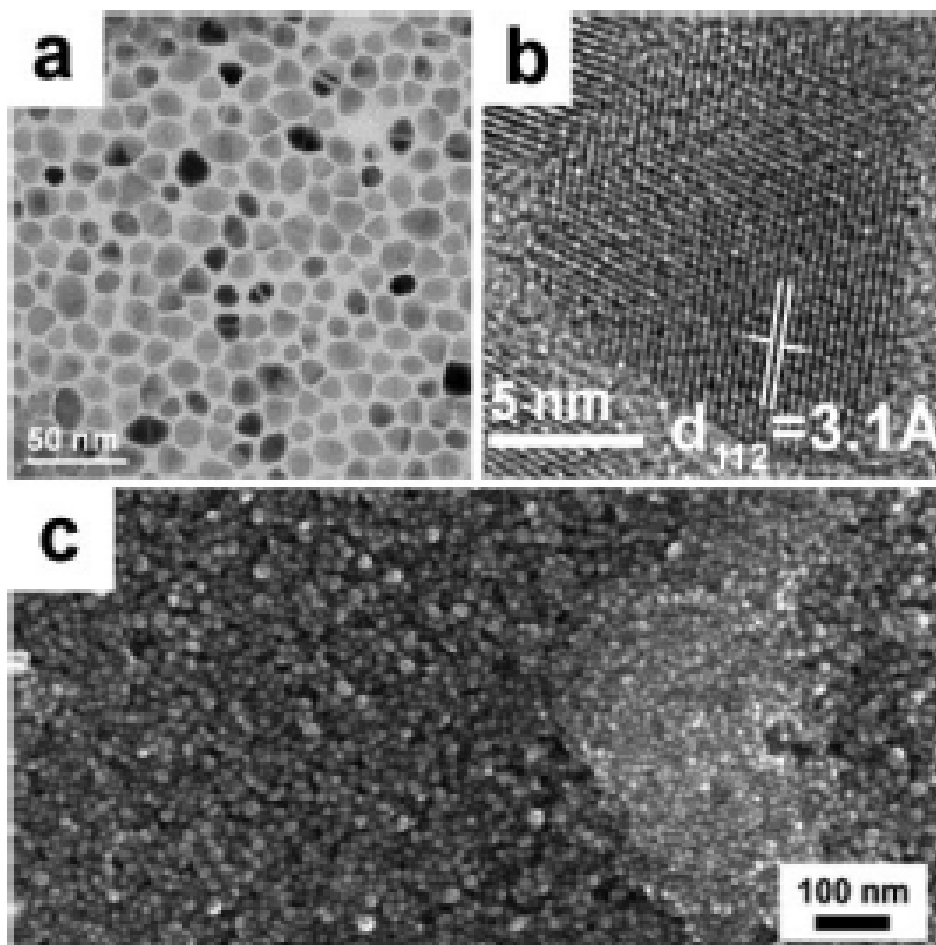
Figure 7.3. TEM image of Cu₂ZnSnSe₄ nanocrystals. Courtesy of C. Steinhagen *et al.*, *Journal of the American Chemical Society*, 131, 12554, 2009.
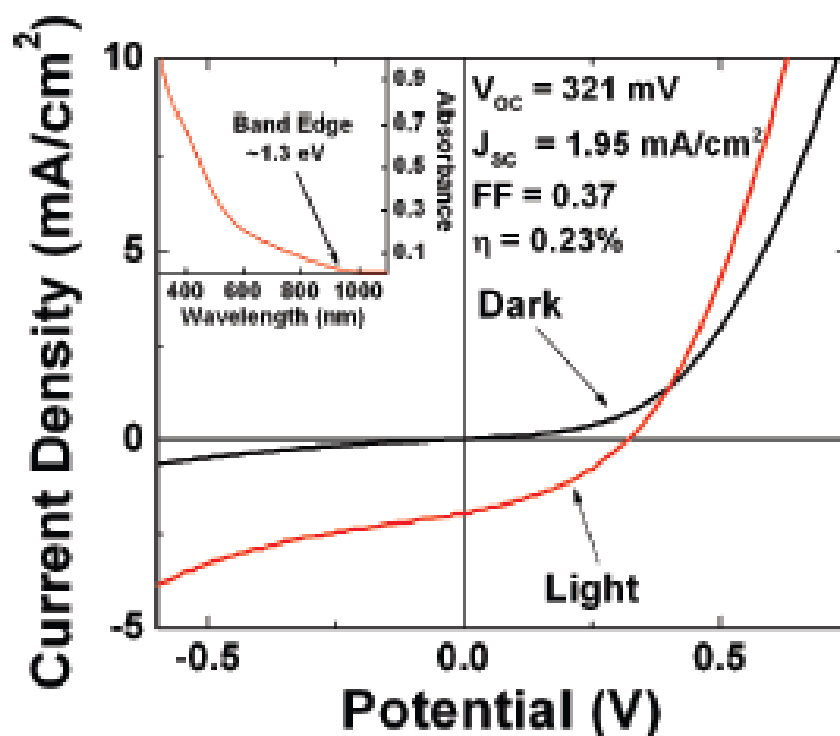
Figure 7.4.   Current-voltage characteristics of a CZTS nanocrystal PV device. Inset: room-temperature UV-vis-NIR absorbance spectrum of CZTS nanocrystals dispersed in toluene.   Courtesy of C. Steinhagen *et al.*, *Journal of the American Chemical Society*, 131, 12554, 2009.

7.2.3 Mechanism study for monodisperse nanocrystals

In the Chapter 4, I discussed the effect of excess CuCl precursor on the monodispersity of trigonal pyramidal $CuInSe_2$ nanocrystals.   However, it is known that diverse variables such as reaction condition (temperature, time, and sequence), kind of precursor and capping ligand, precursor and monomer concentration, and reactivity among the reactants can affect a nucleation-growth process for colloidal nanocrystal formation.   Moveover, it was, very recently, also shown that other factors such as sensitivity of selenourea could hinder the formation of monodisperse $CuInSe_2$

nanocrystals. Further study on these is needed for a clear understanding of variables to affect the monodispersity.

7.2.4 Phase behavior and crystals structure of nanocrystals

The phase behavior and crystal structure of nanocrystalline materials are known to differ in some cases from bulk materials, as in the case of Co nanocrystals with an unusual ε-phase,[22,128,129] $AgInSe_2$ nanorods with a new orthorhombic phase,[130] and $CuInS_2$ with an unexpected wurtzite phase.[66] The wurtzite-chalcopyrite polytypism observed here for $CuInS_2$ and $CuInSe_2$ nanodisks provides another example of unexpected phase behavior. Another important feature of nanocrystals is their ability to accommodate significant amounts of lattice strain at interfaces, which leads to different defect formation mechanisms than in bulk materials,[2,16,17,122] and may provide another reason why these nanodisks exhibit wurtzite-chalcopyrite polytypism that is uncommon in bulk or thin film materials.

7.3 REFERENCES

(1)   Leff, D. V.; Ohara, P. C.; Heath, J. R.; Gelbart, W. M. *Journal of Physical Chemistry* **1995**, *99*, 7036-7041.

(2)   Tang, Z. Y.; Kotov, N. A.; Giersig, M. *Science* **2002**, *297*, 237-240.

(3)   Cho, K. S.; Talapin, D. V.; Gaschler, W.; Murray, C. B. *Journal of the American Chemical Society* **2005**, *127*, 7140-7147.

(4)   Nair, P. S.; Fritz, K. P.; Scholes, G. D. *Small* **2007**, *3*, 481-487.

(5)   Puzder, A.; Williamson, A. J.; Zaitseva, N.; Galli, G.; Manna, L.; Alivisatos, A. P. *Nano Letters* **2004**, *4*, 2361-2365.

(6)   Panthani, M. G.; Akhavan, V.; Goodfellow, B.; Schmidtke, J. P.; Dunn, L.; Dodabalapur, A.; Barbara, P. F.; Korgel, B. A. *J Am Chem Soc* **2008**, *130*, 16770-16777.

(7)   Steinhagen, C.; Panthani, M. G.; Akhavan, V.; Goodfellow, B.; Koo, B.; Korgel, B. A. *Journal of the American Chemical Society* **2009**, *131*, 12554.

(8)   Sun, S. H.; Murray, C. B. *Journal of Applied Physics* **1999**, *85*, 4325-4330.

(9)   Dinega, D. P.; Bawendi, M. G. *Angewandte Chemie-International Edition* **1999**, *38*, 1788-1791.

(10)   Puntes, V. F.; Krishnan, K. M.; Alivisatos, A. P. *Science* **2001**, *291*, 2115-2117.

(11)   Ng, M. T.; Boothroyd, C. B.; Vittal, J. J. *Journal of the American Chemical Society* **2006**, *128*, 7118-7119.

(12)   Pan, D. C.; An, L. J.; Sun, Z. M.; Hou, W.; Yang, Y.; Yang, Z. Z.; Lu, Y. F. *Journal of the American Chemical Society* **2008**, *130*, 5620.

(13)   Kamalov, V. F.; Little, R.; Logunov, S. L.; ElSayed, M. A. *Journal of Physical Chemistry* **1996**, *100*, 6381-6384.

(14)   Chen, X. B.; Lou, Y. B.; Samia, A. C.; Burda, C. *Nano Letters* **2003**, *3*, 799-803.

(15)   Shenoy, V. B. *Physical Review B* **2005**, *71*.

(16)   Koo, B.; Korgel, B. A. *Nano Letters* **2008**, *8*, 2490-2496.

Bibliography

Ahn, S.; Kim, K.; Yoon, K., "Cu(In,Ga)Se$_2$ thin film solar cells from nanoparticle precursors," *Current Applied Physics* (2008), 8(6), 766-769.

Allen, P. M.; Bawendi, M. G., "Ternary I-III-VI quantum dots luminescent in the red to near-infrared," *Journal of the American Chemical Society* (2008), 130(29), 9240.

Asokan, S.; Krueger, K. M.; Colvin, V. L.; Wong, M. S., "Shape-controlled synthesis of CdSe tetrapods using cationic surfactant ligands," *Small* (2007), 3(7), 1164-1169.

Balasubramanian, R.; Wilcox, W. R., "Surface-Tension and Contact Angles of Molten Cadmium Telluride," *International Journal of Thermophysics* (1990), 11(1), 25-35.

Barnard, A. S.; Xu, H. F., "First principles and thermodynamic modeling of CdS surfaces and nanorods," *Journal of Physical Chemistry C* (2007), 111(49), 18112-18117.

Batabyal, S. K.; Tian, L.; Venkatram, N.; Ji, W.; Vittal, J. J., "Phase-Selective Synthesis of CuInS$_2$ Nanocrystals," *Journal of Physical Chemistry C* (2009), 113(33), 15037-15042.

Binsma, J. J. M.; Giling, L. J.; Bloem, J., "Phase-Relations in the System Cu$_2$S-In$_2$S$_3$," *Journal of Crystal Growth* (1980), 50(2), 429-436.

Cahen, D.; Dagan, G.; Mirovsky, Y.; Hodes, G.; Giriat, W.; Lubke, M., "Ternary Chalcogenide-Based Photoelectrochemical Cells .4. Further Characterization of the Normal-CuInS$_2$ and Normal-CuInSe$_2$ Aqueous Polysulfide Systems," *Journal of the Electrochemical Society* (1985), 132(5), 1062-1070.

Castro, S. L.; Bailey, S. G.; Raffaelle, R. P.; Banger, K. K.; Hepp, A. F., "Nanocrystalline chalcopyrite materials (CuInS$_2$ and CuInSe$_2$) via low-temperature pyrolysis of molecular single-source precursors," *Chemistry of Materials* (2003), 15(16), 3142-3147.

Casula, M. F.; Jun, Y. W.; Zaziski, D. J.; Chan, E. M.; Corrias, A.; Alivisatos, A. P., "The concept of delayed nucleation in nanocrystal growth demonstrated for the case of iron oxide nanodisks," *Journal of the American Chemical Society* (2006), 128(5), 1675-1682.

Chen, X. B.; Lou, Y. B.; Samia, A. C.; Burda, C., "Coherency strain effects on the optical response of core/shell heteronanostructures," *Nano Letters* (2003), 3(6), 799-803.

Cho, K. S.; Talapin, D. V.; Gaschler, W.; Murray, C. B., "Designing PbSe nanowires and nanorings through oriented attachment of nanoparticles," *Journal of the American Chemical Society* (2005), 127(19), 7140-7147.

Coe, S.; Woo, W. K.; Bawendi, M.; Bulovic, V., "Electroluminescence from single monolayers of nanocrystals in molecular organic devices," *Nature* (2002), 420(6917), 800-803.

Connor, S. T.; Hsu, C. M.; Weil, B. D.; Aloni, S.; Cui, Y., "Phase Transformation of Biphasic Cu_2S-$CuInS_2$ to Monophasic $CuInS_2$ Nanorods," *Journal of the American Chemical Society* (2009), 131(13), 4962-4966.

Dinega, D. P.; Bawendi, M. G., "A solution-phase chemical approach to a new crystal structure of cobalt," *Angewandte Chemie-International Edition* (1999), 38(12), 1788-1791.

Dingreville, R.; Qu, J. M.; Cherkaoui, M., "Surface free energy and its effect on the elastic behavior of nano-sized particles, wires and films," *Journal of the Mechanics and Physics of Solids* (2005), 53(8), 1827-1854.

Dorfs, D.; Eychmuller, A., "Multishell semiconductor nanocrystals," *Zeitschrift Fur Physikalische Chemie-International Journal of Research in Physical Chemistry & Chemical Physics* (2006), 220(12), 1539-1552.

Du, W. M.; Qian, X. F.; Yin, J.; Gong, Q., "Shape- and phase-controlled synthesis of monodisperse, single-crystalline ternary chalcogenide colloids through a convenient solution synthesis strategy," *Chemistry-a European Journal* (2007), 13(31), 8840-8846.

Dutta, D. P.; Sharma, G., "A facile route to the synthesis of $CuInS_2$ nanoparticles," *Materials Letters* (2006), 60(19), 2395-2398.

El-Sayed, M. A., "Small is different: Shape-, size-, and composition-dependent properties of some colloidal semiconductor nanocrystals," *Accounts of Chemical Research* (2004), 37(5), 326-333.

Friedlander, S. K.; Wu, M. K., "Linear Rate Law for the Decay of the Excess Surface-Area of a Coalescing Solid Particle," *Physical Review B* (1994), 49(5), 3622-3624.

Gerion, D.; Zaitseva, N.; Saw, C.; Casula, M. F.; Fakra, S.; Van Buuren, T.; Galli, G., "Solution synthesis of germanium nanocrystals: Success and open challenges," *Nano Letters* (2004), 4(4), 597-602.

Ghezelbash, A.; Korgel, B. A., "Nickel sulfide and copper sulfide nanocrystal synthesis and polymorphism," *Langmuir* (2005), 21(21), 9451-9456.

Gillin, W. P.; Dunstan, D. J., "Strain and Interdiffusion in Semiconductor Heterostructures," *Physical Review B* (1994), 50(11), 7495-7498.

Gottschalk, H.; Patzer, G.; Alexander, H., "Stacking-Fault Energy and Ionicity of Cubic-III-V Compounds," *Physica Status Solidi a-Applied Research* (1978), 45(1), 207-217.

Gou, X. L.; Cheng, F. Y.; Shi, Y. H.; Zhang, L.; Peng, S. J.; Chen, J.; Shen, P. W., "Shape-controlled synthesis of ternary chalcogenide $ZnIn_2S_4$ and $CuIn(S,Se)_2$ nano-/microstructures via facile solution route," *Journal of the American Chemical Society* (2006), 128(22), 7222-7229.

Gunes, S.; Neugebauer, H.; Sariciftci, N. S.; Roither, H.; Kovalenko, M.; Pillwein, G.; Heiss, W., "Hybrid solar cells using HgTe nanocrystals and nanoporous TiO_2 electrodes," *Advanced Functional Materials* (2006), 16(8), 1095-1099.

Guo, Q.; Ford, G. M.; Hillhouse, H. W.; Agrawal, R., "Sulfide Nanocrystal Inks for Dense $Cu(In_{1-x}Ga_x)(S_{1-y}Se_y)_2$ Absorber Films and Their Photovoltaic Performance," *Nano Letters* (2009), 9(8), 3060-3065.

Guo, Q.; Kim, S. J.; Kar, M.; Shafarman, W. N.; Birkmire, R. W.; Stach, E. A.; Agrawal, R.; Hillhouse, H. W., "Development of $CuInSe_2$ nanocrystal and nanoring inks for low-cost solar cells," *Nano Letters* (2008), 8(9), 2982-2987.

Gur, I.; Fromer, N. A.; Geier, M. L.; Alivisatos, A. P., "Air-stable all-inorganic nanocrystal solar cells processed from solution," *Science* (2005), 310(5747), 462-465.

Gurin, V. S.; Alexeenko, A. A.; Yumashev, K. V.; Prokoshin, R.; Zolotovskaya, S. A.; Zhavnerko, G. A., "Structure and optical properties of Cu_xO- and Cu_xSe-doped sol-gel silica glasses," *Materials Science & Engineering C-Biomimetic and Supramolecular Systems* (2003), 23(6-8), 1063-1067.

Halpert, J. E.; Porter, V. J.; Zimmer, J. P.; Bawendi, M. G., "Synthesis of CdSe/CdTe nanobarbells," *Journal of the American Chemical Society* (2006), 128(39), 12590-12591.

Hawa, T.; Zachariah, M. R., "Molecular dynamics simulation and continuum modeling of straight-chain aggregate sintering: Development of a phenomenological scaling law," *Physical Review B* (2007), 76(5).

Heitsch, A. T.; Fanfair, D. D.; Tuan, H. Y.; Korgel, B. A., "Solution-liquid-solid (SLS) growth of silicon nanowires," *Journal of the American Chemical Society* (2008), 130(16), 5436.

Herring, C., "Citation Classic - Diffusional Viscosity of a Polycrystalline Solid," *Current Contents/Physical Chemical & Earth Sciences* (1979), 35), P16-P16.

Hines, M. A.; Guyot-Sionnest, P., "Bright UV-blue luminescent colloidal ZnSe nanocrystals," *Journal of Physical Chemistry B* (1998), 102(19), 3655-3657.

Huynh, W. U.; Dittmer, J. J.; Alivisatos, A. P., "Hybrid nanorod-polymer solar cells," *Science* (2002), 295(5564), 2425-2427.

Jaffe, J. E.; Zunger, A., "Defect-induced nonpolar-to-polar transition at the surface of chalcopyrite semiconductors," *Physical Review B* (2001), 64(24).

Jagminas, A.; Juskenas, R.; Gailiute, I.; Statkute, G.; Tomasiunas, R., "Electrochemical synthesis and optical characterization of copper selenide nanowire arrays within the alumina pores," *Journal of Crystal Growth* (2006), 294(2), 343-348.

Jiang, Y.; Wu, Y.; Mo, X.; Yu, W. C.; Xie, Y.; Qian, Y. T., "Elemental solvothermal reaction to produce ternary semiconductor $CuInE_2$ (E = S, Se) nanorods," *Inorganic Chemistry* (2000), 39(14), 2964.

Jones, M.; Kumar, S.; Lo, S. S.; Scholes, G. D., "Exciton trapping and recombination in type II CdSe/CdTe nanorod heterostructures," *Journal of Physical Chemistry C* (2008), 112(14), 5423-5431.

Jun, Y. W.; Jung, Y. Y.; Cheon, J., "Architectural control of magnetic semiconductor nanocrystals," *Journal of the American Chemical Society* (2002), 124(4), 615-619.

Kamalov, V. F.; Little, R.; Logunov, S. L.; ElSayed, M. A., "Picosecond electronic relaxation in CdS/HgS/CdS quantum dot quantum well semiconductor nanoparticles," *Journal of Physical Chemistry* (1996), 100(16), 6381-6384.

Khreis, O. M., "Interdiffusion and the strain effect in pseudomorphic quantum well heterostructures," *Solid State Communications* (2004), 132(11), 767-771.

Kino, T.; Kuzuya, T.; Itoh, K.; Sumiyama, K.; Wakamatsu, T.; Ichidate, M., "Synthesis of chalcopyrite nanoparticles via thermal decomposition of metal-thiolate," *Materials Transactions* (2008), 49(3), 435-438.

Kokkonis, P.; Leute, V., "Simulation of interdiffusion processes in quasiternary systems of type MX/NX/NY/MY (alpha-class)," *Solid State Ionics* (2005), 176(37-38), 2681-2688.

Koleilat, G. I.; Levina, L.; Shukla, H.; Myrskog, S. H.; Hinds, S.; Pattantyus-Abraham, A. G.; Sargent, E. H., "Efficient, stable infrared photovoltaics based on solution-cast colloidal quantum dots," *Acs Nano* (2008), 2(5), 833-840.

Konstantatos, G.; Howard, I.; Fischer, A.; Hoogland, S.; Clifford, J.; Klem, E.; Levina, L.; Sargent, E. H., "Ultrasensitive solution-cast quantum dot photodetectors," *Nature* (2006), 442(7099), 180-183.

Koo, B.; Korgel, B. A., "Coalescence and interface diffusion in linear CdTe/CdSe/CdTe heterojunction nanorods," *Nano Letters* (2008), 8(8), 2490-2496.

Koo, B.; Patel, R. N.; Korgel, B. A., "Synthesis of CuInSe$_2$ Nanocrystals with Trigonal Pyramidal Shape," *Journal of the American Chemical Society* (2009), 131(9), 3134.

Koo, B.; Patel, R. N.; Korgel, B. A., "Wurtzite-Chalcopyrite Polytypism in CuInS$_2$ Nanodisks," *Chemistry of Materials* (2009), 21(9), 1962-1966.

Kumar, S.; Jones, M.; Lo, S. S.; Scholes, G. D., "Nanorod heterostructures showing photoinduced charge separation," *Small* (2007), 3(9), 1633-1639.

Kumar, S.; Scholes, G. D., "Colloidal nanocrystal solar cells," *Microchimica Acta* (2008), 160(3), 315-325.

Kumikov, V. K.; Khokonov, K. B., "On the Measurement of Surface Free-Energy and Surface-Tension of Solid Metals," *Journal of Applied Physics* (1983), 54(3), 1346-1350.

Kuo, K. T.; Chen, S. Y.; Cheng, B. M.; Lin, C. C., "Synthesis and characterization of highly luminescent CuInS$_2$ and CuInS$_2$/ZnS (core/shell) nanocrystals," *Thin Solid Films* (2008), 517(3), 1257-1261.

Kwon, S. G.; Hyeon, T., "Colloidal Chemical Synthesis and Formation Kinetics of Uniformly Sized Nanocrystals of Metals, Oxides, and Chalcogenides," *Accounts of Chemical Research* (2008), 41(12), 1696-1709.

Kwon, S. G.; Piao, Y.; Park, J.; Angappane, S.; Jo, Y.; Hwang, N. M.; Park, J. G.; Hyeon, T., "Kinetics of monodisperse iron oxide nanocrystal formation by "heating-up" process," *Journal of the American Chemical Society* (2007), 129(41), 12571-12584.

Law, M.; Luther, J. M.; Song, O.; Hughes, B. K.; Perkins, C. L.; Nozik, A. J., "Structural, optical, and electrical properties of PbSe nanocrystal solids treated thermally or with simple amines," *Journal of the American Chemical Society* (2008), 130(18), 5974-5985.

Leff, D. V.; Ohara, P. C.; Heath, J. R.; Gelbart, W. M., "Thermodynamic Control of Gold Nanocrystal Size - Experiment and Theory," *Journal of Physical Chemistry* (1995), 99(18), 7036-7041.

Leschkies, K. S.; Divakar, R.; Basu, J.; Enache-Pommer, E.; Boercker, J. E.; Carter, C. B.; Kortshagen, U. R.; Norris, D. J.; Aydil, E. S., "Photosensitization of ZnO nanowires with CdSe quantum dots for photovoltaic devices," *Nano Letters* (2007), 7(6), 1793-1798.

Li, B.; Xie, Y.; Huang, J. X.; Qian, Y. T., "Synthesis by a solvothermal route and characterization of $CuInSe_2$ nanowhiskers and nanoparticles," *Advanced Materials* (1999), 11(17), 1456-1459.

Lou, W. J.; Chen, M.; Wang, X. B.; Liu, W. M., "Size control of monodisperse copper sulfide faceted nanocrystals and triangular nanoplates," *Journal of Physical Chemistry C* (2007), 111(27), 9658-9663.

Lu, X. M.; Ziegler, K. J.; Ghezelbash, A.; Johnston, K. P.; Korgel, B. A., "Synthesis of germanium nanocrystals in high temperature supercritical fluid solvents," *Nano Letters* (2004), 4(5), 969-974.

Malik, M. A.; O'Brien, P.; Revaprasadu, N., "A novel route for the preparation of CuSe and $CuInSe_2$ nanoparticles," *Advanced Materials* (1999), 11(17), 1441-1444.

Manna, L.; Milliron, D. J.; Meisel, A.; Scher, E. C.; Alivisatos, A. P., "Controlled growth of tetrapod-branched inorganic nanocrystals," *Nature Materials* (2003), 2(6), 382-385.

Manna, L.; Scher, E. C.; Alivisatos, A. P., "Synthesis of soluble and processable rod-, arrow-, teardrop-, and tetrapod-shaped CdSe nanocrystals," *Journal of the American Chemical Society* (2000), 122(51), 12700-12706.

Manna, L.; Scher, E. C.; Li, L. S.; Alivisatos, A. P., "Epitaxial growth and photochemical annealing of graded CdS/ZnS shells on colloidal CdSe nanorods," *Journal of the American Chemical Society* (2002), 124(24), 7136-7145.

Manna, L.; Wang, L. W.; Cingolani, R.; Alivisatos, A. P., "First-principles modeling of unpassivated and surfactant-passivated bulk facets of wurtzite CdSe: A model system for studying the anisotropic growth of CdSe nanocrystals," *Journal of Physical Chemistry B* (2005), 109(13), 6183-6192.

Medvedeva, N. I.; Shalaeva, E. V.; Kuznetsov, M. V.; Yakushev, M. V., "First-principles study of deformation behavior and structural defects in $CuInSe_2$ and $Cu(In,Ga)Se_2$," *Physical Review B* (2006), 73(3).

Metraux, G. S.; Cao, Y. C.; Jin, R. C.; Mirkin, C. A., "Triangular nanofrarnes made of gold and silver," *Nano Letters* (2003), 3(4), 519-522.

Mews, A.; Eychmuller, A.; Giersig, M.; Schooss, D.; Weller, H., "Preparation, Characterization, and Photophysics of the Quantum-Dot Quantum-Well System Cds/Hgs/Cds," *Journal of Physical Chemistry* (1994), 98(3), 934-941.

Milliron, D. J.; Hughes, S. M.; Cui, Y.; Manna, L.; Li, J. B.; Wang, L. W.; Alivisatos, A. P., "Colloidal nanocrystal heterostructures with linear and branched topology," *Nature* (2004), 430(6996), 190-195.

Mokari, T.; Rothenberg, E.; Popov, I.; Costi, R.; Banin, U., "Selective growth of metal tips onto semiconductor quantum rods and tetrapods," *Science* (2004), 304(5678), 1787-1790.

Murray, C. B.; Norris, D. J.; Bawendi, M. G., "Synthesis and Characterization of Nearly Monodisperse Cde (E = S, Se, Te) Semiconductor Nanocrystallites," *Journal of the American Chemical Society* (1993), 115(19), 8706-8715.

Nair, P. S.; Fritz, K. P.; Scholes, G. D., "Evolutionary shape control during colloidal quantum-dot growth," *Small* (2007), 3(3), 481-487.

Nairn, J. J.; Shapiro, P. J.; Twamley, B.; Pounds, T.; von Wandruszka, R.; Fletcher, T. R.; Williams, M.; Wang, C. M.; Norton, M. G., "Preparation of ultrafine chalcopyrite nanoparticles via the photochemical decomposition of molecular single-source precursors," *Nano Letters* (2006), 6(6), 1218-1223.

Nakamura, H.; Kato, W.; Uehara, M.; Nose, K.; Omata, T.; Otsuka-Yao-Matsuo, S.; Miyazaki, M.; Maeda, H., "Tunable photoluminescence wavelength of chalcopyrite $CuInS_2$-based semiconductor nanocrystals synthesized in a colloidal system," *Chemistry of Materials* (2006), 18(14), 3330-3335.

Ng, M. T.; Boothroyd, C. B.; Vittal, J. J., "One-pot synthesis of new-phase $AgInSe_2$ nanorods," *Journal of the American Chemical Society* (2006), 128(22), 7118-7119.

Nose, K.; Omata, T.; Otsuka-Yao-Matsuo, S., "Colloidal Synthesis of Ternary Copper Indium Diselenide Quantum Dots and Their Optical Properties," *Journal of Physical Chemistry C* (2009), 113(9), 3455-3460.

Nose, K.; Soma, Y.; Omata, T.; Otsuka-Yao-Matsuo, S., "Synthesis of Ternary $CuInS_2$ Nanocrystals; Phase Determination by Complex Ligand Species," *Chemistry of Materials* (2009), 21(13), 2607-2613.

Nozik, A. J., "Multiple exciton generation in semiconductor quantum dots," *Chemical Physics Letters* (2008), 457(1-3), 3-11.

Pan, D. C.; An, L. J.; Sun, Z. M.; Hou, W.; Yang, Y.; Yang, Z. Z.; Lu, Y. F., "Synthesis of Cu-In-S ternary nanocrystals with tunable structure and composition," *Journal of the American Chemical Society* (2008), 130(17), 5620.

Panthani, M. G.; Akhavan, V.; Goodfellow, B.; Schmidtke, J. P.; Dunn, L.; Dodabalapur, A.; Barbara, P. F.; Korgel, B. A., "Synthesis of $CuInS_2$, $CuInSe_2$, and $Cu(In_xGa_{1-x})Se_2$ (CIGS) Nanocrystal "Inks" for Printable Photovoltaics," *Journal of the American Chemical Society* (2008), 130(49), 16770-16777.

Park, J.; An, K. J.; Hwang, Y. S.; Park, J. G.; Noh, H. J.; Kim, J. Y.; Park, J. H.; Hwang, N. M.; Hyeon, T., "Ultra-large-scale syntheses of monodisperse nanocrystals," *Nature Materials* (2004), 3(12), 891-895.

Park, J. S.; Dong, Z.; Kim, S.; Perepezko, J. H., "CuInSe$_2$ phase formation during Cu2Se/In2Se3 interdiffusion reaction," *Journal of Applied Physics* (2000), 87(8), 3683-3690.

Peng, H. L.; Schoen, D. T.; Meister, S.; Zhang, X. F.; Cui, Y., "Synthesis and phase transformation of In$_2$Se$_3$ and CuInSe$_2$ nanowires," *Journal of the American Chemical Society* (2007), 129(1), 34-35.

Peng, S.; Sun, S. H., "Synthesis and characterization of monodisperse hollow Fe$_3$O$_4$ nanoparticles," *Angewandte Chemie-International Edition* (2007), 46(22), 4155-4158.

Peng, X. G.; Wickham, J.; Alivisatos, A. P., "Kinetics of II-VI and III-V colloidal semiconductor nanocrystal growth: "Focusing" of size distributions," *Journal of the American Chemical Society* (1998), 120(21), 5343-5344.

Peng, Z. A.; Peng, X. G., "Nearly monodisperse and shape-controlled CdSe nanocrystals via alternative routes: Nucleation and growth," *Journal of the American Chemical Society* (2002), 124(13), 3343-3353.

Pinna, N.; Weiss, K.; Urban, J.; Pileni, M. P., "Triangular CdS nanocrystals: Structural and optical studies," *Advanced Materials* (2001), 13(4), 261.

Puntes, V. F.; Krishnan, K. M.; Alivisatos, A. P., "Colloidal nanocrystal shape and size control: The case of cobalt," *Science* (2001), 291(5511), 2115-2117.

Puntes, V. F.; Zanchet, D.; Erdonmez, C. K.; Alivisatos, A. P., "Synthesis of hcp-Co nanodisks," *Journal of the American Chemical Society* (2002), 124(43), 12874-12880.

Puzder, A.; Williamson, A. J.; Zaitseva, N.; Galli, G.; Manna, L.; Alivisatos, A. P., "The effect of organic ligand binding on the growth of CdSe nanoparticles probed by Ab initio calculations," *Nano Letters* (2004), 4(12), 2361-2365.

Qi, Y. X.; Liu, Q. C.; Tang, K. B.; Liang, Z. H.; Ren, Z. B.; Liu, X. M., "Synthesis and Characterization of Nanostructured Wurtzite CuInS$_2$: A New Cation Disordered Polymorph of CuInS$_2$," *Journal of Physical Chemistry C* (2009), 113(10), 3939-3944.

Rempel, J. Y.; Trout, B. L.; Bawendi, M. G.; Jensen, K. F., "Density functional theory study of ligand binding on CdSe (0001), (000-1), and (11-20) single crystal relaxed and reconstructed surfaces: Implications for nanocrystalline growth," *Journal of Physical Chemistry B* (2006), 110(36), 18007-18016.

Repins, I.; Contreras, M. A.; Egaas, B.; DeHart, C.; Scharf, J.; Perkins, C. L.; To, B.; Noufi, R., "19.9%-efficient ZnO/CdS/CuInGaSe$_2$ solar cell with 81.2% fill factor," *Progress in Photovoltaics* (2008), 16(3), 235-239.

Robinson, R. D.; Sadtler, B.; Demchenko, D. O.; Erdonmez, C. K.; Wang, L. W.; Alivisatos, A. P., "Spontaneous superlattice formation in nanorods through partial cation exchange," *Science* (2007), 317(5836), 355-358.

Sadowski, T.; Ramprasad, R., "Stability and electronic structure of CdSe nanorods from first principles," *Physical Review B* (2007), 76(23).

Sapra, S.; Poppe, J.; Eychmuller, A., "CdSe nanorod synthesis: A new approach," *Small* (2007), 3(11), 1886-1888.

Saunders, A. E.; Koo, B.; Wang, X. Y.; Shih, C. K.; Korgel, B. A., "Structural characterization and temperature-dependent photoluminescence of linear CdTe/CdSe/CdTe heterostructure nanorods," *Chemphyschem* (2008), 9(8), 1158-1163.

Schaller, R. D.; Klimov, V. I., "High efficiency carrier multiplication in PbSe nanocrystals: Implications for solar energy conversion," *Physical Review Letters* (2004), 92(18).

Schimmel, M. I.; de Tacconi, N. R.; Rajeshwar, K., "Anodic electrosynthesis of Cu$_2$S and CuInS$_2$ films," *Journal of Electroanalytical Chemistry* (1998), 453(1-2), 187-195.

Shenoy, V. B., "Atomistic calculations of elastic properties of metallic fcc crystal surfaces," *Physical Review B* (2005), 71(9).

Shevchenko, E. V.; Talapin, D. V.; Kotov, N. A.; O'Brien, S.; Murray, C. B., "Structural diversity in binary nanoparticle superlattices," *Nature* (2006), 439(7072), 55-59.

Shieh, F.; Saunders, A. E.; Korgel, B. A., "General shape control of colloidal CdS, CdSe, CdTe quantum rods and quantum rod heterostructures," *Journal of Physical Chemistry B* (2005), 109(18), 8538-8542.

Sigman, M. B.; Ghezelbash, A.; Hanrath, T.; Saunders, A. E.; Lee, F.; Korgel, B. A., "Solventless synthesis of monodisperse Cu$_2$S nanorods, nanodisks, and nanoplatelets," *Journal of the American Chemical Society* (2003), 125(51), 16050-16057.

Steinhagen, C.; Panthani, M. G.; Akhavan, V.; Goodfellow, B.; Koo, B.; Korgel, B. A., "Synthesis of Cu$_2$ZnSnS$_4$ Nanocrystals for Use in Low-Cost Photovoltaics," *Journal of the American Chemical Society* (2009), 131(35), 12554.

Sun, S. H.; Murray, C. B., "Synthesis of monodisperse cobalt nanocrystals and their assembly into magnetic superlattices (invited)," *Journal of Applied Physics* (1999), 85(8), 4325-4330.

Sun, S. H.; Murray, C. B.; Weller, D.; Folks, L.; Moser, A., "Monodisperse FePt nanoparticles and ferromagnetic FePt nanocrystal superlattices," *Science* (2000), 287(5460), 1989-1992.

Talapin, D. V.; Rogach, A. L.; Haase, M.; Weller, H., "Evolution of an ensemble of nanoparticles in a colloidal solution: Theoretical study," *Journal of Physical Chemistry B* (2001), 105(49), 12278-12285.

Tang, J.; Hinds, S.; Kelley, S. O.; Sargent, E. H., "Synthesis of Colloidal $CuGaSe_2$, $CuInSe_2$, and $Cu(InGa)Se_2$ Nanoparticles," *Chemistry of Materials* (2008), 20(22), 6906-6910.

Tang, Z. Y.; Kotov, N. A.; Giersig, M., "Spontaneous organization of single CdTe nanoparticles into luminescent nanowires," *Science* (2002), 297(5579), 237-240.

Todorov, T.; Cordoncillo, E.; Sanchez-Royo, J. F.; Carda, J.; Escribano, P., "$CuInS_2$ films for photovoltaic applications deposited by a low-cost method," *Chemistry of Materials* (2006), 18(13), 3145-3150.

Trinh, M. T.; Houtepen, A. J.; Schins, J. M.; Hanrath, T.; Piris, J.; Knulst, W.; Goossens, A. P. L. M.; Siebbeles, L. D. A., "In spite of recent doubts carrier multiplication does occur in PbSe nanocrystals," *Nano Letters* (2008), 8(6), 1713-1718.

Uehara, M.; Watanabe, K.; Tajiri, Y.; Nakamura, H.; Maeda, H., "Synthesis of $CuInS_2$ fluorescent nanocrystals and enhancement of fluorescence by controlling crystal defect," *Journal of Chemical Physics* (2008), 129(13).

Wang, D. S.; Zheng, W.; Hao, C. H.; Peng, Q.; Li, Y. D., "General synthesis of I-III-VI$_2$ ternary semiconductor nanocrystals," *Chemical Communications* (2008), 22), 2556-2558.

Wang, W.; Banerjee, S.; Jia, S. G.; Steigerwald, M. L.; Herman, I. P., "Ligand control of growth, morphology, and capping structure of colloidal CdSe nanorods," *Chemistry of Materials* (2007), 19(10), 2573-2580.

Wang, Y. L.; Cai, L.; Xia, Y. N., "Monodisperse spherical colloids of Pb and their use as chemical templates to produce hollow particles," *Advanced Materials* (2005), 17(4), 473.

Wei, S. H.; Zhang, S. B.; Zunger, A., "Effects of Ga addition to $CuInSe_2$ on its electronic, structural, and defect properties," *Applied Physics Letters* (1998), 72(24), 3199-3201.

Wu, Y.; Wadia, C.; Ma, W. L.; Sadtler, B.; Alivisatos, A. P., "Synthesis and photovoltaic application of copper(I) sulfide nanocrystals," *Nano Letters* (2008), 8(8), 2551-2555.

Xu, X. X.; Liu, F.; Yu, K. H.; Huang, W.; Peng, B.; Wei, W., "A kinetic model for nanocrystal morphology evolution," *Chemphyschem* (2007), 8(5), 703-711.

Yang, Y. H.; Chen, Y. T., "Solvothermal preparation and spectroscopic characterization of copper indium diselenide nanorods," *Journal of Physical Chemistry B* (2006), 110(35), 17370-17374.

Yin, Y. D.; Erdonmez, C. K.; Cabot, A.; Hughes, S.; Alivisatos, A. P., "Colloidal synthesis of hollow cobalt sulfide nanocrystals," *Advanced Functional Materials* (2006), 16(11), 1389-1399.

Yong, K. T.; Sahoo, Y.; Swihart, M. T.; Prasad, P. N., "Growth of CdSe quantum rods and multipods seeded by noble-metal nanoparticles," *Advanced Materials* (2006), 18(15), 1978.

Zhang, S. B.; Wei, S. H., "Reconstruction and energetics of the polar (112) and (11-2) versus the nonpolar (220) surfaces of $CuInSe_2$," *Physical Review B* (2002), 65(8).

Zhang, X.; Brynda, M.; Britt, R. D.; Carroll, E. C.; Larsen, D. S.; Louie, A. Y.; Kauzlarich, S. M., "Synthesis and characterization of manganese-doped silicon nanoparticles: Bifunctional paramagnetic-optical nanomaterial," *Journal of the American Chemical Society* (2007), 129(35), 10668.

Zhang, Y. W.; Sun, X.; Si, R.; You, L. P.; Yan, C. H., "Single-crystalline and monodisperse LaF_3 triangular nanoplates from a single-source precursor," *Journal of the American Chemical Society* (2005), 127(10), 3260-3261.

Zhong, H. Z.; Li, Y. C.; Ye, M. F.; Zhu, Z. Z.; Zhou, Y.; Yang, C. H.; Li, Y. F., "A facile route to synthesize chalcopyrite $CuInSe_2$ nanocrystals in non-coordinating solvent," *Nanotechnology* (2007), 18(2).

Zhong, H. Z.; Zhou, Y.; Yang, Y.; Yang, C. H.; Li, Y. F., "Synthesis of type II CdTe-CdSe nanocrystal heterostructured multiple-branched rods and their photovoltaic applications," *Journal of Physical Chemistry C* (2007), 111(17), 6538-6543.

Zhong, H. Z.; Zhou, Y.; Ye, M. F.; He, Y. J.; Ye, J. P.; He, C.; Yang, C. H.; Li, Y. F., "Controlled Synthesis and Optical Properties of Colloidal Ternary Chalcogenide $CuInS_2$ Nanocrystals," *Chemistry of Materials* (2008), 20(20), 6434-6443.

Vita

Bonil Koo was born in Jeonju, South Korea, on January 26, 1979, to Jawoong Koo and Dalyeon Lim. After graduating from Chonbuk Science High School in 1997, he entered the Seoul National University. He graduated with a Bachelor of Science in Chemical Engineering in February of 2003. After he fulfilled his research on colloidal nanorod synthesis in Professor Taeghwan Hyeon's research group for 2 years, he entered graduate school in August of 2005 at the University of Texas at Austin in the Department of Chemical Engineering. He obtained his Ph.D. studying CdTe/CdSe/CdTe heterostructure nanorods and I-III-VI$_2$ nanocrystals under the supervision of Professor Brian A. Korgel.

Permanent address: Joonghwasandong, Shinil Apt. 105-1001, Wansan-gu, Jeonju, South Korea

This dissertation was typed by the author.